TECHNISCHE UNIVERSITÄT MÜNCHEN
Fakultät für Maschinenwesen
Lehrstuhl für Aerodynamik und Strömungsmechanik

Numerical investigations of cavitation phenomena

Theresa Trummler

Vollständiger Abdruck der von der Fakultät für Maschinenwesen der Technischen Universität München zur Erlangung des akademischen Grades eines

Doktor-Ingenieurs

genehmigten Dissertation.

Vorsitzender:	Prof. Dr.-Ing. Georg Wachtmeister
Prüfer der Dissertation:	1. Prof. Dr.-Ing. Nikolaus A. Adams
	2. Senior Scientist Dr. Mohamed Farhat

Die Dissertation wurde am 05.05.2020 bei der Technischen Universität München eingereicht und durch die Fakultät für Maschinenwesen am 30.11.2020 angenommen.

Theresa Trummler: *Numerical investigations of cavitation phenomena.*
Ph.D. thesis, Technical University of Munich, Germany.

Released 24.04.2020

Copyright © Theresa Trummler, April 2020

All rights reserved. No part of this publication may be reproduced, modified, re-written, or distributed in any form or by any means, without the prior written permission of the author.

Theresa Trummler, Grusonstrasse 5, 80939 München, Germany
theresa.trummler@tum.de

ABSTRACT

Cavitation plays an important role in a wide range of applications, such as fuel injection, hydrodynamic power generation, ship propellers, and biomedical applications. In this thesis, bubble collapses and cavitating nozzle flows with injection into a gaseous ambient are numerically investigated. The simulations are conducted with the fully compressible finite-volume flow solvers CATUM and ECOGEN. In CATUM, a barotropic equilibrium cavitation model embedded in a homogeneous multi-component mixture model is employed. For the numerical scheme, an upwind-biased third-order reconstruction or a central higher-order reconstruction, suitable for implicit Large-eddy simulations, are available. In ECOGEN, the two-phase flow is described using a pressure-disequilibrium model and the numerical scheme is second-order-accurate.

The first part of the thesis is dedicated to cavitation bubbles and their dynamics. The energy partitioning into rebound and shock wave energy of spherical bubble collapses is analyzed and the effect of non-condensable gas inside vapor bubbles on this partitioning is evaluated. For the simulations of vapor bubbles containing non-condensable gas, modifications of the thermodynamic multi-component model in CATUM are proposed. Then, wall-attached bubbles collapsing under atmospheric pressure are considered, enabling detailed analysis of the rebound behavior and gas influence in aspherical configurations. Further, the effect of surface geometry on the collapse behavior and erosion potential of a collapsing gas bubble is investigated. Using ECOGEN, generic configurations of bubbles collapsing close to walls with a cylindrical crevice of varying size are considered. The results show that the crevice size and the stand-off distance of the bubble have a significant influence on the collapse dynamics, the jet formation, and the subsequent wave dynamics.

In the second part of the thesis, cavitating nozzle flows with injection into gas are studied. To this end, high-resolution Large-eddy simulations of a reference experiment are performed using CATUM. Based on the results obtained, the dynamics of cloud cavitation in the nozzle are analyzed in detail, focusing on the shedding mechanisms and the formation of the re-entrant jet. The integral simulations of the nozzle flows and the subsequent injection into a gaseous ambient allow for a comprehensive analysis of the interactions. Thus, the effects of cavitation and partial gas entrainment into the nozzle on the jet break-up and mass flow can be assessed.

ZUSAMMENFASSUNG

Kavitation spielt eine wichtige Rolle in einer Vielzahl von Anwendungen, wie z. B. in der Kraftstoffeinspritzung, in der hydrodynamischen Stromerzeugung, bei Schiffspropellern und bei biomedizinischen Anwendungen. In dieser Arbeit werden Blasenkollapse und kavitierende Düsenströmungen mit Einspritzung in eine gasförmige Umgebung numerisch untersucht. Die Simulationen werden mit den kompressiblen Finite-Volumen Strömungslösern CATUM und ECOGEN durchgeführt. In CATUM wird ein barotropes Gleichgewichtskavitationsmodell, eingebettet in ein homogenes Mehrkomponenten-Mischungsmodell, verwendet. Für die numerische Flussberechnung sind eine upwind-ausgerichtete Rekonstruktion dritter Ordnung und eine zentrale Rekonstruktion höherer Ordnung, geeignet für implizite Large-eddy Simulationen, verfügbar. In ECOGEN wird die Mehrkomponenten-Strömung mit einem Druck-Ungleichgewichts-Modell beschrieben, welches Kondensation vernachlässigt. Für die numerische Berechnung wird ein Schema zweiter Ordnung verwendet.

Der erste Teil der Arbeit befasst sich mit Kavitationsblasen und ihrer Dynamik. Zuerst wird die Wirkung von nicht kondensierbarem Gas in Dampfblasen auf die Energieaufteilung in Schockwellen-Energie und Rebound-Energie bei einem sphärischen Kollaps analysiert. Für diese Simulationen wird in der Arbeit eine Erweiterung des thermodynamischen Mehrkomponenten-Modells in CATUM vorgeschlagen. Anschließend werden an der Wand anliegende Blasen, welche unter atmosphärischen Druck kollabieren, analysiert. Bei atmosphärischen Bedingungen sind detaillierte Analysen des Rebound-Verhaltens und des Gaseinflusses bei asphärischen Konfigurationen möglich. Ein weiterer untersuchter Aspekt ist der Einfluss der Oberflächengeometrie auf das Kollapsverhalten und das Erosionspotenzial einer kollabierenden Gasblase. Mit dem Strömungslöser ECOGEN werden generische Konfigurationen von anliegenden und abgelösten Blasen an einer geraden Wand mit einer zylindrischen Spalte unterschiedlicher Größe untersucht. Die Ergebnisse zeigen, dass die Spaltgröße und der Stand-Off der Blase einen signifikanten Einfluss auf die Kollaps-Dynamik, die Strahlbildung, und die nachfolgende Wellendynamik haben.

Im zweiten Teil der Arbeit werden kavitierende Düsenströmungen mit Einspritzung in Gas untersucht. Dafür werden hochaufgelöste Large-eddy Simulationen eines Referenzexperiments mit CATUM durchgeführt. Basierend auf den erhaltenen Ergebnissen wird die Dynamik der Wolkenkavitation in der Düse im Detail analysiert. Dabei ist der Schwerpunkt auf den Shedding-Mechanismen und dem auslösenden Mechanismus für die Bildung des Re-entrant Jets sowie der Geschwindigkeit von diesem. Des Weiteren ermöglichen die integralen Simulationen der Düsenströmung und der Einspritzung umfangreiche Analysen der Wechselwirkungen. Somit können die Auswirkungen von Kavitation und partieller Gaseinsaugung in die Düse auf den Strahlaufbruch und den Massenstrom untersucht werden.

DANKSAGUNG

Zuallererst möchte ich Herrn Professor Adams für die Möglichkeit der Promotion sowie die Unterstützung über all die Jahre danken. Großer Dank geht auch an den Leiter der Gasdynamik-Gruppe, Steffen Schmidt, von dessen Fachwissen auf dem Gebiet der Gasdynamik und Numerik ich sehr profitiert habe. Professor Adams und Steffen haben mir auch die Teilnahme an mehreren internationalen Konferenzen und einen mehrmonatigen Aufenthalt am Caltech ermöglicht. Vielen Dank!

Der Großteil der vorliegenden Doktorarbeit basiert auf Ergebnissen, welche mit dem institutsinternen Strömungslöser CATUM erzielt wurden. CATUM wurde von einer Vielzahl an Doktoranden über einen Zeitraum von mehr als einem Jahrzehnt konzipiert und stetig weiterentwickelt. Dabei gab es auch einige erfolgreiche Synergien mit der INCA Gruppe. An dieser Stelle möchte ich all meinen Vorgängern und Kollegen – und insbesondere Felix Braun, Christian Egerer und Michael Mihatsch – für die großartige Vorarbeit, die gute Gruppenzusammenarbeit und das Aufbauen und Weitergeben einer enormen Expertise danken. Besonderer Dank geht an Bernd Budich, der mit der von ihm geschriebenen CATUM-Multiblock-Version und dem von ihm aufgebauten CATUM-Workflow einen ganz wesentlichen Beitrag zum Gelingen dieser Arbeit geleistet hat. Darüber hinaus möchte ich Bernd auch für seine geduldige Unterstützung während meiner Anfangszeit danken, durch welche ich extrem viel bezüglich Programmieren und Code-Entwicklung gelernt habe.

Durch meine Arbeitskollegen wurde die Doktorarbeitszeit zu einer unvergesslichen, geprägt von morgendlichen Kaffee-Kochritualen, gemeinsamen Mittagessen in der Mensa und hilfreichem Austausch. Dankend erwähnen möchte ich hier besonders Alex, Thomas, Antonio und Julie. Further, I also thank my office mates at Caltech, Joaquin and Danilo, who made my stay there memorable and often cheered me up with great jokes.

Herzlicher Dank geht auch an meine lieben Eltern und meine Schwestern Maria, Ursula und Elisabeth für ihre ständige Unterstützung. Ganz besonders möchte ich Martin für seine vielseitige Unterstützung danken, welche direkt und indirekt wesentlich zum Fertigstellen dieser Doktorarbeit beigetragen hat.

PUBLICATIONS

Main parts of the thesis are based on the following publications. Text sections and figures are reproduced with the permission of the corresponding publisher.

JOURNAL PAPERS

Trummler, T., Rahn, D., Schmidt, S. J., Adams, N. A., 2018.
Large-eddy simulations of cavitating flow in a step nozzle with injection into gas.
Atomization and Sprays **28 (10)**, pp. 931–955.
https://doi.org/10.1615/AtomizSpr.2018027386

For this publication, I implemented a multi-component model for cavitating flows including an additional gas component in the in-house flow solver CATUM. I also extended the numerical framework for this purpose. For the presented Large-eddy simulations, I defined the simulation set-up and supervised the student, who performed the simulations. I designed and elaborated the paper content, conducted major parts of the post-processing and wrote the manuscript.

Trummler, T., Schmidt, S. J., Adams, N. A., 2020.
Investigation of condensation shocks and re-entrant jet dynamics in a cavitating nozzle flow by Large-eddy Simulation.
International Journal of Multiphase Flow **(125)**, 103215.
https://doi.org/10.1016/j.ijmultiphaseflow.2020.103215

This paper is based on the simulation results from the one above. I designed the paper content and elaborated it, analyzed the simulations to this regard, conducted all the post-processing, and wrote the manuscript.

Trummler, T., Bryngelson, S. H., Schmidmayer, K., Schmidt, S. J., Colonius, T., Adams, N. A., 2019.
Near-surface dynamics of a gas bubble collapsing above a crevice.
Journal of Fluid Mechanics, Volume **899**, A16
https://doi.org/10.1017/jfm.2020.432

For this paper, I designed and performed preliminary studies, designed the simulation set-up, performed all simulations, analyzed the simulation results, conducted the post-processing, conceptualized and elaborated the paper content, and wrote major parts of the manuscript.

CONFERENCE CONTRIBUTIONS

Trummler, T., Rahn, D., Schmidt, S. J., Adams, N. A., 2018.
Large-eddy simulation of cavitating nozzle flows and primary jet break-up with gas entrainment into the nozzle.
In: *Proceedings of the 10th International Symposium on Cavitation.*
ASME Press, pp. 660–664. *https://doi.org/10.1115/1.861851_ch126*.

Trummler, T., Freytag, L., Schmidt, S. J., Adams, N. A., 2018.
Large-eddy simulation of a collapsing vapor bubble containing non-condensable gas.
In: *Proceedings of the 10th International Symposium on Cavitation.*
ASME Press, pp. 656–659. *https://doi.org/10.1115/1.861851_ch125*.

Trummler, T., Schmidt, S. J., Adams, N. A., 2019.
Numerical simulation of aspherical collapses of vapor bubbles containing non-condensable gas.
10th International Conference on Multiphase Flow.

JOURNAL PAPERS AS CO–AUTHOR

Örley, F., Trummler, T., Hickel, S., Mihatsch, M. S., Schmidt, S. J., Adams, N. A., 2015.
Large-eddy simulation of cavitating nozzle flow and primary jet break-up.
Physics of Fluids **27** (**8**), 086101–28. *http://doi.org/10.1063/1.4928701*

The content of this publication is not covered in the thesis.

CONTENTS

Abstract iii

Zusammenfassung v

Publications ix

1. Introduction 1
- 1.1. Cavitation Phenomena . . . 1
  - 1.1.1. Collapse Dynamics of Cavitation Bubbles . . . 1
  - 1.1.2. Cavitating Nozzle Flows . . . 3
- 1.2. Numerical Investigations . . . 5
  - 1.2.1. Modeling of Cavitating Flows . . . 5
  - 1.2.2. Simulations of Collapsing Bubbles . . . 8
  - 1.2.3. Simulations of Cavitating Flows . . . 9
- 1.3. Scope of the Thesis . . . 10
- 1.4. Outline . . . 10

I. Physical and Numerical Model 13

2. Physical Model 15
- 2.1. Governing Equations . . . 15
- 2.2. Single-Fluid Model . . . 16
- 2.3. Equilibrium Cavitation Model for Multi-Component Flows . . . 16
  - 2.3.1. Governing Equations . . . 17
  - 2.3.2. Thermodynamic Closure Relation . . . 17
  - 2.3.3. Relation for Dynamic Viscosity . . . 19
- 2.4. Pressure-Disequilibrium Model . . . 20
  - 2.4.1. Governing Equations . . . 20
  - 2.4.2. Thermodynamic Closure Relation . . . 21
- 2.5. Summary . . . 21

3. Numerical Method 23
- 3.1. Finite Volume Method . . . 23
- 3.2. Numerical Flux Function . . . 23
  - 3.2.1. Upwind-biased Scheme . . . 24
  - 3.2.2. Higher-order Central Reconstruction . . . 25
  - 3.2.3. Sensor Functional . . . 26

3.2.4. Extension for Gas Modeling . . . 27
3.3. Turbulence Modeling . . . 27
3.4. Time Integration . . . 28
3.5. Numerical Method in ECOGEN . . . 29
3.6. Summary . . . 29

4. Code Implementations **31**
4.1. Flow solver CATUM . . . 31
4.2. Flow solver ECOGEN . . . 32

II. Cavitation Bubbles and their Dynamics **33**

5. Vapor Bubble containing Gas **35**
5.1. Motivation and Theory . . . 35
5.2. Set-up . . . 36
5.3. Results . . . 36
5.3.1. Energy Partitioning Model . . . 38
5.4. Summary . . . 40

6. Aspherical Bubble Collapse at Atmospheric Pressure **41**
6.1. Motivation . . . 41
6.2. Set-up . . . 42
6.3. Results . . . 43
6.3.1. Negative Stand-off Distance . . . 43
6.3.2. Positive Stand-off Distance . . . 45
6.4. Conclusions and Discussion . . . 47

7. Gas Bubble collapsing above a Crevice **49**
7.1. Motivation . . . 49
7.2. Set-up . . . 50
7.3. Results . . . 51
7.3.1. Considered Configurations . . . 51
7.3.2. Smooth wall . . . 52
7.3.3. Small Crevice . . . 55
7.3.4. Large Crevice . . . 57
7.3.5. Wall-detached Bubble . . . 60
7.3.6. Cavitation Erosion Potential . . . 62
7.4. Conclusion . . . 64

III. Cavitating Nozzle Flows with Injection into Gas **67**

8. Generic Step nozzle - Set-up and Validation **69**
8.1. Motivation . . . 69

8.2. Numerical Set-up 70
8.3. Comparison with experimental Data and Validation 72
8.4. Summary 73

9. Cavitation Dynamics and Shedding Mechanisms 75
9.1. Motivation 75
9.2. Developing Cavitation 77
9.3. Supercavitation 81
9.4. Characterization of the Shedding Processes 82
9.5. Schematics of the Cloud Shedding Process 83
9.6. Near-wall upstream Flow 84
9.7. Summary 87

10. Effects of Cavitation and Partial Gas Entrainment 89
10.1. Motivation 89
10.2. Effects on the Mass Flow 90
10.3. Collapsing Vapor Patterns 92
10.4. Effects on the Jet 95
10.5. Summary 97

IV. Concluding remarks 99

11. Summary & Outlook 101
11.1. Summary 101
11.2. Outlook 102

Bibliography 105

1. INTRODUCTION

1.1. CAVITATION PHENOMENA

Cavitation is a phenomenon in which local pressure drops beneath saturation pressure lead to the formation of vapor-filled cavities (Brennen, 1995; Franc and Michel, 2005). The static pressure drop can either be induced by a local flow acceleration or by applying an acoustic field. When subjected to higher pressure, these cavities suddenly re-condense and collapse. Several processes are associated with the collapse of a vapor structure, such as the formation of high-velocity micro-jets, the energy focusing resulting in very high temperatures and pressures inside the structures, and the emission of intense pressure waves. The latter can even damage nearby materials (Philipp and Lauterborn, 1998) or generate noise (McKenney and Brennen, 1994). Overall, cavitation with the formation and subsequent collapse of vapor structures plays an important role in a variety of applications.

Common examples affected by cavitation are ship propellers, hydraulic turbines and pumps, where material damage due to cavitation erosion and performance reduction are serious issues (Arndt, 1981). Other examples are flow configurations with restrictions in their cross-sectional area such as nozzles, wedges, valves and throttles in hydraulic systems. Of special technical relevance are injection systems, where cavitation can have desired and undesired effects. The most beneficial one is the promotion of primary jet break up and fuel atomization (Bergwerk, 1959; Reitz and Bracco, 1982). Since spray quality is one of the key parameters for combustion efficiency and reduction of pollutants, this can become a central aspect to fulfill future emission standards. Adverse effects are the reduction of mass flow (Bergwerk, 1959; Nurick, 1976) and cavitation erosion (Asi, 2006).

Although naturally occurring cavitation is mainly associated with negative effects, cavitation bubbles, on the other hand, are currently exploited to benefit from the intense pressure waves and the energy focusing. Examples are biomedical applications, such as urinary stone ablation (Pishchalnikov et al., 2003), drug delivery (Coussios and Roy, 2008) and needle-free injection with pressurized auto-injectors (Veilleux et al., 2018), and new technologies, such as surface-cleaning (Ohl et al., 2006; Reuter et al., 2017), micro-pumps in microfluidics (Dijkink and Ohl, 2008) and water treatment (Zupanc et al., 2012).

1.1.1. COLLAPSE DYNAMICS OF CAVITATION BUBBLES

The most generic phenomenon associated with cavitation is a spherical bubble collapse. Figure 1.1 shows the collapse and subsequent rebound of such a bubble. The first time instant depicts a bubble at its maximum expansion R_0. Due to the pressure imbalance between the bubble (saturation pressure p_{sat}) and the liquid (p_∞) $\Delta p = p_\infty - p_{sat}$, the bubble *collapses* with its interface being accelerated towards the center. Eventually, the bubble has completely condensed,

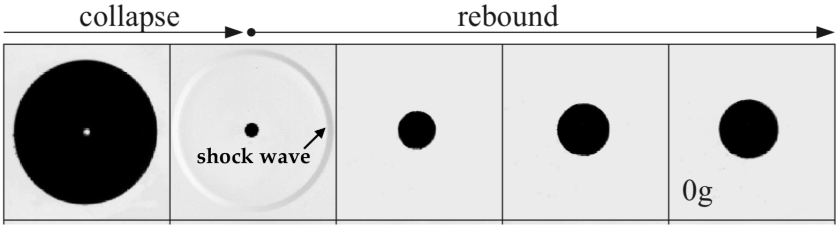

Figure 1.1.: Collapse and rebound of a spherical bubble in micro-gravity. Adapted from Tinguely et al. (2012) and reprinted with permission of the American Physical Society.

or is compressed to its minimum, which results in the abrupt stopping of the accelerated surrounding liquid and the emission of an intense pressure wave traveling outwards. Estimated peak pressures for collapses at atmospheric conditions are on the order of GPa (Pecha and Gompf, 2000; Akhatov et al., 2001; Supponen et al., 2017) and thus can cause material damage to nearby surfaces. After the collapse, the bubble can grow again, termed *rebound*. For a spherical collapse, the rebound is caused by gases inside the bubble expanding again after the collapse. The gases are present due to outgassing effects of gases dissolved in the liquid (Pollack, 1991; Freudigmann et al., 2017) and/or can be formed at bubble generation (Sato et al., 2013). Gases inside vapor bubbles not only affect the rebound but also dampen the emitted pressure waves (Rayleigh, 1917; Keller and Miksis, 1980; Akhatov et al., 2001).

In general, however, bubble collapses are not spherical since they are subjected to gravity and/or take place close to free and rigid surfaces, resulting in an aspherical collapse behavior and the formation of jets (Supponen et al., 2016). Of special relevance for material damage are collapses of bubbles close to a wall or attached to it. Figure 1.2 (a),(b) shows the schematics and an experimental time series of a wall-attached bubble collapse. In the beginning, a wall-directed micro-jet forms piercing the bubble. Then, the formed torus collapses emitting pressure waves, followed by a toroidal rebound. Figure 1.2 (c) visualizes the material damage induced by a single bubble collapse on an aluminum specimen. Both, the jet impact at the wall and the emitted pressure waves induce high pressure peaks. The micro-jet velocities are about $u_{jet} \approx 10 \times \sqrt{\Delta p/\rho_l}$ (Plesset and Chapman, 1971; Vogel et al., 1989; Philipp and Lauterborn, 1998) inducing a water-hammer pressure at the wall of $p_{WH} \approx u_{jet}\rho_l c_l$, where ρ_l and c_l are the density and the speed of sound in the liquid. Although this can be a high pressure peak, several studies concluded that the pressure waves at collapse with peak values of several GPa at atmospheric conditions are more decisive for the material damage (Philipp and Lauterborn, 1998; Lauer et al., 2012b).

Although bubble collapses have been excessively studied experimentally and numerically, there are still some aspects that have not yet been investigated or whose influences have not yet been fully clarified. One of these aspects is the influence of free gas inside a vapor bubble in case of an aspherical collapse. For spherical bubble collapses, it has already been analytically investigated (see above), while for more complex configurations the effect of the gas has not yet been clarified.

Another aspect is the sensitivity of the collapse dynamics to the driving pressure difference Δp. Experimental studies of bubble collapses are mostly performed under atmospheric conditions, while numerical studies mainly consider driving pressure differences of $10 - 100$ bar. At low

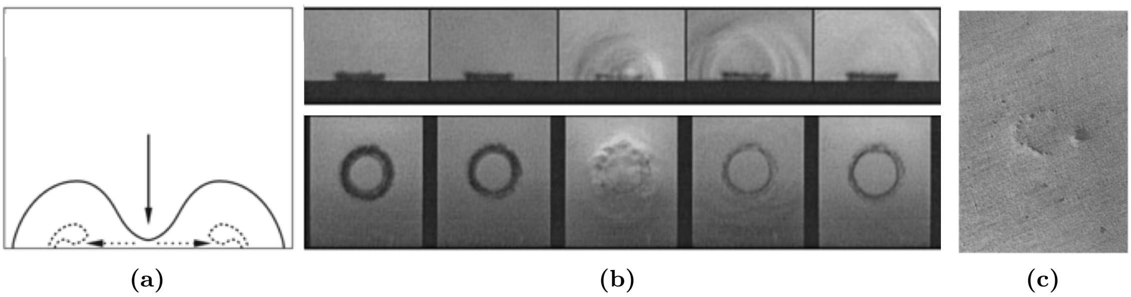
(a) (b) (c)

Figure 1.2.: Collapse of a wall-attached bubble. (a) Schematics by Lauer et al. (2012b), reprinted with permission of Elsevier. (b) Time series for $S/R_0 = 0.5$ in a side and top view, (c) Damage at aluminum specimen after single bubble collapse for $S/R_0 = 0.3$. (b) and (c) are by Philipp and Lauterborn (1998) and are reprinted with permission of Cambridge University Press.

driving pressures, rebound of the bubble is enhanced and effects of gas present in the bubble are more pronounced, which predestines atmospheric conditions for the investigation of these effects.

Furthermore, the effect of surface geometry is also an aspect deserving more attention. Previous studies have shown that a curved boundary (Tomita et al., 2002) or a triangular surface (Zhang et al., 2018) can qualitatively change the collapse behavior and thus also influence the erosion potential. In many technical and medical applications (see above), the characteristic length scale of the surface topology can be of the same order of magnitude as the bubble size, highlighting the importance of this aspect.

1.1.2. CAVITATING NOZZLE FLOWS

Cavitating nozzle flows are of significant technical relevance. Particularly with subsequent outflow into a gaseous ambient, such as in pressure atomizers or injector components, where cavitation can have beneficial and adverse effects. Figure 1.3 shows experimental data (Sou et al., 2014) of a cavitating nozzle flow with injection into gas for different cavitation regimes. The considered configuration of a step nozzle with one-sided constriction resembles a generic example of an injector. The cavitation tendency can be characterized with the dimensionless cavitation number σ, which is defined here as

$$\sigma = \frac{p_{out} - p_{sat}}{0.5\,\rho_l\,\bar{u}_l^2}\,, \tag{1.1}$$

where p_{out} denotes the pressure at the outlet, p_{sat} the saturation pressure of the liquid, ρ_l the mean density and $\bar{u}_l$ the mean velocity in stream-wise direction. With decreasing σ the cavitation tendency increases. At *developing cavitation* (Sou et al., 2007; Stanley et al., 2011) (operating points 2-4 in Fig. 1.3), it starts to cavitate in the detached shear layer, where the highest local velocity occurs, and spanwise cavitating vortices form. Increasing velocity, and hence cavitation, results in the formation of a vapor sheet with cloud detachment at the end of it. A further increase leads to *supercavitation* (Chaves et al., 1995) (operating point 5 in Fig. 1.3) with a vapor sheet almost spanning the entire nozzle length. In this regime, detached clouds collapse near

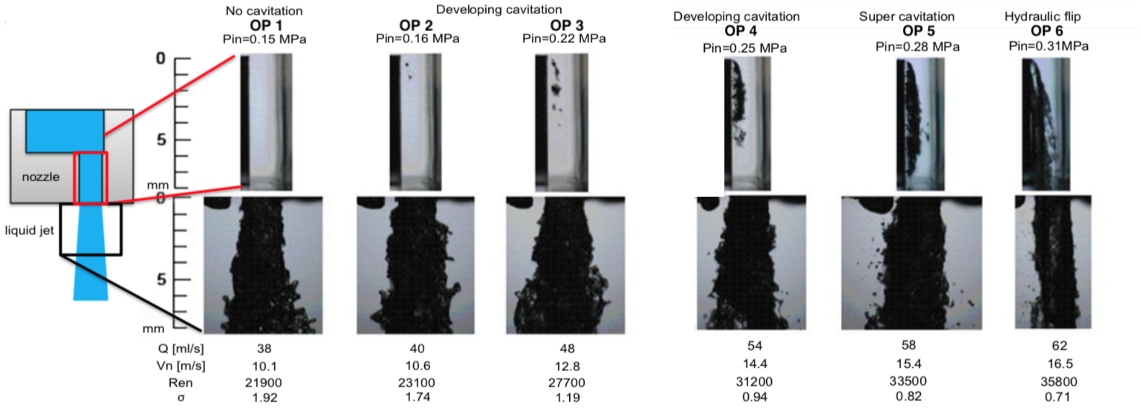
No cavitation
OP 1
Pin=0.15 MPa
Developing cavitation
OP 2
Pin=0.16 MPa
OP 3
Pin=0.22 MPa
Developing cavitation
OP 4
Pin=0.25 MPa
Super cavitation
OP 5
Pin=0.28 MPa
Hydraulic flip
OP 6
Pin=0.31MPa
0
5
mm
0
5
mm
nozzle
liquid jet
Q [ml/s]
Vn [m/s]
Ren
σ
38
10.1
21900
1.92
40
10.6
23100
1.74
48
12.8
27700
1.19
54
14.4
31200
0.94
58
15.4
33500
0.82
62
16.5
35800
0.71

Figure 1.3.: Cavitating nozzle flows for different cavitation regimes, increasing cavitation from left to right. Reprinted from Sou et al. (2014) with permission from Elsevier.

the nozzle outlet and intensify fluctuations there (Sou et al., 2007; Örley et al., 2015), or the clouds are transported to the nozzle outlet and create a pressure gradient from the outflow to the low-pressure vapor region, which results in gas being ingested by the nozzle (Örley et al., 2015). In this regime, strong cavitation causes an increased jet angle and an enhanced spray break-up; see Fig. 1.3. Further increase of the cavitation length can result in a complete flow detachment from the nozzle wall and the so-called hydraulic flip (Sou et al., 2007; Stanley et al., 2011) with a strong decrease in the jet angle; see operating point 6 in Fig. 1.3.

Cavitation processes, where vapor clouds are periodically shed from the main cavity, are termed *cloud cavitation* (Reisman et al., 1998; Laberteaux and Ceccio, 2001). This form of cavitation occurs in internal flows, as in the above described nozzle flows, Venturi nozzles or converging-diverging ducts with a rectangular cross-section (wedges) but is also common for cavitation on external bodies, such as hydrofoils. Le et al. (1993) proposed a schematic description for the periodic cloud shedding process on hydrofoils, see Fig. 1.4. The shedding process is initiated by the upstream motion of a disturbance. The common understanding is that a *re-entrant jet* (a thin liquid film underneath the cavity) causes this shedding. However, the shedding can be also triggered by a *bubbly condensation shock*. Even though this was already predicted by Jakobsen (1964), this mechanism had not been fully established and only recently several experimental investigations (Ganesh et al., 2016; Jahangir et al., 2018; Wu et al., 2017; Wang et al., 2017) and a numerical study (Budich et al., 2018) again emphasized it.

Figure 1.4 depicts a re-entrant jet governed shedding cycle with period T. During the first third of the cycle, the re-entrant jet develops. Then a cloud is shed and a new main cavity forms. Although many experimental and numerical studies have investigated re-entrant jets and their decisive role in cloud shedding (e.g. Kawanami et al. (1997); Furness and Hutton (1975); Stanley et al. (2014)), the driving mechanism behind the formation of the jet has not yet been clarified.

Despite the importance of orifices and nozzles with a constant cross-section in technical applications, detailed investigations of cavitation dynamics and shedding mechanisms have been far less performed than for external flows or flows in convergent-divergent geometries. Among the few conducted studies is the experimental work of Stanley et al. (2014) to cavitation dynamics

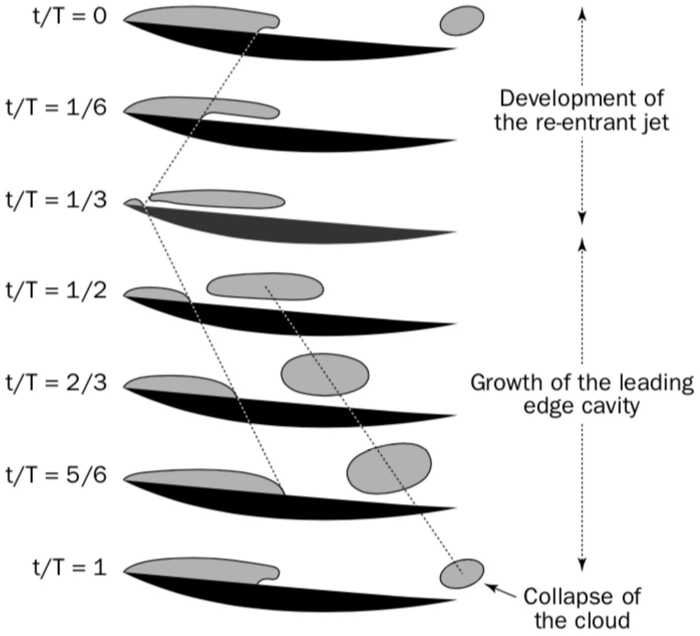

Figure 1.4.: Typical unsteady behavior of a partial cavity with the development of a re-entrant jet and the periodic shedding of cavitation clouds proposed by Le et al. (1993), reprinted from Franc et al., 2004 with permission granted by Springer Nature.

in circular nozzles, demonstrating the relevance of this aspect and pointing out differences to cavitation dynamics in other configurations.

The mentioned effects and interactions illustrate the importance of cavitation in nozzle flows. Some aspects are not yet clarified and are difficult to investigate experimentally, such as the interaction between cavitation, mass flow and partial gas entrainment into the nozzle. Numerical simulations can significantly contribute to understanding these processes. Once numerical methods have been validated, they can be used to study applications at conditions at which experiments are not possible, e.g. at high temperatures or pressures.

1.2. NUMERICAL INVESTIGATIONS

In the last decades, Computational Fluid Dynamics (CFD) have become a complementary approach to experimental studies for analyzing cavitation phenomena. Therefore, methods on different levels of computational complexity and accuracy have been developed. Depending on the considered configuration and the specific purpose of the simulation, a suitable modeling approach is chosen.

1.2.1. MODELING OF CAVITATING FLOWS

Physical modeling of cavitating flows is inherently challenging. A wide range of length and time scales is present and vapor structures exhibit strong volume changes due to growth or collapse.

Further, to capture the pressure waves emitted at collapse, a compressible approach is necessary.

The two-phase flow, consisting of the liquid and the vapor phase, can be either modeled with an Euler-Lagrangian approach or in a complete Eulerian framework with varying sets of equations. The occurring condensation and evaporation are associated with a mass transfer between the liquid and the vapor, which has to be modeled. Computational feasibility imposes further constraints on the modeling, especially for multi-component flows in complex configurations.

In the following, an overview of mass transfer models is given and then multi-phase models are presented, focusing on Eulerian single-fluid models.

MASS TRANSFER MODELS

Mass transfer at condensation and evaporation is either incorporated by finite-rate mass transfer models or thermodynamic equilibrium is assumed.

Finite-rate mass transfer models employ a corresponding finite source term. These models are often derived from bubble dynamics using the Rayleigh-Plesset equation, e.g. Singhal et al. (2002); Schnerr and Sauer (2001), and contain semi-empirical parameters that have to be calibrated. These configuration-specific parameters and their evaluation represent a disadvantage of that approach, limiting its general applicability.

Assuming that equilibrium is reached immediately, the mass transfer rate can be modeled as infinite and no additional modeling parameters are necessary. This approach was first suggested by Schmidt et al. (2006) and Koop (2008) and the underlying assumption is justified for most technical applications. Koukouvinis et al. (2017) have demonstrated that for developing cavitation occurring in large scale step nozzles an equilibrium cavitation model leads to comparable cavitation development and volume fraction distribution as a finite-rate mass transfer model. Without any tuning and adaptations, this model can be applied to various cavitation regimes (Egerer et al., 2014).

Additionally, phase transition can be neglected, if no further evaporation is expected and it can be assumed that the overall dynamics are not sensitive to the modeling of the gaseous phase. This is the case, for example, for bubble or bubble-cloud collapses that are exposed to high driving pressure differences.

EULER-LAGRANGIAN APPROACHES

In Euler-Lagrangian approaches, the liquid is modeled as a continuous carrier phase in an Eulerian frame of reference, while single vapor bubbles or parcels of bubbles are tracked in a Lagrangian way using the Rayleigh-Plesset equation for growth and collapse, as in e.g. Giannadakis et al. (2008); Shams et al. (2011); Sou et al. (2014) and more recently in Ghahramani et al. (2019). These models are especially well-suited for incipient cavitation and are generally embedded in an incompressible framework.

EULERIAN SINGLE-FLUID MODELS

In Eulerian approaches all phases are described in an Eulerian frame of reference. The straight forward approach is to solve an individual set of transport equations for each phase. However, because this involves high computational effort, two-phase flows are often modeled by a single mixture fluid, assuming mechanical equilibrium and neglecting slip velocities and pressure jumps at the phase boundaries. To account for imbalances, additional transport equations have to be included. For the interface capturing, suitable parameters are transported. The following approaches have been established:

- Transport of *volume fraction*

  The volume fraction of the second phase is transported. This procedure is well suited for incompressible solvers (Singhal et al., 2002; Bensow and Bark, 2010) and can also be applied to multi-phase/multi-component flows (Kunz, 2000; Singhal et al., 2002; Ji et al., 2010; Edelbauer, 2017). For compressible solvers, the mass transport equation of each phase has to be additionally included to avoid pressure fluctuations at the phase boundaries (see e.g. Abgrall (1996); Shyue (1998)), resulting in so-called *five-equation models* (Allaire et al., 2002; Perigaud and Saurel, 2005; Kapila et al., 2001). Saurel et al. (2009) proposed a *pressure-disequilibrium* model to improve and stabilize the model of Kapila et al. (2001), where the energy equation of each phase has to be considered. All these volume fraction approaches can improve the interface capturing by geometric reconstruction such as Piecewise Linear Interface Computation (PLIC), e.g. (Parker and Youngs, 1992), or the Tangent of Hyperbola for INterface Capturing (THINC) (Xiao et al., 2005; Shyue and Xiao, 2014). Furthermore, a reconstruction of the phase interface normal vector allows the inclusion of surface tension effects (Brackbill et al., 1992). Although phase transfer can be considered in these models, it is usually neglected in compressible realizations.

- Transport of *mass fraction* or a suitable material property

  The mass fraction of the second phase is transported. This approach, proposed by Shyue (1998), can be applied directly to compressible methods without additional transport equations. Alternatively to the mass fraction, a suitable material property can be advected, see e.g. Johnsen and Colonius (2009). The thermodynamic closure requires special attention in all these approaches. Phase transfer can be taken into account.

- *Thermodynamic-equilibrium cavitation model*

  Using thermodynamic equilibrium cavitation models (Schmidt et al., 2006), the two-phase flow of a liquid and its liquid-vapor mixture can be entirely described with a single-fluid and no additional transport equations are necessary. The model is suitable for compressible methods and includes phase transition. Its intrinsic modeling of sub-grid scales and processes on the sub-grid level makes it particularly suitable for Large-eddy simulations (Schmidt et al., 2014).

MULTI-COMPONENT MODELS

In the scope of this work, multi-phase flows consisting of a cavitating liquid and an additional gas phase are of interest. These flows are also referred to as three-phase flows. In general, multi-phase/multi-component modeling can be achieved by adding an additional component to the above mentioned approaches. However, the extension of five, six or seven equation models, such as in Wang et al. (2014), can lead to computationally intensive models that are only suitable for 2-D studies and not for complex 3-D simulations. The most established method for cavitating multi-component flows is the extension of a thermodynamic equilibrium cavitation model by an additional gas component, first proposed by Mihatsch (2017) and implemented and applied by Trummler (2014) and Örley et al. (2015). Since the gas mass fraction is transported, no additional transport equations have to be considered for a compressible treatment. Thermodynamic closure is realized with a coupled, barotropic equation of state. Many research groups have taken up the model and partly modified it. Örley et al. (2016) extended the model to employ different equations of state for the individual components; Mithun et al. (2018) added a volume-of-fluid method for interface capturing; Brandao et al. (2020) considered a finite-rate mass transfer for the cavitation process.

1.2.2. SIMULATIONS OF COLLAPSING BUBBLES

About ten years ago, several research groups have started to use compressible finite volume flow solvers to study aspherical bubble collapses in the vicinity of a wall. Considering compressibility allows for capturing the emitted shockwave and the assessment of the erosion potential. One of the first high-resolution studies was conducted by Johnsen and Colonius (2009), who examined the collapse behavior and induced wall pressures of collapsing wall-detached bubbles. Later, Lauer et al. (2012b) simulated collapsing wall-attached and detached bubbles. Both references employed a higher-order shock and interface capturing scheme. However, they used different thermodynamic models and Lauer et al. (2012b) considered condensation, contrary to Johnsen and Colonius (2009), and included a level set method for sharp interfaces.

Recent research focused on thermal effects at collapses, as collapse associated temperature peaks (Beig et al., 2018), the effect of thermodynamic models (Kyriazis et al., 2018), and the effect of viscoelasticity (Rodriguez and Johnsen, 2019). Other topics of current research are the inclusion of the bubble growth phase in the simulations (Lauterborn et al., 2018; Lechner et al., 2019) and the effect of bubble shapes at maximum expansion such as an initial ellipsoidal shape (Pishchalnikov et al., 2019).

Moreover, not only near-wall single bubble collapses have been investigated, but also multi-bubble configurations, as arrays of collapsing bubbles (Lauer et al., 2012a), collapsing gas-bubble clouds (Tiwari et al., 2015; Rasthofer et al., 2019) and vapor bubble clouds (Schmidt, 2015; Mihatsch, 2017; Ogloblina et al., 2018).

Single-fluid models are commonly used for these investigations and mostly the bubble content is modeled as non-condensable. The liquid phase is either described by a stiffened-gas equation or a modified Tait equation. The phase distinction between liquid and gaseous phase is achieved by transport of material properties or five- and six-equation models. Such models are also available in the open-source codes ECOGEN[1] and MFC[2], and have been implemented in OpenFOAM[3]. Several studies, on the other hand, also included phase transition as Lauer et al. (2012b) and Ochiai et al. (2011). The latter study was the first to numerically reproduce the rebound and the second collapse with a compressible simulation. Sezal (2009) and Schmidt (2015) suggested the single-fluid equilibrium cavitation model for simulations of bubble collapses and Pöhl et al. (2015); Örley (2016); Koukouvinis et al. (2016a) have demonstrated that this model leads to comparable results to the ones obtained by Lauer et al. (2012b).

---

[1] https://code-mphi.github.io/ECOGEN/

[2] https://mfc-caltech.github.io

[3] http://sourceforge.net/projects/openfoam-extend/files/foam-extend-3.0/

The results of numerical simulations depend on various parameters. For the intensity of the emitted pressure peaks the following aspects are relevant: the numerical scheme (Egerer et al., 2016), the grid resolution (Schmidt et al., 2014), the thermodynamic model and the modeling of the bubble content (Pishchalnikov et al., 2019; Trummler et al., 2018a). Whereas the bubble dynamics are only weakly sensitive to these aspects. A grid resolution of about 100 cells over the maximum radius R_0 can be considered as state of the art (Lauer et al., 2012b). The highest resolutions reported are 200 cells/R_0 for 3-D (Beig et al., 2018) and 1600 cells/R_0 for 2-D axisymmetric simulations (Koch et al., 2017).

1.2.3. SIMULATIONS OF CAVITATING FLOWS

Numerical simulations of cavitating flows were initially carried out to analyze cavitation dynamics, especially on hydrofoils. For these investigations mainly Eulerian single-fluid models were used, differing in the modeling of the mass transfer. The first studies include 2-D investigations of Singhal et al. (2002) and Coutier-Delgosha et al. (2007) and subsequent 3-D investigations of e.g. twisted hydrofoils of Schnerr et al. (2008) and Koop and Hoeijmakers (2009). Fully compressible, time-resolved simulations enable the assessment of the transient and relevant physical processes such as the emitted pressure waves during collapse (Schmidt et al., 2006). Further, Large-eddy simulations (LES) are used to consider the effect of unresolved turbulent structures. Using LES, cavitation dynamics on hydrofoils (Huang et al., 2014; Ji et al., 2015), propellers (Bensow and Bark, 2010) (incompressible), wedges (Dittakavi et al., 2010; Gnanaskandan and Mahesh, 2016), and in nozzles (Duke et al., 2013; Egerer et al., 2014) were investigated.

Nowadays, cavitation processes in nozzles and orifices are often subject of numerical investigations because of their importance in many technical applications. Depending on the cavitation regime and focus of the investigation, compressible or incompressible approaches and different cavitation models are employed. Incipient cavitation was studied by Shams et al. (2011) and Sou et al. (2014) using an incompressible approach coupled with an Eulerian-Lagrangian two-phase model. Focusing on the cavitation dynamics, He et al. (2016) and Edelbauer (2017) employed incompressible models with finite-rate mass transfer cavitation models. For the investigation of various cavitation regimes, Egerer et al. (2014) and Örley et al. (2015) used a single-fluid equilibrium model with a compressible approach. Studies aiming to predict cavitation erosion (Örley et al., 2016; Koukouvinis et al., 2016b; Beban, 2019; Cristofaro et al., 2019) generally use compressible LES. Albeit, recently Schenke and van Terwisga (2019) proposed an energy conservative method to predict the erosive aggressiveness applicable to incompressible approaches.

Cavitating nozzle flows often occur upstream to an outflow into a gaseous environment. To investigate such configurations and the interactions between cavitation and jet break-up, full configuration simulations including the cavitating nozzle flow and the jet are best suited (Örley et al., 2015; Edelbauer, 2017; Mithun et al., 2018). These studies can reveal deeper insight into the underlying physical processes. At the moment, most of these studies aim to validate the multi-component modeling approach to be afterwards applied to more realistic geometries and conditions.

1.3. SCOPE OF THE THESIS

Cavitation phenomena and processes affect a wide range of applications and involve varying mechanisms and effects, which are not all completely understood yet. This thesis aims to elucidate some of them using numerical investigations. To this end, the academic flow solvers CATUM (CAvitation Technical University Munich) and ECOGEN are employed.

Firstly, the focus is on cavitation bubbles and their dynamics. The following aspects are investigated:

- Effect of non-condensable gas inside a vapor bubble on the collapse dynamics and pressure impact. For this investigation, a modification to the multi-component model by Örley et al. (2015) is proposed and implemented in CATUM. The effect of gas on the rebound and the intensity of the shock wave is validated with the energy partitioning model by Tinguely et al. (2012).
- Bubble dynamics and induced pressure peaks at collapses under atmospheric conditions. Using the flow solver CATUM, simulations of collapsing wall-attached bubbles are performed. Pure vapor bubbles and vapor-gas bubbles are considered to additionally assess the effect of gas in these configurations.
- Effect of notched walls on the collapse dynamics and erosion potential. Using the CFD tool ECOGEN, the collapse behavior of gas bubbles close to walls with a cylindrical crevice is investigated.

Secondly, cavitating nozzle flows with injection into gas are investigated. For this purpose, the multi-component model by Örley et al. (2015) is used and applied to wall-resolved LES performed with CATUM. The simulation results provide the basis for the following main objectives:

- Validation of the thermodynamic multi-component model combined with the implicit LES approach by Egerer et al. (2016) with experimental flow field data.
- Detailed analysis of the cavitation dynamics and shedding mechanisms in cavitating nozzle flows featuring re-entrant jet and condensation shock governed shedding.
- Evaluation of the impact of cavitation and gas entrainment on the jet characteristics, mass flow and erosion potential.

1.4. OUTLINE

This thesis is divided into four parts. Part I introduces the physical and numerical methods. Chapter 2 presents the governing equations and the modeling of the multi-component flows. In Chapter 3 the numerical method is described. The two flow solvers CATUM and ECOGEN are briefly presented in Chapter 4.

Part II contains numerical studies of cavitation bubbles. First, the effect of free non-condensable gas inside a vapor bubble is numerically assessed in Chapter 5. Then, in Chapter 6, the collapse behavior of wall-attached bubbles at atmospheric conditions is analyzed. Additionally, simulations of bubbles containing vapor and an additional small amount of non-condensable gas are also presented. In Chapter 7, near-surface dynamics of a collapsing gas bubble above a cylindrical crevice are scrutinized.

Part III focuses on Large-eddy simulations of cavitating nozzle flows with injection into gas using a multi-component model. First, in Chapter 8, the computational set-up is presented and the results are validated against experimental data. Afterwards, in Chapter 9, the cavitation dynamics and shedding mechanisms of cavitating nozzle flows featuring different cavitation regimes are analyzed in detail. The effects of the cavitating nozzle flow and cavitation induced partial gas entrainment into the nozzle on the jet characteristics are investigated in Chapter 10.

Finally, Chapter 11 summarizes the main findings and gives an outlook for future studies.

Part I.

PHYSICAL AND NUMERICAL MODEL

2. PHYSICAL MODEL

In this chapter, the physical model is introduced by presenting the governing equations and the thermodynamic closure relations. First, the physical fundamentals are discussed and afterwards the two employed modeling approaches are described. CATUM contains a multi-component model for cavitating liquids and an additional gas component. ECOGEN employs a model accounting for pressure-disequilibrium at phase boundaries. Both models are based on single-fluid approaches with different assumptions for equilibrium, phase transfer and viscosity.

2.1. GOVERNING EQUATIONS

We consider the fully compressible Navier-Stokes equations in conservative form

$$\partial_t \boldsymbol{U} + \nabla \cdot \boldsymbol{F}(\boldsymbol{U}) = 0\,, \tag{2.1}$$

representing the transport equation of the state vector $\boldsymbol{U}$ with the physical, non-linear flux $\boldsymbol{F}(\boldsymbol{U})$. For later convenience, $\boldsymbol{F}$ can be split into its convective part $\boldsymbol{C}$, and surface stresses due to pressure $\boldsymbol{P}$, and viscous forces $\boldsymbol{D}$ as

$$\partial_t \boldsymbol{U} + \nabla \cdot [\boldsymbol{C}(\boldsymbol{U}) + \boldsymbol{P}(\boldsymbol{U}) + \boldsymbol{D}(\boldsymbol{U})] = 0 \tag{2.2}$$

with

$$\boldsymbol{U} = \begin{bmatrix} \rho \\ \rho \boldsymbol{u} \\ \rho E \end{bmatrix} \quad \boldsymbol{C}(\boldsymbol{U}) = \boldsymbol{u} \begin{bmatrix} \rho \\ \rho \boldsymbol{u} \\ \rho E + p \end{bmatrix} \quad \boldsymbol{P}(\boldsymbol{U}) = p \begin{bmatrix} 0 \\ \boldsymbol{I} \\ 0 \end{bmatrix} \quad \boldsymbol{D}(\boldsymbol{U}) = - \begin{bmatrix} 0 \\ \boldsymbol{\tau} \\ \boldsymbol{\tau} \boldsymbol{u} - \boldsymbol{q} \end{bmatrix}. \tag{2.3}$$

Equation (2.2) contains the transport equations for mass, momentum and total energy of the considered fluid. ρ, $\boldsymbol{u}$ and p are density, velocity and pressure, respectively. The total energy E is composed of internal energy e and kinetic energy

$$E = e + \frac{1}{2}\|\mathbf{u}\|^2. \tag{2.4}$$

$\boldsymbol{\tau}$ is the viscous stress tensor

$$\boldsymbol{\tau} = \mu(\nabla \boldsymbol{u} + (\nabla \boldsymbol{u})^T - \frac{2}{3}(\nabla \cdot \boldsymbol{u})\boldsymbol{I}), \tag{2.5}$$

with the unit tensor $\boldsymbol{I}$ and the dynamic viscosity μ. The heat flux $\boldsymbol{q}$ is calculated by

$$\boldsymbol{q} = -\lambda \nabla T, \tag{2.6}$$

where λ is the thermal conductivity and T the static temperature. For the inviscid Euler equations, the term $\boldsymbol{D}$ is omitted. These governing equations are solved with a thermodynamic closure relation for the pressure $p = p(\rho, e)$ and, if applicable, relations for the viscosity μ and the thermal conductivity λ.

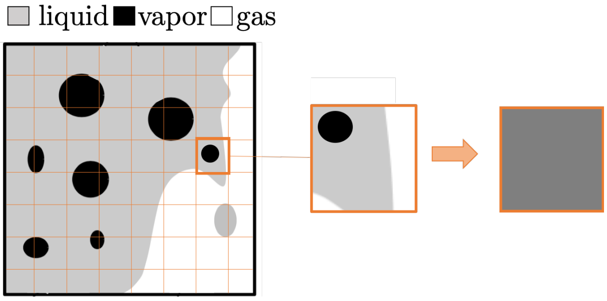

Figure 2.1.: Schematics for the single-fluid model visualizing the physical situation with the numerical discretization (left) and the generic modeling in one grid cell (right), adapted from Örley et al. (2015).

2.2. SINGLE-FLUID MODEL

Figure 2.1 depicts a sketch of a multi-component flow composed of a liquid (l), its vapor component (v) and gas (g). In the employed finite volume method (Chapter 3), the flow domain is discretized into finite volumes - *cells*. Within a cell, each component $\mathbf{\Phi} = \{l, v, g\}$ is defined by its state variables $\rho_\Phi, \boldsymbol{u}_\Phi, p_\Phi, T_\Phi, e_\Phi$, and its volume β_Φ and mass fraction ξ_Φ

$$\beta_\Phi = \frac{V_\Phi}{V} \quad \text{and} \quad \xi_\Phi = \frac{m_\Phi}{m} \tag{2.7}$$

of the cell volume V with mass m. The most general way to describe such a flow is to solve for each component $\mathbf{\Phi}$ an individual set of transport equations for mass, momentum and total energy (Eq. (2.2)). However, such an approach implies high computational expenses and to minimize these efforts, multi-component flows are often modeled by a single mixture fluid defined by cell-averaged mixture quantities ρ, p, $\boldsymbol{u}$, T, e. Assuming mechanical and thermodynamic equilibrium within a finite cell volume, the pressure acting on each component is the mixture pressure $p_\Phi = p$, slip velocity is neglected $\boldsymbol{u}_\Phi = \boldsymbol{u}$ and the temperature for all components is identical $T_\Phi = T$. The volume-averaged density is computed as

$$\rho = \sum_\Phi \beta_\Phi \rho_\Phi . \tag{2.8}$$

Further, sub-cell phase interfaces are not reconstructed and surface tension is neglected.

An overview of singe-fluid models can be found in the introduction (Section 1.2). In the scope of this work, we employ the multi-component model proposed by Örley et al. (2015), described in Section 2.3, and the pressure-disequilibrium model of Saurel et al. (2009), described in Section 2.4.

2.3. EQUILIBRIUM CAVITATION MODEL FOR MULTI-COMPONENT FLOWS

More detailed descriptions of this model can be found in Mihatsch (2017); Trummler (2014); Örley et al. (2015); Trummler et al. (2018c).

2.3.1. GOVERNING EQUATIONS

For this model, the governing equations are the compressible Navier-Stokes equations plus the transport of the gas mass fraction $\rho\xi_g$

$$\partial_t \boldsymbol{U} + \nabla \cdot [\boldsymbol{C}(\boldsymbol{U}) + \boldsymbol{P}(\boldsymbol{U}) + \boldsymbol{D}(\boldsymbol{U})] = 0 \tag{2.9}$$

with

$$\boldsymbol{U} = \begin{bmatrix} \rho \\ \rho\boldsymbol{u} \\ \rho\xi_g \end{bmatrix} \quad \boldsymbol{C}(\boldsymbol{U}) = \boldsymbol{u} \begin{bmatrix} \rho \\ \rho\boldsymbol{u} \\ \rho\xi_g \end{bmatrix} \quad \boldsymbol{P}(\boldsymbol{U}) = p \begin{bmatrix} 0 \\ \boldsymbol{I} \\ 0 \end{bmatrix} \quad \boldsymbol{D}(\boldsymbol{U}) = - \begin{bmatrix} 0 \\ \boldsymbol{\tau} \\ 0 \end{bmatrix}, \tag{2.10}$$

where ρ, $\boldsymbol{u}$ and p are the density, velocity, and pressure of the representative mixture fluid. Since the assumed thermodynamic closure relation for the pressure is a function of the density and the gas mass fraction $p = p(\rho, \xi_g)$, the energy equation can be omitted. The thermodynamic closure is presented in Section 2.3.2 and the evaluation of the mixture viscosity μ for the viscous stresses τ is described in Section 2.3.3.

2.3.2. THERMODYNAMIC CLOSURE RELATION

First, we derive an equation of state (EOS) for the cavitating liquid and the gas component individually and afterward combine them to a coupled EOS. For the application to vapor bubbles containing gas, we propose a small modification.

CAVITATING LIQUID

We employ a thermodynamic equilibrium cavitation model, where finite-rate mass transfer terms are avoided. The liquid starts to cavitate if the pressure drops beneath saturation pressure p_{sat}

$$p < p_{\text{sat}} \tag{2.11}$$

and then a liquid-vapor mixture is present, denoted with subscript m. For instantaneous phase change in local thermodynamic equilibrium, the densities of liquid and vapor are their saturation densities $\rho_l = \rho_{\text{sat},l}$, $\rho_v = \rho_{\text{sat},v}$. Thus, the vapor volume fraction $\alpha \equiv \beta_v$ is given by the density of the liquid-vapor mixture ρ_m as

$$\alpha = \frac{\rho_{\text{sat},l} - \rho_m}{\rho_{\text{sat},l} - \rho_{\text{sat},v}}. \tag{2.12}$$

For water at reference temperature T = 293.15 K, the corresponding values are $p_{\text{sat}} = 2340\,\text{Pa}$, $\rho_{\text{sat},l} = 998.1618\,\text{kg/m}^3$ and $\rho_{\text{sat},v} = 17.2 \cdot 10^{-3}\,\text{kg/m}^3$.

An equation of state for the pure liquid and the two-phase region can be derived from the definition of the isentropic (entropy $s = \text{const.}$) speed of sound c

$$c = \sqrt{\left.\frac{\partial p}{\partial \rho}\right|_{s=\text{const.}}}. \tag{2.13}$$

Assuming an approximately constant speed of sound in the liquid region and also in the two-phase region, one can integrate Eq. (2.13) for each region starting from saturation density $\rho_{\mathrm{sat},l}$ to obtain a linearized relation between density and pressure valid in both regions

$$\rho_{lm} = \rho_{\mathrm{sat},l} + \frac{1}{c^2}(p - p_{\mathrm{sat}}) \;\text{ with }\; c = \begin{cases} c_l & \text{if} \quad p \geq p_{\mathrm{sat}} \\ c_m & \text{if} \quad p < p_{\mathrm{sat}} \end{cases} . \tag{2.14}$$

Here, the subscript lm indicates that both regions, the liquid and the two-phase mixture region, can be described with this correlation. In the liquid region ($p \geq p_{\mathrm{sat}}$), the speed of sound is $c = c_l = 1482.35\,\mathrm{m/s}$, while in the liquid-vapor mixture ($p < p_{\mathrm{sat}}$) we adopt $c_m = 1\,\mathrm{m/s}$, following Örley et al. (2015). This value lies in between the equilibrium speed of sound $c_{m,\mathrm{eq}}$ and the frozen speed of sound $c_{m,\mathrm{frozen}}$ for $\alpha = 0.5$, which are $c_{m,\mathrm{eq}} = 0.08\,\mathrm{m/s}$ and $c_{m,\mathrm{frozen}} = 3\,\mathrm{m/s}$ (Franc and Michel, 2005), and thus should be a good representation of the speed of sound considering phase-change (Brennen, 1995; Budich et al., 2018).

NON-CONDENSABLE GAS COMPONENT

The non-condensable gas-phase is modeled as an isothermal ideal gas

$$\rho_g = \frac{p}{\mathrm{R}T}, \tag{2.15}$$

with the reference temperature $T = 293.15\,\mathrm{K}$ and the specific gas constant $\mathrm{R} = 287.06\,\mathrm{J/(kg \cdot K)}$.

COMBINED EOS FOR MULTI-COMPONENT FLOW

To obtain a closed-form equation of state for the cavitating liquid and the gas, the individual closure relations Eqs. (2.14) and (2.15) are combined via the definition of the average density Eq. (2.8)

$$\rho = \beta_{lm}(\rho_{sat} + \frac{1}{c^2}(p - p_{sat})) + \beta_g \frac{p}{\mathrm{R}T} \quad \text{with} \quad c = \begin{cases} c_l & p \geq p_{sat} \\ c_m & p < p_{sat} \end{cases} \tag{2.16}$$

Using $\sum_\Phi \beta_\Phi = 1$ and $\beta_\Phi = \xi_\Phi \frac{\rho}{\rho_\Phi}$, the volume fractions can be expressed as functions of p, ξ_g

$$\beta_{lm} = 1 - \beta_g \qquad \beta_g = \xi_g \frac{\rho}{\rho_g} = \xi_g \frac{\rho \mathrm{R}T}{p}, \tag{2.17}$$

which yields to

$$\rho = \left(1 - \xi_g \frac{\rho \mathrm{R}T}{p}\right)\left(\rho_{sat} + \frac{1}{c^2}(p - p_{sat})\right) + \xi_g \rho, \tag{2.18}$$

and subsequently to

$$p^2 + p(c^2\rho_{sat} - p_{sat} - \rho\xi_g RT - \rho c^2(1 - \xi_g)) - (c^2\rho_{sat} - p_{sat})\rho\xi_g RT = 0. \tag{2.19}$$

The pressure p is obtained by solving this quadratic equation. First, Eq. (2.19) is solved for $c = c_l$ and if no solution is found, this step is repeated for $c = c_m$.

MODIFICATION FOR VAPOR BUBBLE CONTAINING GAS

For a vapor bubble containing free gas, the above described combined EOS has to be slightly modified. In a vapor bubble containing gas, the pressure in the bubble is (see e.g. Rayleigh (1917))

$$p_{bubble} = p_v + p_g. \tag{2.20}$$

Thus, the pressure acting on the liquid-vapor mixture has to be treated differently. Using Dalton's law, the partial gas pressure can be expressed as

$$p_g = \beta_g \, p \tag{2.21}$$

and we approximate the pressure acting on the liquid-vapor mixture with

$$p_{lm} = p - p_g = (1 - \beta_g) \, p. \tag{2.22}$$

Again, a coupled EOS gives the pressure as a function of the average density and the gas mass fraction $p = p(\rho, \xi_g)$ and is obtained by expressing the densities ρ_Φ with the corresponding thermodynamic relations Eqs. (2.14) and (2.15). For this application, we consider a mixture speed of sound closer to the equilibrium value with $c_m = 0.1\,\mathrm{m/s}$. The coupled EOS is solved as described above.

2.3.3. RELATION FOR DYNAMIC VISCOSITY

For wall-bounded cavitating flows, the viscosity plays a central role. Since the dynamic viscosity of pure liquids is about 100 times larger than for vapor, the modeling of the mixture viscosity is non-trivial. Consequently, depending on the considered configuration, different approaches are employed to determine the mixture viscosity for the liquid-vapor mixture μ_{lm}.

For cavitating nozzle flows, we model the dynamic viscosity of the liquid-vapor mixture μ_{lm} as proposed by Beattie and Whalley (1982) with

$$\mu_{lm} = \alpha \cdot \mu_v + (1 - \alpha)(1 + \frac{5}{2}\alpha) \cdot \mu_l. \tag{2.23}$$

μ_v, μ_l denote the viscosity of the vapor and liquid, respectively. In a fluid containing solid particles, the viscosity increases for small volume fractions of particles. Assuming that small vapor bubbles have a comparable effect, Eq. (2.23) resembles this increase for small values of α. Dittakavi et al. (2010); Hickel et al. (2011); Egerer et al. (2014); Örley et al. (2016) employed the same approach for cavitating nozzle flows. For a detailed study of the effect of viscosity modeling on the vapor distribution and collapse intensity can be found in the master's thesis of Rahn (2017).

For the simulations of bubbles, on the other hand, the phase boundary is well resolved and we use a linear blending with the volume fractions

$$\mu_{lm} = \alpha \cdot \mu_v + (1 - \alpha) \cdot \mu_l. \tag{2.24}$$

Finally, the viscosity of the representing mixture fluid μ is approximated with the volume-averaged viscosity as

$$\mu = \beta_g \cdot \mu_g + (1 - \beta_g) \cdot \mu_{lm}. \tag{2.25}$$

The following values for the viscosities are used: $\mu_l = 1.002 \cdot 10^{-3}\,\mathrm{Pa\,s}$, $\mu_v = 9.272 \cdot 10^{-6}\,\mathrm{Pa\,s}$ and $\mu_g = 1.837 \cdot 10^{-5}\,\mathrm{Pa\,s}$.

2.4. PRESSURE-DISEQUILIBRIUM MODEL

2.4.1. GOVERNING EQUATIONS

The pressure-disequilibrium model by Saurel et al. (2009) can be expressed as

$$\partial_t \boldsymbol{U} + \nabla \cdot [\boldsymbol{C}(\boldsymbol{U}) + \boldsymbol{P}(\boldsymbol{U})] + \boldsymbol{h}(\boldsymbol{U}) \nabla \cdot \boldsymbol{u} = \boldsymbol{r}(\boldsymbol{U})\,, \tag{2.26}$$

with the state vector $\boldsymbol{U}$, the flux composed of a convective part $\boldsymbol{C}$ and a pressure part $\boldsymbol{P}$, and the non-conservative terms $\boldsymbol{h}$ and $\boldsymbol{r}$. $\boldsymbol{h}$ contains additional pressure terms and $\boldsymbol{r}$ is for the pressure relaxation. For a two-component flow $\Phi = \{l, g\}$, these are

$$\boldsymbol{U} = \begin{bmatrix} \beta_l \\ \beta_l \rho_l \\ \beta_g \rho_g \\ \rho \boldsymbol{u} \\ \beta_l \rho_l e_l \\ \beta_g \rho_g e_g \\ \rho E \end{bmatrix}, \; \boldsymbol{C} = \boldsymbol{u} \begin{bmatrix} \beta_l \\ \beta_l \rho_l \\ \beta_g \rho_g \\ \rho \boldsymbol{u} \\ \beta_l \rho_l e_l \\ \beta_g \rho_g e_g \\ (\rho E + p) \end{bmatrix}, \; \boldsymbol{P} = p \begin{bmatrix} 0 \\ 0 \\ 0 \\ \boldsymbol{I} \\ 0 \\ 0 \\ 0 \end{bmatrix}, \; \boldsymbol{h} = \begin{bmatrix} -\beta_l \\ 0 \\ 0 \\ \boldsymbol{0} \\ \beta_l p_l \\ \beta_g p_g \\ 0 \end{bmatrix}, \; \boldsymbol{r} = \begin{bmatrix} \kappa(p_l - p_g) \\ 0 \\ 0 \\ \boldsymbol{0} \\ -\kappa p_I (p_l - p_g) \\ \kappa p_I (p_l - p_g) \\ 0 \end{bmatrix}, \tag{2.27}$$

where β_Φ, ρ_Φ, p_Φ and e_Φ are the volume fraction, density, pressure and internal energy of phase $\Phi = \{l, g\}$, respectively. The mixture density ρ is given by Eq. (2.8), the pressure is analogously

$$p = \sum_\Phi \beta_\Phi p_\Phi, \tag{2.28}$$

and for the total energy $E = e + \frac{1}{2}\|\mathbf{u}\|^2$ the mixture internal energy is

$$e = \sum_\Phi \xi_\Phi e_\Phi. \tag{2.29}$$

Further, κ in Eq. (2.27) denotes the pressure-relaxation coefficient and p_I the interfacial pressure with

$$p_I = \frac{I_g p_l + I_l p_g}{I_l + I_g}, \tag{2.30}$$

where $I_\Phi = \rho_\Phi c_\Phi$ is the acoustic impedance. Here, the mass transport equation for each component, the transport of the volume fraction of one component and the momentum equation for the mixture fluid are considered. Due to the pressure disequilibrium, the internal energy equation for each phase is included. Nevertheless, the conservation of the total energy is additionally solved to ensure numerical conservation and correct treatment of shock waves, see Saurel et al. (2009).

The pressure-relaxation is achieved by an infinite-relaxation procedure, which first solves the non-relaxed, hyperbolic equations ($\kappa \to 0$), and then relaxes the disequilibrium pressures for $\kappa \to +\infty$. The relaxation procedure is combined with a re-initialization procedure at each time-step step. Thereby convergence to the 5-equation mechanical-equilibrium model by Kapila et al. (2001) is ensured, see Schmidmayer et al. (2020).

2.4.2. THERMODYNAMIC CLOSURE RELATION

The closure is with individual equations of state for each component $p_\Phi = p_\Phi(\rho_\Phi, e_\Phi)$, considering full thermodynamics including energy. The gas component g is modeled by the ideal-gas equation of state

$$p_g = (\gamma_g - 1)\rho_g e_g, \tag{2.31}$$

and the liquid l by the stiffened-gas equation of state

$$p_l = (\gamma_l - 1)\rho_l e_l - \gamma_l \pi_\infty, \tag{2.32}$$

where $\gamma_g = 1.4$, $\gamma_l = 2.35$, and $\pi_\infty = 10^9\,\mathrm{Pa}$ are model parameters (Le Métayer et al., 2005).

2.5. SUMMARY

In this chapter, the two employed multi-component modeling approaches were presented. Both are based on a single-fluid approach in which the governing equations are solved for a representative mixture fluid.

The first model is an equilibrium cavitation model extended by an additional gas component. The cavitating liquid is described by an isentropic relation and the thermodynamic closure is realized with a coupled, barotropic equation of state. A slightly modified coupled equation of state has been proposed for vapor bubbles containing gas.

The second model is a pressure-disequilibrium model governed by six transport equations, where for both components a full thermodynamic model is included. Phase transition and viscosity are neglected in this model.

3. NUMERICAL METHOD

In this chapter, we first introduce the mathematical model in Section 3.1. Then, we present the numerical flux calculation in CATUM (Section 3.2) and briefly discuss the implicit LES approach (Section 3.3). The time integration is described in Section 3.4. At the end of the chapter, we present the numerical method used in ECOGEN (Section 3.5).

3.1. FINITE VOLUME METHOD

For solving the governing equations (Eq. (2.3)), their weak or integral form is considered and Gauss' theorem applied

$$\partial_t \int_\Omega \boldsymbol{U}(\boldsymbol{x},t)\,dV + \int_{\partial\Omega} \boldsymbol{F}(\boldsymbol{U},\boldsymbol{x},t)\,dA = 0\,, \tag{3.1}$$

where Ω denotes the control volume with the surface $\partial\Omega$. Equation (3.1) is solved numerically by spatially discretizing the domain into N grid cells i with a control volume Ω_i with volume $V_i = \int_{\Omega_i} 1 dV$. The volume-averaged solution of a grid cell i can be expressed as

$$\bar{\boldsymbol{U}}_i(t) = \frac{1}{V_i}\int_{\Omega_i} \boldsymbol{U}_i(\boldsymbol{x},t)\,dV_i. \tag{3.2}$$

The surface integral in Eq. (3.1) is split into sub-integrals for each cell face j with area A_j and unit normal $\boldsymbol{n}_j$, and numerically approximated as

$$\int_{\partial\Omega_i} \boldsymbol{F}(\boldsymbol{U},\boldsymbol{x},t)\,dA = \sum_j (\check{\boldsymbol{F}}_j\,\boldsymbol{n}_j)A_j, \tag{3.3}$$

where $\check{\boldsymbol{F}}$ denotes the numerical approximation of the physical flux $\boldsymbol{F}$. Finally, a semi-discretized form of Eq. (3.1) is obtained

$$\partial_t\bar{\boldsymbol{U}}_i(t) \approx -\frac{1}{V_i}\sum_j (\check{\boldsymbol{F}}_j\,\boldsymbol{n}_j)A_j. \tag{3.4}$$

Equation (3.4) can be solved by finding a suitable reconstruction for $\check{\boldsymbol{F}}$ (see Section 3.2) and subsequent integration in time (see Section 3.4).

3.2. NUMERICAL FLUX FUNCTION

To obtain the numerical flux $\check{\boldsymbol{F}}$, composed of a convective $\check{\boldsymbol{C}}$, a pressure $\check{\boldsymbol{P}}$ and a viscous part $\check{\boldsymbol{D}}$, the values at the cell face must be reconstructed. In the following, an upwind-biased scheme

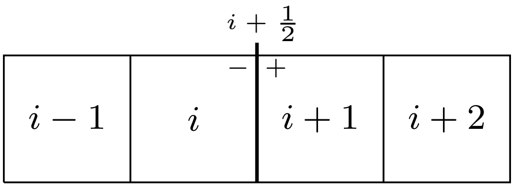

Figure 3.1.: Sketch of the four-cell stencil.

(Section 3.2.1) and a less-dissipative higher-order central scheme (Section 3.2.2) are presented for this reconstruction. The higher-order scheme can only be applied in smooth regions and, therefore, discontinuities as shock waves, steep gradients, and pseudo phase-boundaries have to be detected with a sensor functional enabling a switch to an upwind-biased reconstruction at these positions (Section 3.2.3). Further, the additional gas component ξ_g directly affects the thermodynamic calculations and thus requires special treatment, as is discussed in Section 3.2.4.

In CATUM a compact four-cell stencil is employed to reconstruct the cell face values, as sketched in Fig. 3.1. For simplicity, we consider an equidistant Cartesian grid and refer to Budich (2018) for the actual implementation. He describes the implemented scheme taking into account arbitrary orientations of the cell faces and varying distances of the grid points.

For a cell face $i+\frac{1}{2}$ the fluxes $\breve{\boldsymbol{C}}_{i+\frac{1}{2}}$, $\breve{\boldsymbol{P}}_{i+\frac{1}{2}}$ read

$$\breve{\boldsymbol{C}}_{i+\frac{1}{2}} = \breve{u}^*_{i+\frac{1}{2}} \breve{\boldsymbol{U}}_{i+\frac{1}{2}} = \breve{u}^*_{i+\frac{1}{2}} \begin{bmatrix} \breve{\rho} \\ \breve{\rho}\breve{\boldsymbol{u}} \\ \breve{\rho e} + \frac{1}{2}\breve{\rho}\breve{\boldsymbol{u}}^2 + \breve{p}^* \\ \breve{\rho}\breve{\xi}_g \end{bmatrix}_{i+\frac{1}{2}} \qquad \breve{P}_{i+\frac{1}{2}} = \breve{p}^*_{i+\frac{1}{2}} \begin{bmatrix} 0 \\ \boldsymbol{n} \\ 0 \\ 0 \end{bmatrix}, \tag{3.5}$$

where $\breve{u}^*$ is the numerical transport velocity and $\breve{p}^*$ the interface pressure. The reconstruction of $\breve{u}^*$, $\breve{p}^*$ and the primitive variables $\breve{\varphi} = \{\breve{\rho}, \breve{u}, \breve{v}, \breve{w}, \breve{\rho e}, \breve{\xi}_g\}$ is achieved by an upwind-biased scheme or a central one, as is described in the following.

3.2.1. UPWIND-BIASED SCHEME

Schmidt (2015) proposed this upwind-biased scheme, specially designed for compressible cavitating flows. For a more detailed description, we refer to his work, Sezal (2009) and Budich (2018).

For the upwind-biased reconstruction of the cell face values $\breve{\varphi}^u_{i+\frac{1}{2}}$, we first evaluate $\breve{\varphi}_{i+\frac{1}{2}}$ from the left side $\breve{\varphi}^-_{i+\frac{1}{2}}$ and the right side $\breve{\varphi}^+_{i+\frac{1}{2}}$ ($-,+$ in Fig. 3.1) and then take the upwind value corresponding to the sign of the transport velocity $\breve{u}^{*,u}$

$$\breve{\varphi}^u_{i+\frac{1}{2}} = \begin{cases} \breve{\varphi}^-_{i+\frac{1}{2}} & \text{for } \breve{u}^{*,u}_{i+\frac{1}{2}} \geq 0 \\ \breve{\varphi}^+_{i+\frac{1}{2}} & \text{for } \breve{u}^{*,u}_{i+\frac{1}{2}} < 0. \end{cases} \tag{3.6}$$

$\breve{\varphi}^\pm_{i+\frac{1}{2}}$ are the corresponding upwind cell value plus a higher-order contribution limited by a flux limiter *Lim*

$$\breve{\varphi}^-_{i+\frac{1}{2}} = \varphi_i + \frac{1}{2} Lim(r^-_{i+\frac{1}{2}})(\varphi_i - \varphi_{i-1}) \qquad \breve{\varphi}^+_{i+\frac{1}{2}} = \varphi_{i+1} + \frac{1}{2} Lim(r^+_{i+\frac{1}{2}})(\varphi_{i+2} - \varphi_{i+1}) \tag{3.7}$$

where the limiter function Lim is evaluated based on the ratio r

$$r^{-}_{i+\frac{1}{2}} = \frac{\varphi_i - \varphi_{i-1}}{\varphi_{i+1} - \varphi_i} \qquad r^{+}_{i+\frac{1}{2}} = \frac{\varphi_{i+1} - \varphi_i}{\varphi_{i+2} - \varphi_{i+1}} \tag{3.8}$$

of the corresponding upwind difference to the local difference. Note that for better readability we omit the ¯ indicating that the cell values (φ_i) are volume-averaged variables. For the velocity components $\varphi = \{u, v, w\}$ the slope limiter by Koren (1993)

$$Lim(r) = max\left[0, min\left(2r, \frac{1+2r}{3}, 2\right)\right] \tag{3.9}$$

is used, which is third-order accurate for sufficiently smooth data. For the density, the energy and the gas mass fraction $\varphi = \{\rho, \rho e, \xi_g\}$ the Minmod slope limiter (Roe, 1986)

$$Lim(r) = max(0, min(1, r)) \tag{3.10}$$

is employed, which is second-order accurate in smooth regions. Due to the high density gradients in cavitating flows, a more robust scheme has to be employed for ρ. The other thermodynamic quantities, ρe and ξ_g, are strongly coupled with ρ and for consistency and stability, they have to be reconstructed with the same limiter.

The numerical transport velocity $\breve{u}^{*,u}_{i+\frac{1}{2}}$ is calculated as

$$\breve{u}^{*,u}_{i+\frac{1}{2}} = \frac{I^{-}\breve{u}^{-}_{i+\frac{1}{2}} + I^{+}\breve{u}^{+}_{i+\frac{1}{2}} + p_i - p_{i+1}}{I^{-} + I^{+}} \tag{3.11}$$

with the acoustic impedances $I^{\pm}$

$$I^{-} = \frac{1}{4}(3\,\rho_i + 1\,\rho_{i+1})\,c_{max} \qquad I^{+} = \frac{1}{4}(1\,\rho_i + 3\,\rho_{i+1})\,c_{max}, \tag{3.12}$$

where c_{max} is the maximum speed of sound in the numerical stencil $(i-1, i, i+1, i+2)$.

For a low Mach number consistency, the interface pressure $\breve{p}^{*}_{i+\frac{1}{2}}$ is calculated with a second-order central approximation Schmidt (2015) as follows

$$\breve{p}^{*,u}_{i+\frac{1}{2}} = \frac{p_i + p_{i+1}}{2}. \tag{3.13}$$

The diffusive flux $\breve{\boldsymbol{D}}_{i+\frac{1}{2}}$ is discretized by a linear second-order central scheme.

3.2.2. HIGHER-ORDER CENTRAL RECONSTRUCTION

Egerer et al. (2016) designed a higher-order, central scheme for the available compact four-cell stencil. This central scheme can be only applied in smooth regions and therefore a sensor functional $f(\vartheta)$ is employed to detect discontinuities. The reconstruction of $\breve{\varphi}_{i+\frac{1}{2}}$ reads as

$$\breve{\varphi}_{i+\frac{1}{2}} = (1 - f(\vartheta))\,\breve{\varphi}^{c}_{i+\frac{1}{2}} + f(\vartheta)\,\breve{\varphi}^{u}_{i+\frac{1}{2}}. \tag{3.14}$$

where the superscript c denotes the central scheme and u the upwind-biased one described above. The sensor functional $f(\vartheta) \in [0;1]$ switches between these two schemes depending on the flow field and is presented in Section 3.2.3.

The central reconstruction is as follows: The velocities and static pressure $\varphi = \{u, v, w, p\}$ are reconstructed by a linear fourth-order central scheme

$$\breve{\varphi}^{c}_{i+\frac{1}{2}} = \frac{1}{12}(7(\varphi_i + \varphi_{i+1}) - \varphi_{i-1} - \varphi_{i+2}), \tag{3.15}$$

while the thermodynamic variables $\varphi = \{\rho, \rho e, \xi_g\}$ are approximated with the mean of the reconstructed values from the left and the right side

$$\breve{\varphi}^{c}_{i+\frac{1}{2}} = \frac{1}{2}(\breve{\varphi}^{+}_{i+\frac{1}{2}} + \breve{\varphi}^{-}_{i+\frac{1}{2}}). \tag{3.16}$$

Furthermore, the calculation of the interface pressure $\breve{p}^{*}_{i+\frac{1}{2}}$ and the numerical transport velocity $\breve{u}^{*}_{i+\frac{1}{2}}$ are also with a higher-order reconstruction in smooth regions with

$$\breve{p}^{*}_{i+\frac{1}{2}} = (1 - f(\vartheta))\, \breve{p}^{c}_{i+\frac{1}{2}} + f(\vartheta) \left(\frac{\breve{p}^{-}_{1+\frac{1}{2}} + \breve{p}^{+}_{1+\frac{1}{2}}}{2} \right) \tag{3.17}$$

and

$$\breve{u}^{*}_{i+\frac{1}{2}} = (1 - f(\vartheta))\, \breve{u}^{*\,c}_{i+\frac{1}{2}} + f(\vartheta)\, \breve{u}^{*\,u\prime}_{i+\frac{1}{2}}, \tag{3.18}$$

where $\breve{u}^{*\,c}_{i+\frac{1}{2}}$ is

$$\breve{u}^{*\,c}_{i+\frac{1}{2}} = \breve{u}^{c}_{i+\frac{1}{2}} + \frac{\Delta^{\breve{3}} p_{i+\frac{1}{2}}}{I^{-} + I^{+}} \tag{3.19}$$

and $\breve{u}^{*\,u\prime}_{i+\frac{1}{2}}$ a slight modification of Eq. (3.11) as

$$\breve{u}^{*\,u\prime}_{i+\frac{1}{2}} = \frac{I^{-}\breve{u}^{-}_{i+\frac{1}{2}} + I^{+}\breve{u}^{+}_{i+\frac{1}{2}} + \breve{p}^{-}_{1+\frac{1}{2}} - \breve{p}^{+}_{1+\frac{1}{2}}}{I^{-} + I^{+}}. \tag{3.20}$$

The acoustic impedances $I^{\pm}$ are calculated as in Eq. (3.12).

This higher-order scheme is less dissipative and thus suitable for LES of turbulent flows. Adding a regularization term makes this numerical approximation capable of sub-grid-scale modeling, as presented in Section 3.3

3.2.3. SENSOR FUNCTIONAL

The smoothness of the flow field is characterized by a sensor functional $f(\vartheta)$, which controls the reconstruction at the cell face. Shock and expansion waves are detected by the vorticity-dilation sensor proposed by Ducros et al. (1999)

$$\vartheta^{D} = \frac{(\nabla \cdot \boldsymbol{u})^2}{(\nabla \cdot \boldsymbol{u})^2 + (\nabla \times \boldsymbol{u})^2 + \epsilon}, \tag{3.21}$$

where ϵ denotes a very small value to avoid division by zero.

Pseudo phase-boundaries are detected with the variation of the vapor volume fraction $\gamma = \alpha$ in all three spatial directions here indicated with i, j, k

$$\vartheta^{\gamma} = var_i(\gamma) + var_j(\gamma) + var_k(\gamma) \ , \tag{3.22}$$

where the variation is evaluated as

$$var_i(\gamma) = \|\gamma_i - \gamma_{i-1}\| + \|\gamma_{i+1} - \gamma_i\|. \tag{3.23}$$

For simulations of multi-component flows, the sensor functional is extended by adding the 3-D variation in gas volume fraction, $\gamma = \{\alpha, \beta_g\}$. If at least one sensor component exceeds its threshold value, the scheme switches to the upwind-biased reconstructions as

$$f(\vartheta^D, \vartheta^\alpha, \vartheta^{\beta_g}) = \begin{cases} 1, & if \quad \vartheta^D > \vartheta^D_{th} \parallel \vartheta^\alpha > \vartheta^\alpha_{th} \parallel \vartheta^{\beta_g} > \vartheta^{\beta_g}_{th} \\ 0, & else. \end{cases} \tag{3.24}$$

Egerer et al. (2016) proposed the threshold values $\vartheta^D_{th} = 0.95$ and $\vartheta^\alpha_{th} = 0.25$ and Rahn (2017) found $\vartheta^{\beta_g}_{th} = 0.4$.

3.2.4. EXTENSION FOR GAS MODELING

In this thesis, the numerical modeling approach has been extended for an additional gas component ξ_g. Since ξ_g directly affects ρ and p by the thermodynamic model, the reconstruction of ξ_g is crucial for stability and accuracy. High pressure oscillations can arise in case of an inconsistent reconstruction. One way to avoid stability issues is to reconstruct ξ_g in the same way as ρ and to use for both quantities a robust scheme as e.g. a Van-Albada or Minmod limiter function, see Trummler (2014). Further stability and accuracy can be gained by a thermodynamically coupled reconstruction of ξ_g as proposed in Trummler et al. (2018c). ξ_g is calculated with the employed equation of state (EOS) based on the reconstructed pressure and density at the cell face as

$$\breve{\xi}_{g,i+\frac{1}{2}} = EOS(\breve{\rho}_{i+\frac{1}{2}}, \breve{p}_{i+\frac{1}{2}}). \tag{3.25}$$

A series of specifically designed test-cases demonstrated that the proposed modifications are sufficient to avoid pressure oscillations while keeping contact waves crisp without artificial smearing, see Rahn (2017).

3.3. TURBULENCE MODELING

In Large-eddy simulations (LES) the smallest scales are not resolved on the computational grid and thus the effects of these unresolved sub-grid scales must be modeled accordingly. This can be either achieved by explicitly modeling the sub-grid scale stresses, such as in e.g. the Dynamic Smagorinsky Model (Germano et al., 1991), or implicitly by using the numerical truncation error as a physically consistent sub-grid scale model for turbulence.

We employ an implicit LES approach based on the Adaptive Local Deconvolution Method (ALDM) (Adams et al., 2004; Hickel et al., 2006). In ALDM, free parameters are included to control the implicit sub-grid scale model and to obtain a model consistent with turbulence theory. Hickel et al. (2014) have extended the originally incompressible method for compressible flows and cavitating ones (Hickel et al., 2011). Recently, Egerer et al. (2016) adapted the structure of the compressible ALDM-scheme to be applicable to the available framework with the higher-order central reconstruction. For the ILES flux function, a regularization term $\breve{\boldsymbol{R}}$ is added to the convective fluxes as

$$\breve{\boldsymbol{C}}^{ILES} = \breve{\boldsymbol{C}} - \breve{\boldsymbol{R}} = \breve{u}^* \begin{bmatrix} \breve{\rho} \\ \breve{\rho}\breve{\boldsymbol{u}} \\ \breve{\rho}e + \frac{1}{2}\breve{\rho}\breve{\boldsymbol{u}}^2 + \breve{p}^* \\ \breve{\rho}\breve{\xi}_g \end{bmatrix} - \begin{bmatrix} \breve{R}^{\rho} \\ \breve{\boldsymbol{R}}^{\rho u} \\ \breve{R}^{\rho e} \\ 0 \end{bmatrix} \tag{3.26}$$

The regularization term is a function of the values reconstructed with the higher-order central scheme $\breve{\varphi}^c$ and free parameters ω^{φ} as $\breve{\boldsymbol{R}} = \breve{\boldsymbol{R}}(\breve{\varphi}^c, \omega^{\varphi})$. Note that no regularization is applied to the gas mass fraction. The free parameters ω^{φ} are calibrated in such a way that a physically consistent sub-grid scale model is obtained. For the calibration and a detailed description of the scheme, we refer to Egerer et al. (2016).

3.4. TIME INTEGRATION

To march the volume-averaged solution forward in time, we use an explicit second-order, four-step low-storage Runge-Kutta method (Schmidt, 2015). Considering a simplified version of Eq. (3.4)

$$\partial t\, \bar{\boldsymbol{U}}_i(t) = \mathcal{L}_i(\bar{\boldsymbol{U}}_i), \tag{3.27}$$

with $\mathcal{L}$ representing the right-hand side of Eq. (3.4), a multi-step time integration from $t = n$ to $t = n + 1$ reads

$$\bar{\boldsymbol{U}}_i^{n+1,k} = \bar{\boldsymbol{U}}_i^{n} + C_k\, \Delta t\, \mathcal{L}_i(\bar{\boldsymbol{U}}_i^{n+1,k-1}) \tag{3.28}$$

with $k = 1, .., N_k$,

$$\bar{\boldsymbol{U}}_i^{n+1,0} = \bar{\boldsymbol{U}}_i^{n} \quad \text{and} \quad \bar{\boldsymbol{U}}_i^{n+1} = \bar{\boldsymbol{U}}_i^{n+1,N_k}. \tag{3.29}$$

For the employed four-step method ($N_k = 4$), the coefficients are $C_1 = 0.11$, $C_2 = 0.2766$, $C_3 = 0.5$, $C_4 = 1$, see Schmidt (2015).

The global time step Δt in our simulations is determined by the minimum of the local time steps

$$\Delta t = min(\Delta t_i), \tag{3.30}$$

which are evaluated by the Courant-Friedrichs-Lewy (CFL) criterion as

$$\Delta t_i = CFL \left(\frac{\Delta x_i}{|u_i| + c_i} + \frac{{\Delta x_i}^2}{2(\nu_i + \nu_{t,i})} \right). \tag{3.31}$$

The length scale Δx_i is calculated with a characteristic cell length l_i divided by the dimension N_d as $\Delta x_i = l_i / N_d$. u_i is a characteristic velocity, c_i the speed of sound, ν_i the kinematic viscosity of the fluid and $\nu_{t,i}$ the unresolved viscosity of the sub-grid-scale. The first term in Eq. (3.31) represents the limit due to convection and the second due to diffusion, see Ferziger et al. (2002). For the simulations presented in Chapters 5, 6 and 8 to 10, $CFL = 1.4$ is used.

3.5. NUMERICAL METHOD IN ECOGEN

In ECOGEN the pressure-disequilibrium model by Saurel et al. (2009) is employed, which can be expressed as

$$\partial_t \boldsymbol{U} + \nabla \cdot \boldsymbol{F}(\boldsymbol{U}) + \boldsymbol{h}(\boldsymbol{U}) \nabla \cdot \boldsymbol{u} = \boldsymbol{r}(\boldsymbol{U}) \,, \tag{3.32}$$

with the state vector $\boldsymbol{U}$, the fluxes $\boldsymbol{F}$, here composed of convective terms and pressure terms, and the non-conservative terms $\boldsymbol{h}$ and $\boldsymbol{r}$, where $\boldsymbol{h}$ contains additional pressure terms and $\boldsymbol{r}$ is for the pressure relaxation. Equation (3.32) is solved numerically by the finite-volume method for the cell i at time $n+1$

$$\bar{\boldsymbol{U}}_i^{n+1} = \bar{\boldsymbol{U}}_i^{n} - \frac{\Delta t}{V_i} \left(\sum_j (\check{\boldsymbol{F}}_j \, \boldsymbol{n}_j) A_j + \boldsymbol{h}(\bar{\boldsymbol{U}}_i^{n}) \sum_j (\check{\boldsymbol{u}}_j \, \boldsymbol{n}_j A_j) \right) . \tag{3.33}$$

As above, j denotes the cell faces with area A_j and unit normal vector $\boldsymbol{n}_j$ and $\check{\boldsymbol{F}}$ the numerical approximation of the physical flux $\boldsymbol{F}$.

FLUX FUNCTION

At the cell faces, the associated Riemann problem is computed using the HLLC approximate solver (Toro, 1997) to obtain $\check{\boldsymbol{F}}$ and $\check{\boldsymbol{u}}$, respectively. The primitive variables are reconstructed using the monotonized central slope limiter (Van Leer, 1977). Written in the notation in Section 3.2.1 the limiter function reads as

$$Lim(r) = max \left[0, min\left(2r, 0.5(1+r), 2\right)\right] , \tag{3.34}$$

and is second-order total-variation-diminishing in smooth regions. Additionally, the interface-sharpening technique Tangent of Hyperbola for Interface Capturing (THINC) (Shyue and Xiao, 2014) is used to minimize interface diffusion.

TIME INTEGRATION

For the time integration, an explicit two-step method is employed (Schmidmayer et al., 2019b). In the notation in Section 3.4, the integrator uses $N_k = 2$, $C_1 = 0.5$, and $C_2 = 1$. Using this time integration, the CFL-number is set to $CFL = 0.4$ for the simulations presented in Chapter 7.

3.6. SUMMARY

To solve the governing equations, the finite volume method is employed and the flow domain is discretized into finite volumes. The fluxes across the cell faces are approximated by the reconstructed primitive variables. For the reconstruction, an upwind-biased baseline scheme and a higher-order central scheme with a switch at discontinuities are implemented in CATUM. The extension of the central scheme with an adequate regularization term provides an implicit LES model where the numerical truncation error represents a sub-grid scale model for turbulence. For the time integration, CATUM employs an explicit second-order, four-step Runge-Kutta method.

The flow solver ECOGEN uses a second-order central flux reconstruction and an explicit two-step time integrator.

4. CODE IMPLEMENTATIONS

In the context of this work, the two CFD codes CATUM and ECOGEN are used. The methods presented in the previous chapters are employed in these codes. In the following, their development, field of application and implementation are briefly described.

4.1. FLOW SOLVER CATUM

CATUM is a fully compressible flow solver specially designed for the simulation of cavitating flows and has been entirely developed in the gas dynamics group at the Chair of Aerodynamics and Fluid Mechanics at TU Munich. The in-house flow solver was used for the simulations presented in Chapters 5, 6 and 8 to 10. The thermodynamic models described in Section 2.3 and the numerical method presented in Sections 3.2 to 3.4 are implemented in the code.

Originally designed for inertia driven cavitating flows (Schmidt, 2015), viscous effects were neglected and the code was successfully employed for studies of cavitation dynamics (Schnerr et al., 2008; Schmidt et al., 2009; Budich et al., 2018; Gorkh et al., 2018), bubble cloud collapses (Schmidt et al., 2014; Ogloblina et al., 2018) and numerical cavitation erosion prediction (Mihatsch et al., 2015; Beban et al., 2017). Code extensions to include viscous effects and a higher-order central numerical scheme with an ILES flux function (Egerer et al., 2016) resolve even more flow physics and thus increased the capabilities. Currently, CATUM is not only used for cavitating flows but also to investigate e.g. transcritical turbulent channel flows (Döhring et al., 2018, 2019). The current version features a wide range of thermodynamic modeling approaches including analytical models for full thermodynamics, multi-dimensional tabulated equations of state with a fast searching algorithm and real gas modeling. On-going research projects focus on wall modeling and the implementation of non-Newtonian viscosity models.

Contrary to most academic codes using Cartesian grids, CATUM operates on structured, body-fitted grids, which makes it particularly suitable for application to complex geometries such as ship propellers (Budich et al., 2015) or injector components. However, the consideration of different cell sizes and cell face orientations requires an elaborate and complex implementation, see Budich (2018). CATUM is written in Fortran and parallelized using Massage Passing Interface. Since our high-resolution, fully compressible simulations require a lot of computing power, the code is optimized for massively parallel calculations on high-performance supercomputers like the Super MUCs of the LRZ in Garching. The original version of CATUM used a 1-to-1 mapping of grid blocks to processors. Such an approach is not feasible for complex geometries and thus Budich (2018) extended the code to allow arbitrary distribution of the blocks on the processors used. Furthermore, Budich (2018) restructured and partially rewrote the code, documented it, redesigned the workflow and integrated state-of-the-art tools and standards, greatly facilitating and accelerating the utilization and application of the in-house flow solver. Additionally, he also implemented an Arbitrary-Lagrangian-Eulerian approach to study moving geometries (Budich et al., 2016; Budich, 2018).

As part of this Ph.D. project, I have significantly contributed to the continuous development of the code. My contribution has primarily been to multi-component modeling with an additional gas component. I built the infrastructure to account for additional scalars and gas components and then implemented several thermodynamic models for multi-component flows. Furthermore, I have worked on the general code development and the surrounding infrastructure. For example, I have designed several modules for predicting cavitation erosion and have written scripts for pre- and post-processing.

4.2. FLOW SOLVER ECOGEN

ECOGEN (Schmidmayer et al., 2019a,b) is an open-source CFD platform for numerical simulation of compressible multiphase flows, see *https://code-mphi.github.io/ECOGEN/*. It has been verified for several gas bubble dynamics applications, including free-space (Schmidmayer et al., 2020) and wall-attached (Pishchalnikov et al., 2019) bubble collapses. The methods described in Section 2.4 and Section 3.5 are implemented in the code and used for the results presented in Chapter 7.

Within the scope of this project, Kevin Schmidmayer and I have implemented the feature allowing for steps and slopes in walls, and a routine to evaluate maximum pressures. Further, I wrote several scripts to enhance and facilitate the workflow, enabling concurrent result analysis and automated post-processing. Simulations were conducted on the cluster *Richardson* at Caltech.

Part II.

CAVITATION BUBBLES AND THEIR DYNAMICS

5. VAPOR BUBBLE CONTAINING GAS

We investigate numerically the effect of non-condensable gas inside a vapor bubble on the bubble dynamics and the collapse pressure. Free gas inside vapor bubbles has a cushioning effect that can weaken the pressure wave and enhance the bubble rebound. For the cavitating liquid and the non-condensable gas, we employ the coupled equation of state described in Section 2.3.2.

Parts of the results presented here overlap with the peer-reviewed conference contribution Trummler et al. (2018a).

5.1. MOTIVATION AND THEORY

In technical applications and experiments, it can be assumed that a certain amount of non-condensable gas is present in vapor cavities. In general, gases are dissolved in liquids (Pollack, 1991) and are released during pressure reduction by outgassing (Iben et al., 2015; Freudigmann et al., 2017) or cavitation. In experiments with cavitation bubbles, gases are produced when the bubbles are generated using lasers or sparks due to chemical reactions and recombination processes (Sato et al., 2013; Akhatov et al., 2001).

Gas inside a vapor bubble has a damping effect that can weaken the pressure wave and increase the rebound of the bubble. For spherical bubble collapses, the damping effect is evident in the incompressible Rayleigh-Plesset equation (Plesset, 1949)

$$\rho_l(\ddot{R}R + 3/2\,\dot{R}^2) = -\Delta p + p_g, \tag{5.1}$$

here written in inviscid form neglecting surface tension, with the driving pressure difference $\Delta p = p_\infty - p_{sat}$ and the gas pressure $p_g = p_{g,0}\left(R_0/R\right)^{3\gamma}$. $p_{g,0}$ and γ denote the initial gas content and the adiabatic index, respectively. The compressible equation of Keller and Miksis (1980) captures the collapse and the rebound. Taking advantage of the fact that it can be treated according to the first order (Prosperetti, 1987), and again neglecting viscosity and surface tension, it simplifies to

$$\rho_l(\ddot{R}R(1-v) + 3/2\dot{R}^2(1-v/3)) = (-\Delta p + p_g)(1+v) + R\dot{p_g}/c_l, \tag{5.2}$$

with $v = \dot{R}/c_l$. Both equations clearly show that the gas inside the bubble decelerates the collapse and that this effect is more pronounced at lower driving pressure differences. With a compressible formulation the rebound is captured, which increases with the gas content.

Fujikawa and Akamatsu (1980) and Akhatov et al. (2001) analytically investigated bubble dynamics including compressibility, phase transition with non-equilibrium effects and conductive heat transfer. Akhatov et al. (2001) additionally considered supercritical conditions at collapse.

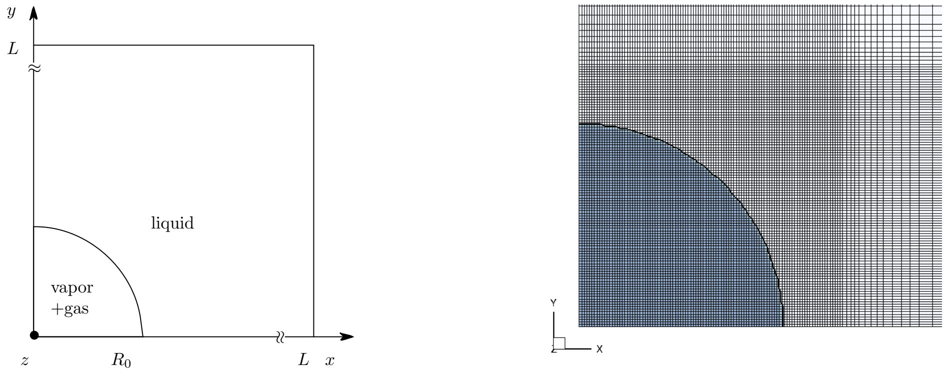

(a) (b)

Figure 5.1.: Simulation set-up. (a) Sketch of the numerical set-up, (b) Grid in near bubble region and initialized bubble.

Tinguely et al. (2012) systematically investigated the energy partitioning into shockwave energy and rebound energy for spherical bubble collapses under microgravity. Furthermore, they derived an analytical model from the Keller-Miksis Equation demonstrating that the energy partitioning depends on one single parameter.

The aim of the presented work is to numerically investigate and reproduce the findings of Tinguely et al. (2012) and to thereby validate our gas modeling approach, presented in Section 2.3.2.

5.2. SET-UP

A bubble with an initial radius R_0 of 400 µm is placed in the center of a box with dimension $500 \times R_0$ in each direction. Taking advantage of symmetry, only an eighth of a bubble is simulated. The domain is discretized with an equidistant grid within a cubic sub-domain with an edge length of 1.25 R_0, and for the outer part a grid stretching is applied. Simulations are performed on different grid levels defined by the number of cells over the initial radius N_C/R_0. If not stated otherwise, the results are for a grid-resolution of $N_C/R_0 = 80$. The pressure field is initialized with a pressure jump at the pseudo phase boundary.

For this investigation, the initial gas content in the bubble $p_{g,0}$ and the driving pressure difference Δp are varied covering different combinations of $\Delta p = 1e4 - 1e5\,\text{Pa}$ and $p_{g,0} = 0 - 1000\,\text{Pa}$. During the simulations, pressure signals are recorded at certain radial positions from the bubble center.

5.3. RESULTS

Figure 5.2 (a) depicts the bubble collapse and the rebound at different time steps for $\Delta p = 10\text{kPa}$ with $p_{g,0} = \{0\ \text{Pa}, 1000\ \text{Pa}\}$. The left time series presents the bubble collapse without gas, showing the initial bubble, the situation shortly before the collapse and the emitted shockwave

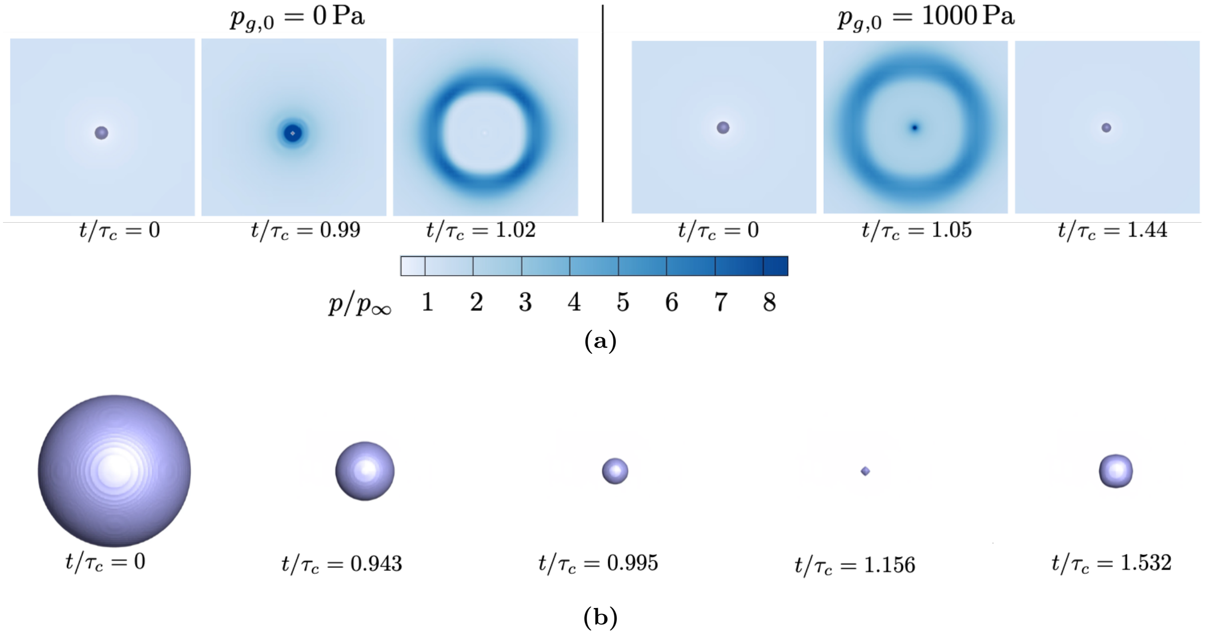

Figure 5.2.: Time series of bubble collapse and rebound. (a) Pressure field for $\Delta p = 10\,\mathrm{kPa}$ with $p_{g,0} = 0\,\mathrm{Pa}$ (left) and with $p_{g,0} = 1000\,\mathrm{Pa}$ (right), (b) Near bubble region to visualize the rebound for $\Delta p = 10\,\mathrm{kPa}$ with $p_{g,0} = 1000\,\mathrm{Pa}$.

after collapse. Analogously, the dynamics of a bubble with a high gas content is visualized in the right time series. In this case, a rebound is visible at $t = 1.44\,\tau_c$. In Fig. 5.2 (b) the near bubble region is shown to visualize the rebound behavior.

Figure 5.3 (a) compares the temporal evolution of the normalized bubble radius R/R_0 for different gas contents. The time is normalized to the Rayleigh collapse time $\tau_c = 0.915 \cdot R_0\sqrt{\rho_l/\Delta p}$ (Rayleigh, 1917). Without gas, there is a very small rebound after the shockwave has propagated outwards. In configurations with gas, the bubbles rebound significantly. Besides the rebound, the non-condensable gas in the vapor bubble also affects the intensity of the emitted pressure wave. Figure 5.3 (b) shows the monitored pressure at certain radial positions from the bubble center and different gas contents. We have normalized the pressure with $p^* = c_l\sqrt{\rho_l \Delta p}$. The radial decay of the maximum pressure is obvious and the presence of gas reduces the maximum pressure. The damping effect of the gas is more distinct for probes closer to the bubble center. Additionally, the pressure signals reveal that the collapse time is closely matched. Figure 5.3 (c) compares the pressure maximum in the near bubble region. Again, the damping effect of the gas and the decay of the damping effect with increasing distance to the focus point are evident.

The grid resolution is known to affect the minimum bubble radius and the rebound (Beig et al., 2018; Schmidmayer et al., 2020) and the intensity of the pressure peaks (Mihatsch et al., 2015; Schmidt et al., 2014). To assess the grid influence, we have conducted a grid study. Figure 5.4 (a) depicts the temporal evolution of the bubble radius for different grid resolutions. As expected, the rebound increases with increasing grid resolution and approaches the one predicted by the

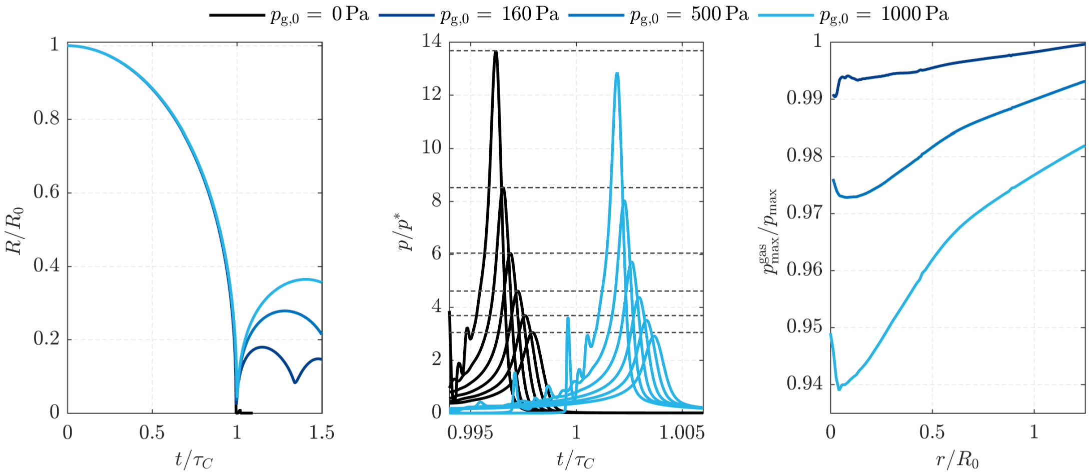

(*a*) (*b*) (*c*)

Figure 5.3.: Simulation results. (a) Temporal evolution of the bubble radius, (b) Pressure signals from the probes 0.1 : 0.05 : 0.35 R_0 for selected conditions, (c) Maximum pressure compared to that without gas. (Grid resolution 80 N_C/R_0).

Keller-Miksis equation. Figure 5.4 (b) compares the maximum pressure of the configuration with gas (p_{max}^{gas}) to that without gas (p_{max}). At all grid resolutions, the gas has a damping effect on the maximum pressure, although a higher grid resolution results in higher damping since the focus point is better resolved and the transport of the emitted shockwave is less dissipative. Based on our observations, we consider a grid resolution of 80 N_C/R_0 as a good compromise of accuracy and necessary computational resources.

5.3.1. ENERGY PARTITIONING MODEL

Tinguely et al. (2012) experimentally and theoretically investigated the effects of the driving pressure difference Δp and initial gas content $p_{g,0}$ on bubble dynamics and shockwave emission. They postulated that the initial energy of a bubble E_0 mainly partitions into rebound energy E_{reb} and shockwave energy E_{sw}

$$E_0 \to E_{reb} + E_{sw}, \tag{5.3}$$

which is in terms of normalized energies $\epsilon_{reb} = E_{reb}/E_0$, $\epsilon_{sw} = E_{sw}/E_0$

$$\epsilon_{reb} + \epsilon_{sw} = 1. \tag{5.4}$$

The initial energy and the rebound energy are potential energies at the corresponding instants (Obreschkow et al., 2006)

$$E_0 = \frac{4\pi}{3} R_0^3 \Delta p \quad \text{and} \quad E_{reb} = \frac{4\pi}{3} R_{reb}^3 \Delta p, \tag{5.5}$$

and thus the normalized energy partitioning into the rebound ϵ_{reb} is

$$\epsilon_{reb} = E_{reb}/E_0 = \left(R_{reb}/R_0\right)^3. \tag{5.6}$$

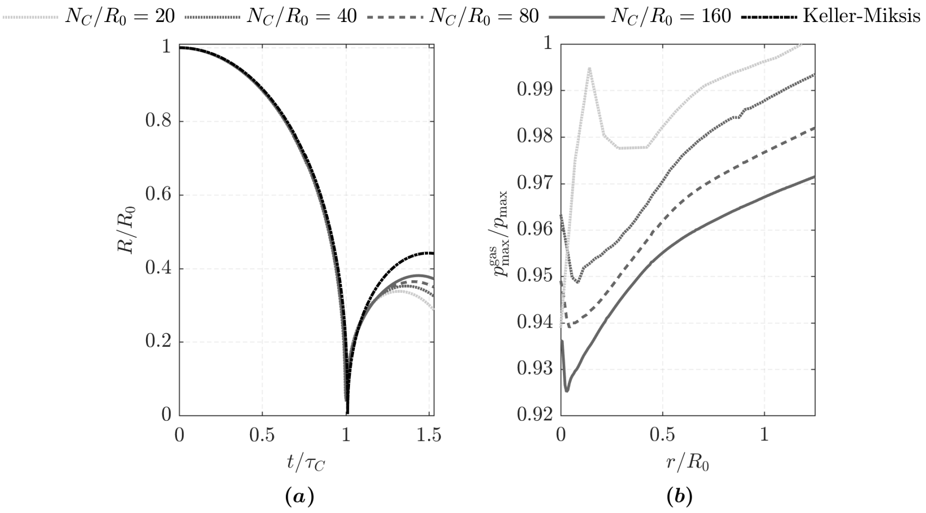

Figure 5.4.: Grid effect on the rebound and the damping of the maximum pressure by the gas for $\Delta p = 1e5\,\mathrm{Pa}$ and $p_g = 1000\,\mathrm{Pa}$. (a) Temporal evolution of the bubble radius, (b) Maximum pressure compared to that without gas.

The shockwave energy E_{sw} at a distance d from the focus point reads (Vogel and Busch, 1996)

$$E_{sw} = \frac{4\pi d^2}{\rho_l c_l} \int p(t)^2 dt. \tag{5.7}$$

Based on the assumption that the pressure signals $p(t)$ have a universal shape that scales with the peak value p_{max}, one can estimate $E_{sw} \propto p_{max}^2$. The normalized energy partitioning into the shockwave ϵ_{sw} can be approximated with

$$\epsilon_{sw} \approx 1 - \epsilon_{reb}, \tag{5.8}$$

or be assessed by the relative damping of the peak values as

$$\epsilon_{sw} \approx \left(p_{max}/p_{max,no\,rebound}\right)^2, \tag{5.9}$$

or be calculated by integration of the pressure signals.

Tinguely et al. (2012) derived a theoretical model using the inviscid Keller-Miksis equation (Eq. (5.2)) to predict the energy partitioning. Based on this model and experimental measurements, they could show that the energy partitioning into rebound ϵ_{reb} and shock wave energy ϵ_{sw} depends on a single parameter

$$\psi = \frac{\Delta p \gamma^6}{{p_{g,0}}^{1/\gamma}(\rho_l c_l^2)^{1-1/\gamma}}. \tag{5.10}$$

Figure 5.5 plots the energy partitioning over ψ. The shockwave energy increases with ψ and thus with the driving pressure difference and decreases with the partial pressure of free gas. On the other hand, the rebound is enhanced for a lower driving pressure difference and a higher gas content.

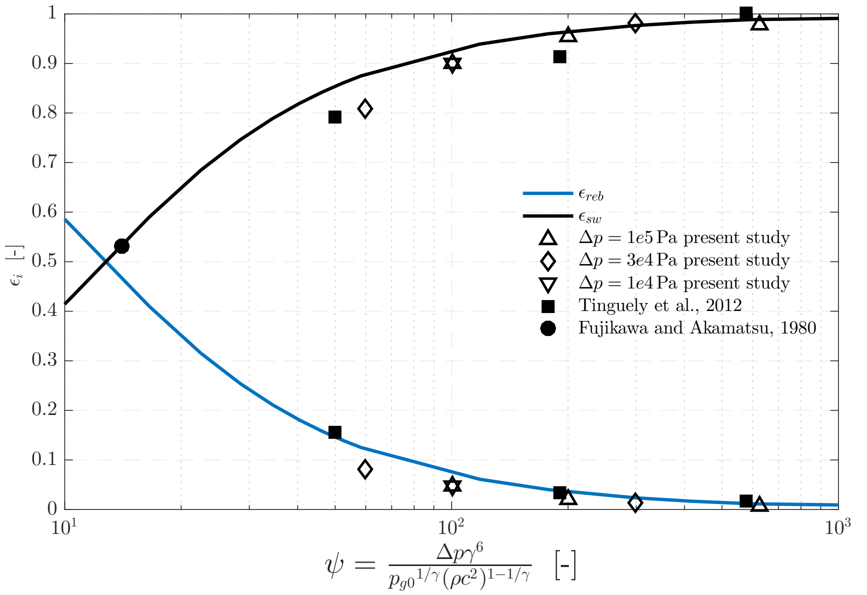

Figure 5.5.: Simulation results in comparison with the theoretical energy partitioning proposed by Tinguely et al. (2012) and experimental data.

For the comparison of our simulation results with the energy partitioning model, the normalized rebound energy ϵ_{reb} is obtained from the maximum radius of the bubble in the first rebound using Eq. (5.6). For the normalized shockwave energy ϵ_{sw}, the pressure signals recorded at the bubble center are numerically integrated and set in relation to the respective values without gas and thus no rebound. Additionally, we have also evaluated the square of the ratios of the collapse pressures, see Eq. (5.9), which yield, as expected, to comparable results. The evaluated energy partitioning in our simulations is included in Fig. 5.5 and are in good agreement with the model and values from the literature. Further, we can confirm a ψ-equivalence, i.e. same ψ-values result in a comparable rebound behavior and reduction of the shockwave energy.

5.4. SUMMARY

In this chapter, we have applied a modified multi-component model to simulate vapor bubbles containing free, non-condensable gas. With our simulations, we could reproduce the physical effects of gas inside a vapor bubble. Free gas in a vapor bubble leads to a stronger rebound and dampens the emitted shockwave. This effect is already visible on coarse grid resolutions but gets more pronounced for higher grid resolutions. Additionally, we were able to reproduce the partitioning into rebound and shockwave energy proposed by Tinguely et al. (2012) and could confirm a ψ-equivalence. This validation allows us to investigate the effect of free gas inside vapor structures on more complex configurations such as the collapse of wall-attached bubbles.

6. ASPHERICAL BUBBLE COLLAPSE AT ATMOSPHERIC PRESSURE

In this chapter, we present simulation results of wall-attached bubbles collapsing at atmospheric pressure. We analyze the collapse dynamics and the distribution of the induced maximum pressure. Based on the results, we propose schematics for the collapse and rebound dynamics. Additionally, we investigate the effect of an additional certain amount of non-condensable gas inside vapor bubbles.

Parts of the results presented here overlap with the peer-reviewed conference contribution Trummler et al. (2019).

6.1. MOTIVATION

The driving pressure difference governs the intensity of the emitted pressure wave, the rebound and the influence of the gas, as discussed in the previous chapter and covered in e.g. Brennen (1995); Franc and Michel (2005); Tinguely et al. (2012). Consequently, a stronger rebound and a more pronounced damping effect of the gas occurs under atmospheric conditions than with, for example, 100 bar. Despite the lower intensity of the pressure waves, cavitation erosion still plays an important role under atmospheric conditions, as e.g. in marine applications. But one of the most important examples are experiments of single bubbles. These are nearly always performed under atmospheric conditions and are still the main tool for studying cavitation and cavitation erosion (Philipp and Lauterborn, 1998; Dular et al., 2019).

CFD simulations, on the other hand, are mainly carried out at high driving pressure differences. One reason for this is the lower computational effort. The collapse time scales with $\tau_C \propto 1/\sqrt{\Delta p}$ and because the time step of compressible simulations is mainly determined by the speed of sound, the simulation time also roughly scales with τ_C. Moreover, the increased rebound at low driving pressures extends the simulation time even further. Apart from the computational costs, many models are not able to capture the relevant processes. Only a few models take into account compressibility and phase transition and are also able to capture the rebound correctly. Barotropic, homogeneous mixture models including phase change are well suited for this application.

We want to reduce this gap between experiment and simulation and present numerical investigations at atmospheric conditions. The stand-off distance has a significant influence on collapse dynamics and wall pressure (Tomita and Shima, 1986; Philipp and Lauterborn, 1998; Lauer et al., 2012b), where the wall pressure and consequently the cavitation erosion potential is highest at small stand-off distances. Therefore, we consider wall-attached bubbles at two different

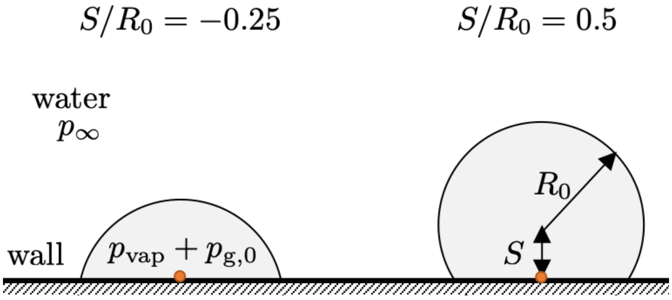

Figure 6.1.: Sketch of the investigated configurations $S/R_0 = -0.25$ and $S/R_0 = 0.5$. The orange circle marks the position of the pressure signals monitored.

stand-off distances.

Additionally, we have also performed simulations of vapor bubbles containing a certain amount of non-condensable gas. Based on experimental data, Tinguely et al. (2012) estimated the initial partial gas content of non-condensable gas inside of laser-generated bubbles in water to be $7 \pm 3.5\,\text{Pa}$. Moreover, they also found that the energy partitioning into shock wave energy and rebound energy is dictated by the non-dimensional parameter $\psi = (\Delta p \gamma^6) \,/\, \left({p_{\text{g},0}}^{1/\gamma} (\rho_l c_l^2)^{1-1/\gamma}\right)$. For the lower limit of the estimated gas content of $p_{g,0} = 3.5\,\text{Pa}$, an adiabatic index of $\gamma = 1.4$, a driving pressure of 1 bar and water, this value is $\psi = 630$. Since we model the additional gas isothermal, we consider the ψ equivalent gas content for $\gamma = 1$ of $p_{g,0} = 160\,\text{Pa}$. The ψ-equivalence of our simulation results regarding rebound and damping of the maximum pressure has been demonstrated in Chapter 5.

6.2. SET-UP

A vapor bubble with an initial radius R_0 of 400 µm is placed with different stand-off distances to the wall, as depicted in Fig. 6.1. We initialize the pressure field with a jump at the bubble interface with a driving pressure difference of $\Delta p = 1\,\text{e}5\,\text{Pa}$. We consider either pure vapor bubbles ($p_{\text{g},0} = 0\,\text{Pa}$) or vapor bubbles containing a non-condensable gas content of $p_{\text{g},0} = 160\,\text{Pa}$.

Taking advantage of symmetry, only a quarter of the bubble is simulated. The bubble is placed in the center of a rectangular domain with an extension of $125 \times R_0$ in wall-normal direction and $250 \times R_0$ in wall-parallel directions. The domain is discretized with an equidistant grid within the near bubble region (80 cells/R_0) and for the outer part a grid stretching is applied. In the previous chapter, a grid study is included demonstrating that this resolution is a good compromise of accuracy and required resources. In total, the grid has about 15 million cells. A constant CFL number of 1.4 is used, which corresponds to a time step of $\Delta t \approx 1.5\,\text{ns}$.

To obtain dimensionless quantities, the time is normalized with

$$t^* = R_0 \sqrt{\rho_l / \Delta p}, \tag{6.1}$$

where R_0 is the radius at maximum extension, ρ_l the density of the liquid and Δp the driving pressure difference. The wall has a retarding effect on the collapse and thus t^* is longer than the Rayleigh collapse time for spherical collapses ($\tau_C = 0.915\, t^*$). Velocity and pressure are normalized as

$$u^* = \sqrt{\frac{\Delta p}{\rho_l}}, \quad \text{and} \quad p^* = c_l \sqrt{\rho_l \Delta p}, \tag{6.2}$$

where c_l is the liquid speed of sound.

During the simulations, we monitor the integral vapor and gas volumes, the flow field at selected positions and evaluate the maximum pressure induced within the total simulation time. In the results, the pressure signals at the wall-center are presented.

6.3. RESULTS

6.3.1. WALL-ATTACHED BUBBLE WITH $S/R_0 = -0.25$

The collapse behavior of a vapor bubble with $S/R_0 = -0.25$ is visualized in Fig. 6.2. Additionally, the comparison of a vapor bubble and a vapor-gas bubble for two selected time steps and a schematic representation of the collapse behavior are shown. The corresponding temporal evolution of the bubble volume and the recorded pressure signals in the wall-center are in the bottom of the figure.

The wall-attached bubble is pinched circumferentially at its maximum expansion, resulting in a mushroom shape (Fig. 6.2 (ii)). Such behavior was also reported by Shima and Nakajima (1977) and Lauer et al. (2012b). Additionally, a circumferential pinching has been also observed for ellipsoidal bubbles (Pishchalnikov et al., 2019; Lechner et al., 2019). The radially inward directed flow reaches very high velocities, here exceeding 200 m/s ($\approx 20u^*$). Later, the collision of the waterfronts induces a high pressure peak, which can be seen in the pressure signals (Fig. 6.2 bottom left). Shortly afterward the remaining upper part (the 'mushroom head') collapses emitting a shock wave. When this wave reaches the wall, it induces the smaller increase in the pressure signals (Fig. 6.2 bottom left). Due to the conservation of momentum, the preceding radial inward flow at the pinching now causes a flow in upward direction reaching more than 100 m/s ($\approx 10u^*$), see Fig. 6.2 (iv). The rebound takes place in the shear layer resulting in a vapor torus surrounding this flow (Fig. 6.2 (v)).

If gas is present in the vapor bubble, the collapse is slightly decelerated and a higher gas content occurs at the boundary where the vapor has already collapsed, see Fig. 6.2 (iii')(iv'). The retarding effect of the gas is already predicted by the Rayleigh and Keller-Miksis equation (see previous chapter). The gas decelerates the circumferential pinching and reduces its velocity by 3.25%. The reduced velocity correlates with a damped maximum pressure at collision (see Fig. 6.2 bottom left). As expected, the rebound with gas is stronger, as visualized in Fig. 6.2 (iv').

Figure 6.3 shows the distribution of the maximum pressure on the mid-plane and the wall. The highest pressure occurs at the focus point of the collapse. The high pressure along the symmetry line and in the center of the wall is due to the collision of the liquid fronts. The gas dampens the maximum pressure at the focus point by 0.8%, which corresponds to the damping effect in a spherical collapse (see Chapter 5). The maximum wall pressure, on the other hand, is damped by even 1.34%. This demonstrates that gas may have an even stronger damping effect in aspherical collapses than at spherical ones.

Based on the maximum wall pressures, material damage can be estimated. In experiments

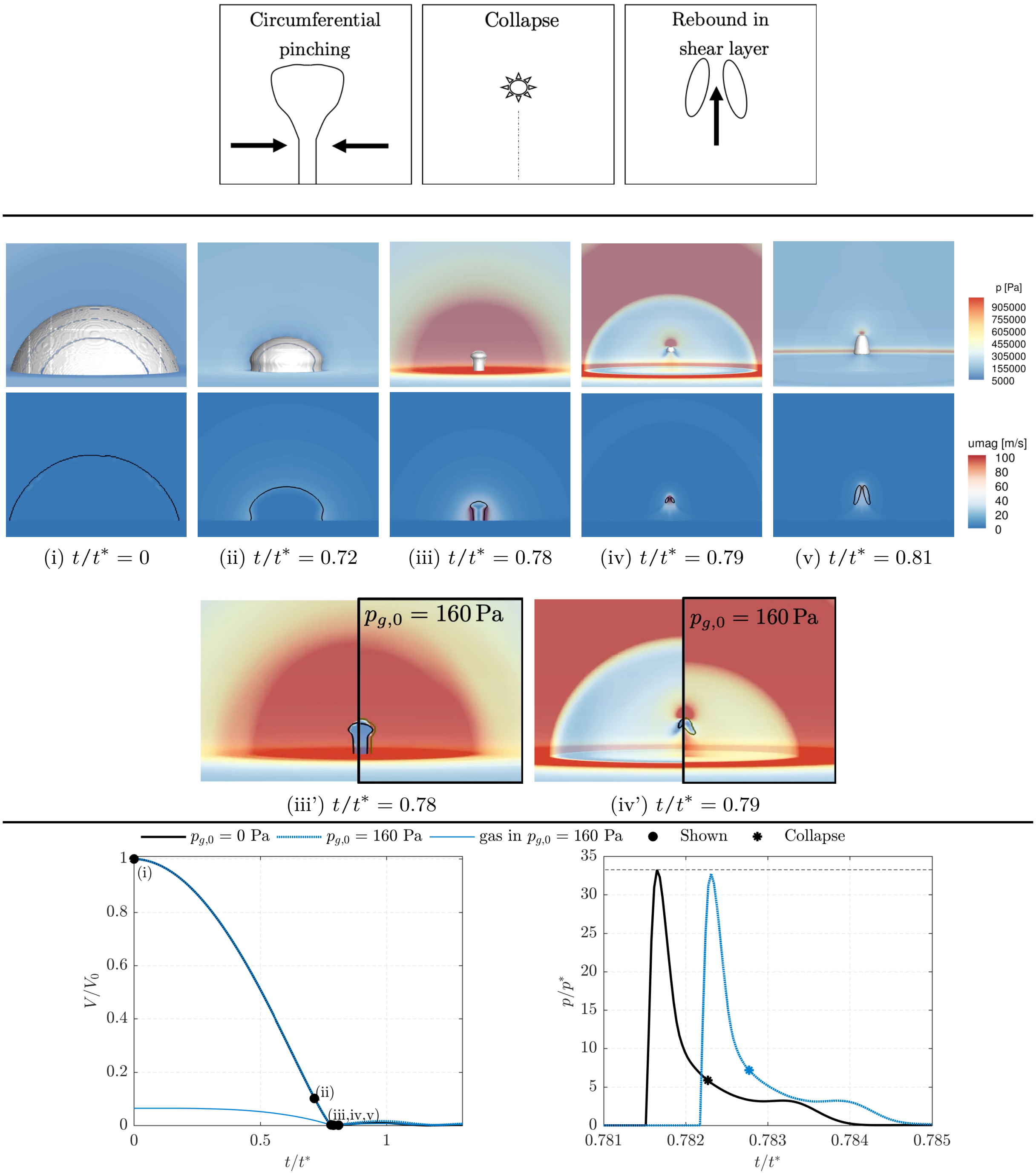

(i) $t/t^* = 0$ (ii) $t/t^* = 0.72$ (iii) $t/t^* = 0.78$ (iv) $t/t^* = 0.79$ (v) $t/t^* = 0.81$

(iii') $t/t^* = 0.78$ (iv') $t/t^* = 0.79$

Figure 6.2.: Collapsing wall-attached bubble with $S/R_0 = -0.25$. Top: Sketch of general collapse behavior. Middle: Time series showing pressure and velocity magnitude on midplane and isosurface/isoline 10% vapor [(i)-(v)] and a comparison of $p_{g,0} = 0\,\mathrm{Pa}$ and $p_{g,0} = 160\,\mathrm{Pa}$ with additionally olive isolines 10% gas [(iii)-(iv)]. Note that the discontinuities in the isosurface are due to post-processing issues. Bottom: Temporal evolution of bubble volume (left), and recorded pressure signals at the wall-center (right).

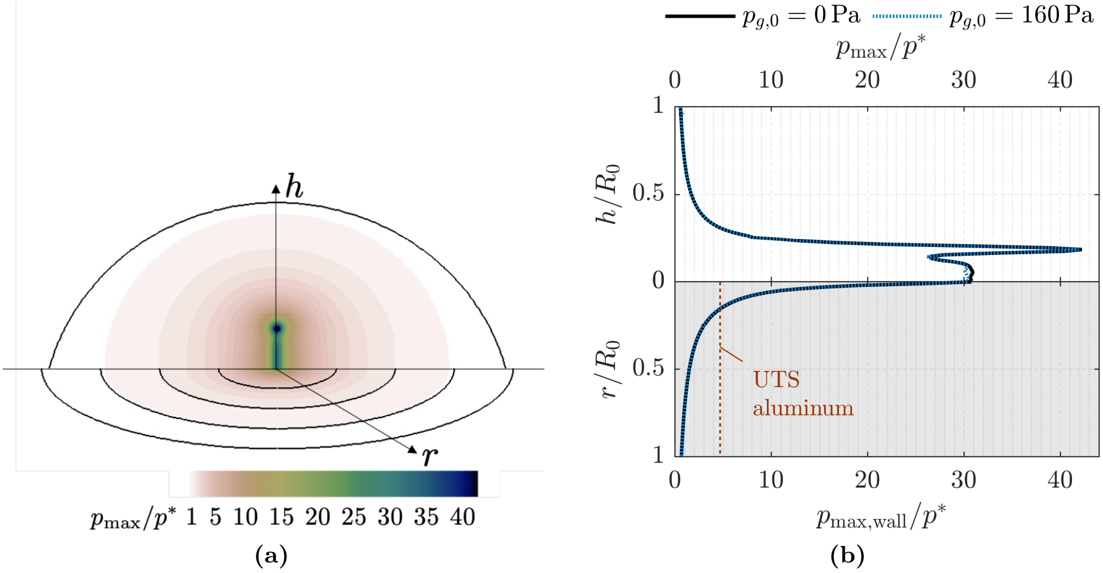

Figure 6.3.: Maximum pressure induced by a collapsing bubble with $S/R_0 = -0.25$. (a) $p_{\max}/p^*$ on the wall (orientation rings at $r/R_0 = 0.25, 0.5, 0.75, 1$) and midplane (initial bubble boundary indicated) (b) extracted p_{max}/p^* and ultimate tensile strength (UTS) of aluminum (70 MPa).

aluminum with an ultimate tensile strength (UTS) of about 70 MPa ($\approx 4.7p^*$) (Malmberg and Käck, 2015) is often used. Taking the UTS as the threshold, the estimated wall damage for aluminum is indicated in Fig. 6.3, and would be a central pit.

6.3.2. WALL-ATTACHED BUBBLE WITH $S/R_0 = 0.5$

Figure 6.4 visualizes the collapse of a vapor bubble. Additionally, the comparison of a vapor bubble and a vapor-gas bubble for two selected time steps, a schematic representation of the collapse behavior, the corresponding temporal evolution of the bubble volume and the recorded pressure signals in the wall-center are shown.

In this configuration, the least resistance of the bubble is in the wall-normal direction and the surrounding pressure distribution leads to an indentation on the upper side. A wall-directed liquid jet forms, penetrating the bubble and resulting in a torus. Then the first collapse takes place, followed by a toroidal rebound and a second collapse. This behavior is well known and has been analyzed in several experimental (Tomita and Shima, 1986; Philipp and Lauterborn, 1998) and numerical studies (Lauer et al., 2012b).

The wall-centered pressure signals (Fig. 6.4 bottom left) show the impact of the jet, followed by two pressure peaks induced by the first collapse. These peaks are significantly higher than the jet induced one, which agrees with the literature (Lauer et al., 2012b; Philipp and Lauterborn, 1998).

The presence of gas, again, results in a higher gas content at the boundary, see Fig. 6.4 (ii'),(iii'). Furthermore, it delays the first collapse, leads to a stronger rebound and a delayed second collapse

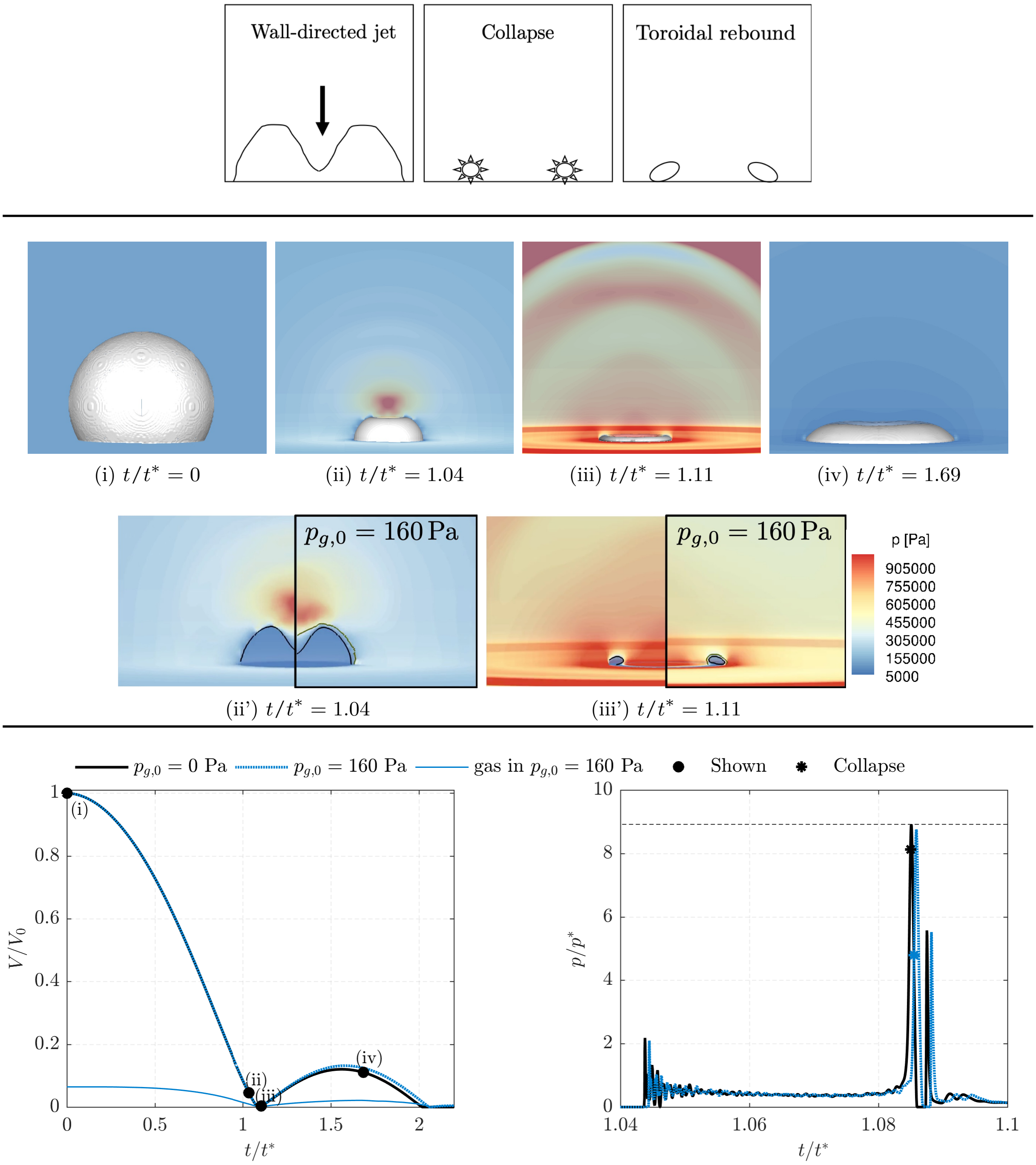

Figure 6.4.: Collapsing wall-attached bubble with $S/R_0 = 0.5$. Top: Sketch of general collapse behavior. Middle: Time series showing pressure on midplane and isosurface 10% vapor [(i)-(iv)] and a comparison of $p_{g,0} = 0\,\mathrm{Pa}$ and $p_{g,0} = 160\,\mathrm{Pa}$ with additional isolines 10% gas (olive) [(ii)-(iii)]. Bottom: Temporal evolution of bubble volume (left), and recorded pressure signals at the wall-center (right).

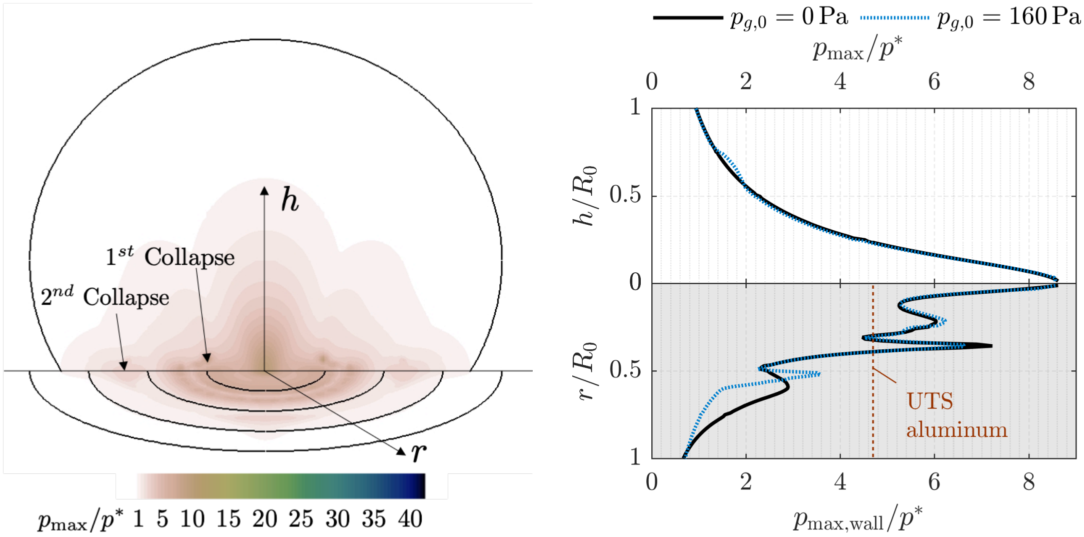

(a) (b)

Figure 6.5.: Maximum pressure induced by a collapsing bubble with $S/R_0 = 0.5$. (a) $p_{\max}/p^*$ on the wall (orientation rings at $r/R_0 = 0.25, 0.5, 0.75, 1$) and midplane (initial bubble boundary indicated) (b) extracted p_{max}/p^* and ultimate tensile strength (UTS) of aluminum (70 MPa).

(Fig. 6.4 bottom). The gas attenuates the velocity of the wall-directed jet and thus the intensity of the jet impact by 3.91%, as can be seen in the pressure signals. The collapse induced pressure peak is also damped by the gas.

The distribution of the maximum pressure is shown in Fig. 6.5. The first collapse induces pressure peaks in the center of the collapsing torus and high pressures at the wall below. However, the highest wall pressure is recorded in the center and induced by the superposition of the emitted pressure waves at first collapse. The second collapse takes place radially further outwards and causes significantly lower wall pressures than the first collapse. If gas is present, the maximum wall pressure induced by the second collapse is higher and shifted radially inwards. Otherwise, the gas slightly dampens the maximum pressures. The damping of the maximum wall pressure at first collapse is even 6.6%. On an aluminum specimen, the collapse would probably lead to ring-shaped damage with radius $r = 0.35R_0$ and an indentation in the center, which matches experimental observations (Philipp and Lauterborn, 1998).

The maximum wall pressure at $S/R_0 = 0.5$ is about a third of the maximum wall pressure at $S/R_0 = -0.25$. This is in agreement with the findings by Lauer et al. (2012b) that the maximum wall pressure decreases with increasing stand-off distance and that this decay is less pronounced for negative stand-off distances.

6.4. CONCLUSIONS AND DISCUSSION

We have performed simulations of bubble collapses driven by atmospheric pressure and investigated the collapse behavior and pressure impact for the two selected stand-off distances $S/R_0 = -0.25$

and $S/R_0 = 0.5$. The employed modeling approach considers phase change and compressibility and thus captures the emitted pressure waves and the rebound.

The observed collapse behavior resembles that of previous investigations at higher driving pressure differences. Our simulation results provide deeper and additional insights into the rebound behavior and the relevant mechanisms for pressure peaks. We could show that at $S/R_0 = -0.25$ the collision of the circumferential pinching induces the maximum wall pressure and not the final collapse. At $S/R_0 = 0.5$, we captured the first and second toroidal collapse and the induced wall pressures of both. The induced wall pressure of the second collapse is weaker and radially further outward.

Additionally, we have evaluated the effects of gas inside the vapor bubble. The gas decelerates the collapse and reduces the velocity of the liquid jets, i.e. the circumferential pinching or the wall-directed jet. And as expected, gas dampens the collapse pressure and enhances the rebound. We found that the damping of the maximum wall pressure by the gas depends on the mechanism inducing this pressure. Nevertheless, our simulations of bubbles containing gas might be biased by the employed modeling approach. We assume isothermal gas and initialize a relatively high gas content of $p_{g,0} = 160\,\mathrm{Pa}$ compared to the assumed $p_{g,0} = 3 - 10\,\mathrm{Pa}$. The ψ-equivalence, which justifies this initial value, was only shown for spherical collapse (see Chapter 5). To evaluate the effect of the gas in detail, adiabatic modeling of the gas has to be employed. Moreover, further experimental and numerical investigations are generally necessary to quantify the effect of gas inside vapor bubbles. A major uncertainty for these studies is that the actual gas content is generally unknown and very difficult to estimate.

7. GAS BUBBLE COLLAPSING ABOVE A CREVICE

In the following chapter, we investigate the near-surface dynamics of a gas bubble collapsing above a crevice. This study was conducted with the open-source flow solver ECOGEN.

The chapter is based on a paper submitted to the Journal of Fluid Mechanics (Trummler et al., 2020a).

7.1. MOTIVATION

Several studies have analyzed bubbles collapsing near smooth walls, as discussed in Chapter 1. However, such configurations represent the wall pressure and collapse dynamics only if the length scale of the wall roughness is much smaller than the nominal bubble size. When this condition is not satisfied, the bubble collapse, and thus its effect on near-wall erosion, can change qualitatively (Tomita et al., 2002; Zhang et al., 2018). The broad list of applications with bubble sizes in the same order as the surface topology including urinary stones ablation (Pishchalnikov et al., 2003), surface cleaning (Ohl et al., 2006; Reuter et al., 2017), cavitation in micro-pumps (Dijkink and Ohl, 2008) and pressurized auto-injectors (Veilleux et al., 2018) motivates the study of bubble collapse dynamics in this regime.

Our goal is to determine how a surface crevice modifies the collapse of a near-wall bubble and to assess the associated modification of wall pressure, jet and shock formation, and wave interactions, which are of principal importance when considering erosion and damage potential (Brennen, 1995; Pöhl et al., 2015). For this purpose, the collapse of a spherical gas bubble near or attached to a wall with a cylindrical notch is analyzed. We use numerical simulations to characterize qualitative and quantitative differences of collapse behavior associated with the surface geometry.

The specific configurations considered are presented in Section 7.2 and include variations in notch size and bubble-wall stand-off distance. The variation in notch size serves as a representation of the varying degrees of surface roughness present in engineering and medical applications, whereas the stand-off distance has a significant impact on the collapse dynamics and wall-pressure for smooth-wall cases (Tomita and Shima, 1986; Philipp and Lauterborn, 1998; Lauer et al., 2012b). The collapse behavior of the bubble is analyzed for such configurations in Section 7.3, followed by an assessment of induced wall-pressures. Section 7.4 summarizes this chapter.

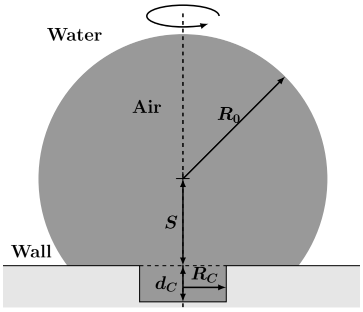

Figure 7.1.: Schematic of the problem set-up.

7.2. SET-UP

Figure 7.1 shows the flow configuration considered. The initial bubble is spherical with radius R_0 and stand-off distance S above a cylindrical crevice of radius R_C and depth $d_C = 0.25R_0$. The spherical shape is chosen as an approximation of the geometry of an expanded cavitation bubble at its maximum volume. We define the stand-off distance S as the distance from the wall to bubble-center for $R_C/R_0 \leq 0.5$ and as the distance from the crevice-bottom to bubble-center for $R_C/R_0 > 0.5$. This definition ensures consistency for both limiting cases $R_C/R_0 \to 0$ and $R_C/R_0 \to \infty$.

We consider a $R_0 = 400\,\mu\text{m}$ bubble filled with non-condensable gas of initial pressure $p_B = 3000\,\text{Pa}$ and density $\rho_g = 0.035\,65\,\text{kg}\,\text{m}^{-3}$. Bubbles commonly used in relevant applications predominately consist of non-condensable gas. Furthermore, the collapse dynamics are also only weakly sensitive to the internal bubble pressure when the driving pressure differences are large (Pishchalnikov et al., 2019).

The bubble is surrounded by water with a density of $\rho_l = 1002.7\,\text{kg}\,\text{m}^{-3}$ and varying pressure

$$p(\hat{r}, t = 0) = p_\infty + \frac{R_0}{\hat{r}}\left(p_B - p_\infty\right) \quad \text{for} \quad \hat{r} > R_0, \tag{7.1}$$

where $\hat{r}$ is the radial coordinate with its origin at the bubble center. This initialization matches the pressure distribution predicted by the Rayleigh equation for the Besant problem (Brennen, 1995; Besant, 1859). For the configurations considered, it provides a valid approximation of the realistically evolving pressure field and suppresses the formation of spurious pressure waves due to pressure jumps (Tiwari et al., 2013, 2015). Further, it has been established that this approximation evolves towards an exact solution of the Besant problem within a very short time (Rasthofer et al., 2019). We use $p_\infty = 10^7\,\text{Pa}$, which matches that of previous studies (Lauer et al., 2012b; Beig et al., 2018) and serves as a representation of actual applications involving liquid cavitation, such as high-pressure pumps (Bohner et al., 2001).

Figure 7.2 shows the computational grid. The bubble collapse process is assumed to be axisymmetric with radial coordinate r, and thus a 2D axisymmetric domain of radius and length $25R_0$ is used, matching that of previous studies of smooth-wall collapse (Lauer et al., 2012b). The grid is equally spaced with 400 finite volumes per R_0 near the bubble (until $\hat{r} = 1.5R_0$) and is progressively stretched farther from the bubble with a stretching factor of 1.01 in each direction. This resolution has been shown to be sufficient for the conditions considered

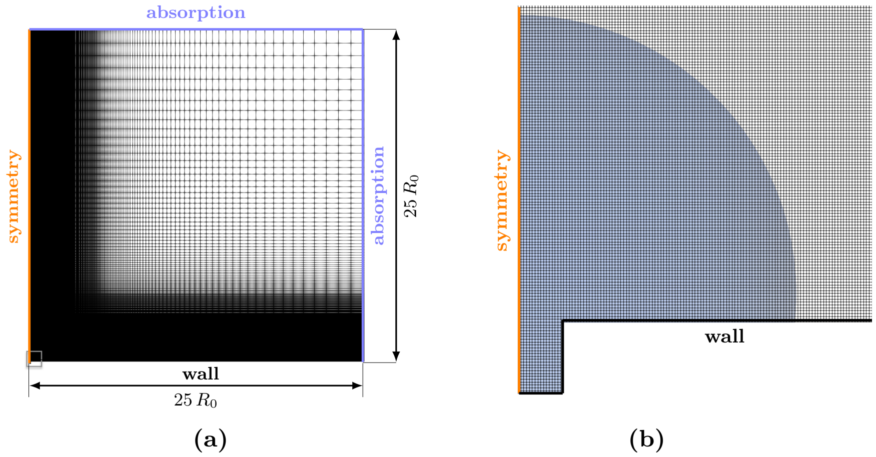

Figure 7.2.: (a) 2D axisymmetric grid configuration and boundary conditions for example case small crevice ($R_C/R_0 = 0.15$) and a stand-off distance of $S/R_0 = 0.35$. (b) Magnification of the near-bubble region with the bubble shaded. Only every fourth grid-line is shown in each coordinate direction.

here (Lauer et al., 2012b; Pöhl et al., 2015; Beig et al., 2018). Non-reflecting boundary conditions are used at the outer boundaries to suppress reflecting pressure waves at these locations (Toro, 1997). This involves solving a Riemann problem at an outer boundary by assuming identical primitive variables on both sides of the boundaries. A constant CFL number of 0.4 is used, which corresponds to a time step of $\Delta t \approx 0.15\,\mathrm{ns}$. The total simulation time is $6\,\mu\mathrm{s}$, or about $1.5t^*$ where

$$t^* = R_0\sqrt{\frac{\rho_l}{\Delta p}} \tag{7.2}$$

is an estimate of the collapse time of a bubble collapse near a solid wall (Plesset and Chapman, 1971), where $\Delta p \equiv p_\infty - p_B$ is the driving pressure difference. The wall has a retarding effect on the collapse and thus t^* is longer than the Rayleigh collapse time for spherical collapses ($t_{\mathrm{Rayleigh}} = 0.915\,t^*$). Velocity and pressure are normalized as

$$u^* = \sqrt{\frac{\Delta p}{\rho_l}}, \quad \text{and} \quad p^* = c_l\sqrt{\rho_l \Delta p}, \tag{7.3}$$

where c_l is the liquid speed of sound.

7.3. RESULTS

7.3.1. CONSIDERED CONFIGURATIONS

We use stand-off distances $S/R_0 = 0.1$, 0.35, 0.6, and 1.1 (wall-detached). For each stand-off distance we consider a smooth wall ($R_C = 0$), a small crevice ($R_C/R_0 = 0.15$) and a large crevice ($R_C/R_0 = 0.75$), as shown in Fig. 7.3.

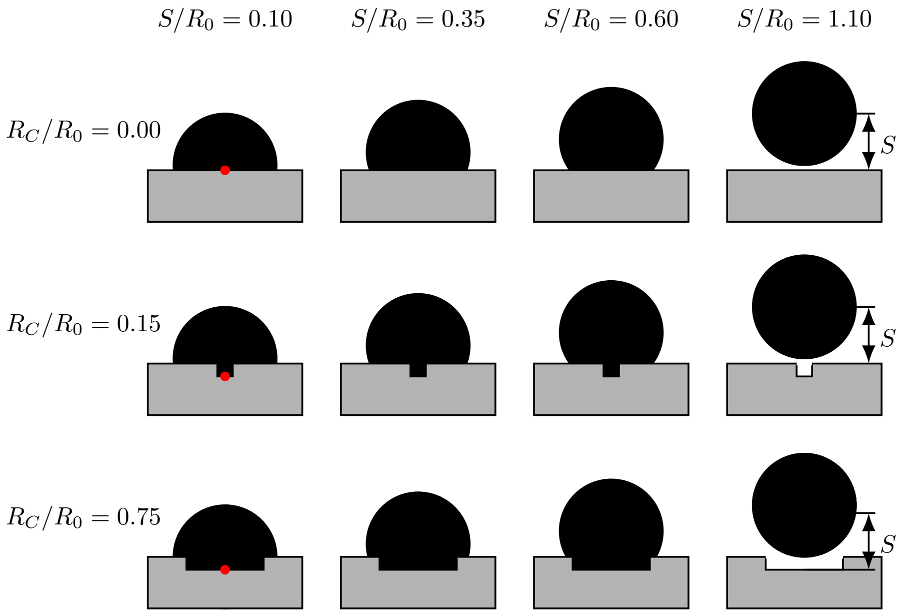

Figure 7.3.: Overview of the investigated configurations. The red circle shows the $r = 0$ wall-centered position used to observe the pressure impact. Rows correspond to constant crevice size R_C/R_0 and columns correspond to constant stand-off distance S/R_0. The stand-off distance S is also shown; its definition is modified to be measured from the bottom of the crevice for the $R_C/R_0 = 0.75$ cases.

We first analyze the collapse behavior of wall-attached bubbles by increasing crevice size (smooth wall in Section 7.3.2, small crevice in Section 7.3.3 and large crevice in Section 7.3.4), and then consider detached bubbles in Section 7.3.5. In Section 7.3.6, we compare the pressure impact on the wall for all configurations and assess the cavitation erosion potential.

7.3.2. SMOOTH-WALL-ATTACHED BUBBLE COLLAPSE $R_C = 0$

Figure 7.4 visualizes the flow of a collapsing wall-attached bubble using the pressure field p and numerical schlieren Φ (Quirk and Karni, 1996) as

$$\Phi = \exp\left(-\frac{k|\nabla\rho|}{\max|\nabla\rho|}\right), \tag{7.4}$$

where $k = 400$ is used to ensure waves in the liquid are visible (Johnsen, 2007; Meng and Colonius, 2018). The corresponding pressures at the center of the wall are shown in Fig. 7.5.

For all cases a wall-directed jet is formed during the initial collapse phase. The jet impinges on the wall (row ii) leading to a pressure wave. At subsequent times the remaining toroidal bubble continues to collapse, emitting a pulse that travels radially inward and collides at $r = 0$.

The collapse of the torus becomes increasingly non-uniform, with a portion near the wall being pinched away from the main torus which is in agreement with experimental observations (Lindau and Lauterborn, 2003). Pressure waves emitted near the pinching location are evident, starting

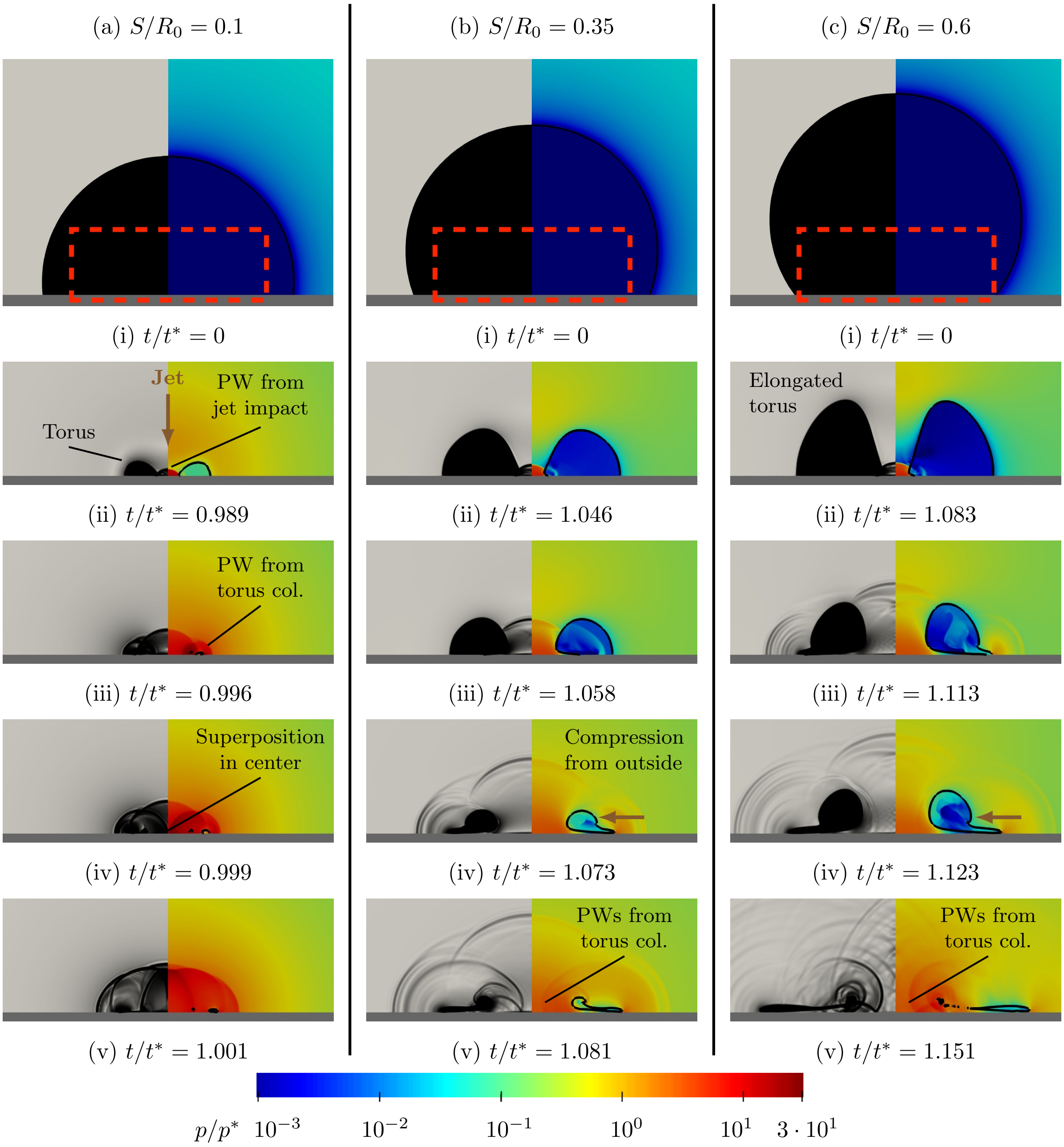

Figure 7.4.: Numerical schlieren (left) and log-scale pressure fields (right) of an air bubble collapsing onto a smooth wall of varying stand-off distances S/R_0 (a)–(c) at selected times (i)–(v). Gas volume fraction β_g is shown as a shaded area of decreasing opacity with decreasing β_g (left), while the $\beta_g = 0.5$ bubble interface is shown as a solid curve (right). (ii)–(v) are magnified to the – – – rectangular region of (i). Selected pressure waves (PW) and collapse dynamics (col.) are also identified.

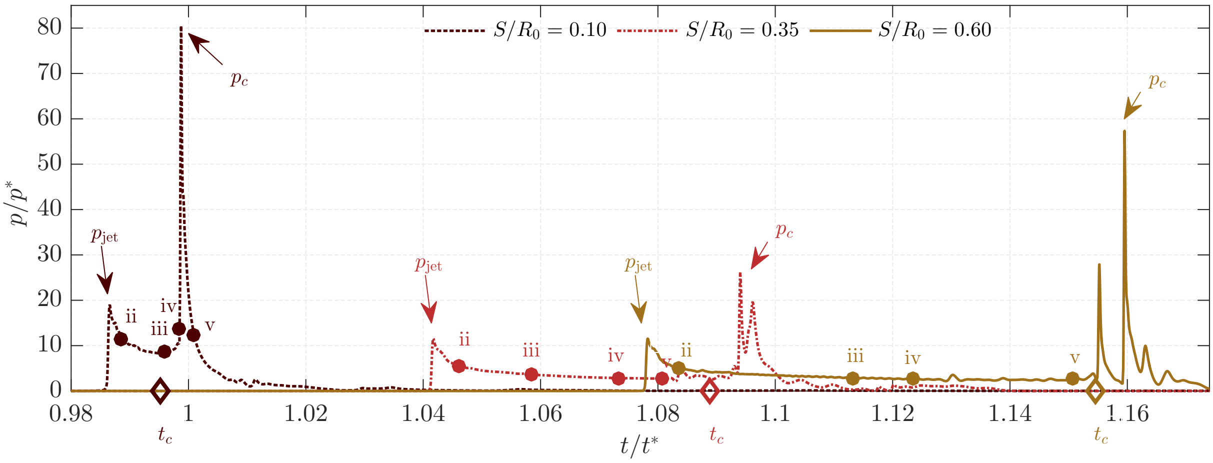

Figure 7.5.: Evolution of the wall-centered pressure for the smooth-wall case at varying stand-off distances S/R_0. The time instances shown in Fig. 7.4 are highlighted and labeled with the corresponding row (ii–v). The pressure peaks induced by the jet impact p_{jet} and the collapse p_c are indicated as such. The collapse time t_c is plotted as a diamond on the x-axis.

in (b,iv) and (c,iii) respectively. In addition, a compression of the torus from the outside pushes its upper part towards the center (b,iv), (c,iv). During the final collapse phase, two pressure waves propagate inward, focus, and result in two distinct pressure pulses at the wall center, as visible in Fig. 7.5.

The impact of a liquid jet onto the wall generates a water hammer pressure proportional to the jet velocity $p_{\text{jet}} \propto \rho_l \, c_l \, u_{\text{jet}}$. The jet-induced pressure peak p_{jet} is clearly visible from the wall-centered pressure signals of Fig. 7.5. For $S/R_0 = 0.1$, the peak is about twice as high as for the others. The high jet velocity at this small stand-off distance is a result of the bubble shape being almost hemispherical. A hemispherical bubble attached to an inviscid wall collapses like a spherical bubble with a uniform and high acceleration of the interface. For $S/R_0 = 0.1$ the initial stages of the collapse resemble those of a collapsing spherical bubble, with the formation of the liquid jet immediately preceding the total collapse and the jet reaching a high velocity. Similar observations were made by Philipp and Lauterborn (1998), who also experimentally recorded the highest jet-induced pressures at small stand-off distances.

In the configurations considered, the total collapse is the collapse of the gas torus. We determine the collapse time t_c by the minimum gas volume. The pressure waves emitted at total collapse result in collapse-induced pressure peaks p_c (see Fig. 7.5). Thus, the jet impact on the wall, as well as the shock waves emitted during total collapse, cause high pressure peaks and potentially material damage. For the rough wall cases, we also observe pressure peaks induced by post-collapse wave dynamics. For the smooth-wall cases, p_c is significantly higher than p_{jet}, which agrees with the findings of Lauer et al. (2012b).

In Fig. 7.6 the maximum wall pressure $p_{\max}$ is compared with that of Lauer et al. (2012b) for our present resolution (400pts$/R_0$) and 100pts$/R_0$, which matches their study. The current results follow the same trends, although with lower pressures for the attached-bubble cases ($S < R_0$). The maximum pressure is known to be sensitive to resolution, although a discrepancy

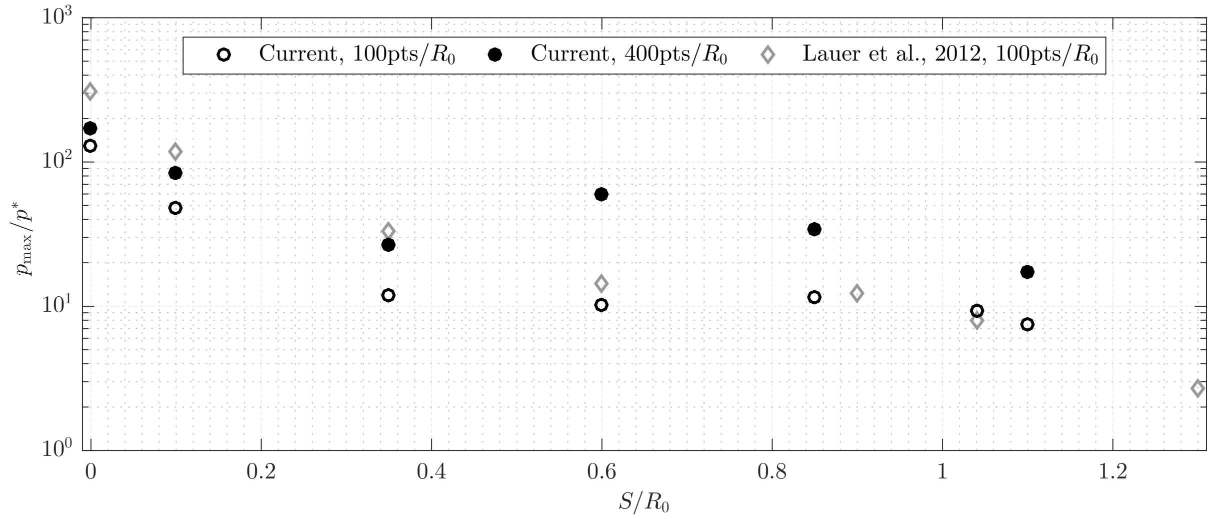

Figure 7.6.: Maximum wall pressure for a smooth-wall-attached bubble of varying stand-off distance S/R_0 and grid resolution as labeled. Results from Lauer et al. (2012b) are also shown for comparison.

also exists for identical grid resolutions (100pts/R_0). Lauer et al. (2012b) consider condensation, while we model the bubble content as non-condensable gas. The damping of the maximum pressure observed is consistent with previous analysis of bubbles containing non-condensable gas (Trummler et al., 2018a; Pishchalnikov et al., 2019). Further, the observed decrease of the maximum wall pressure with increasing stand-off distance matches experimental observations for wall-attached bubbles at atmospheric conditions (Shima et al., 1983, 1984; Tomita and Shima, 1986) and is consistent with measured cavitation damage depths (Philipp and Lauterborn, 1998).

7.3.3. SMALL CREVICE $R_C/R_0 = 0.15$

Visualizations of a collapsing $R_C/R_0 = 0.15$ crevice-wall-attached bubble at varying stand-off distances S/R_0 are shown in Fig. 7.7 and the corresponding wall pressures are shown in Fig. 7.8.

For the smallest stand-off distance case ($S/R_0 = 0.1$), the initial stages of the collapse match that of the smooth-wall cases, with a jet piercing the bubble and generating a toroidal structure. However, in this case the gas torus is ultimately fully contained in the crevice. As shown in (a,iii), a pressure wave is emitted when the liquid has reached the sharp edge of the crevice and is suddenly stopped there. This wave propagates radially outwards (a,iv) and collides in the center inducing a small pressure peak at the wall-center, see p_{PW1} in Fig. 7.8. The pressure wave continues to travel towards the other crevice side pushing the gas away from the crevice bottom and pressing it against the opposite side wall (a,v). Between (a,iv) and (a,v) the pressure wave and its reflections induce high pressure fluctuations at the wall center (p_{PW2}). The last time step depicted (a,v) is close to the final collapse, which causes the highest pressure peak.

For the larger stand-off distances $S/R_0 = 0.35$ and 0.6, the jet penetrates the entire bubble and hits the crevice bottom. A gas torus remains on the upper wall and a gas layer covers the side walls. Like in the smooth wall cases, the gas torus outside of the crevice collapses ((b,iv),

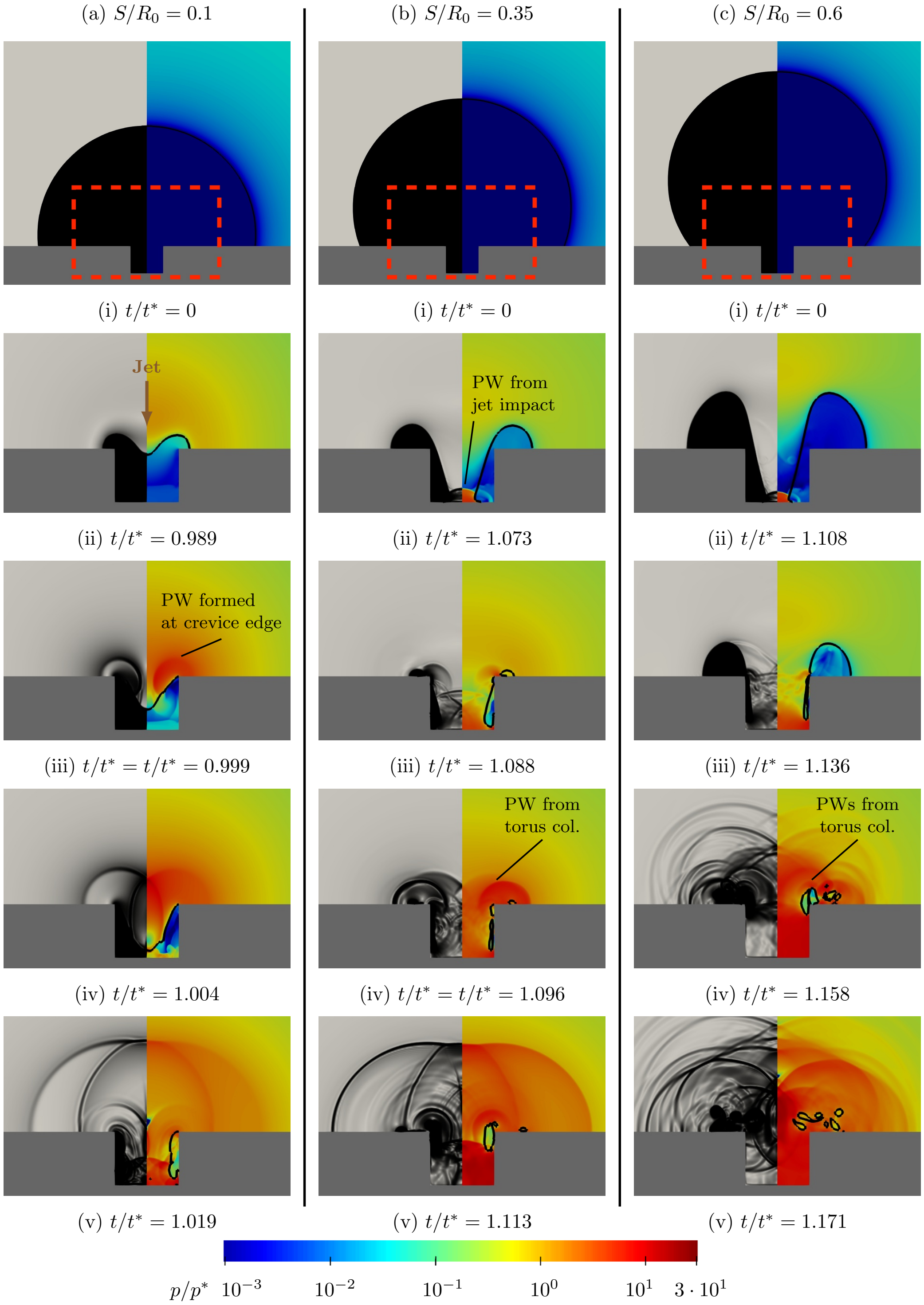

(a) $S/R_0 = 0.1$

(i) $t/t^* = 0$

(ii) $t/t^* = 0.989$

(iii) $t/t^* = t/t^* = 0.999$

(iv) $t/t^* = 1.004$

(v) $t/t^* = 1.019$

(b) $S/R_0 = 0.35$

(i) $t/t^* = 0$

(ii) $t/t^* = 1.073$

(iii) $t/t^* = 1.088$

(iv) $t/t^* = t/t^* = 1.096$

(v) $t/t^* = 1.113$

(c) $S/R_0 = 0.6$

(i) $t/t^* = 0$

(ii) $t/t^* = 1.108$

(iii) $t/t^* = 1.136$

(iv) $t/t^* = 1.158$

(v) $t/t^* = 1.171$

Figure 7.7.: Numerical schlieren (left) and pressure fields (right) of an air bubble collapsing onto a wall with a small crevice $R_C/R_0 = 0.15$ at varying stand-off distances S/R_0 (a)–(c) at selected times (i)–(v). (ii)–(v) are magnified to the – – – rectangular region shown in (i). Selected pressure waves (PW) and collapse dynamics (col.) are also identified.

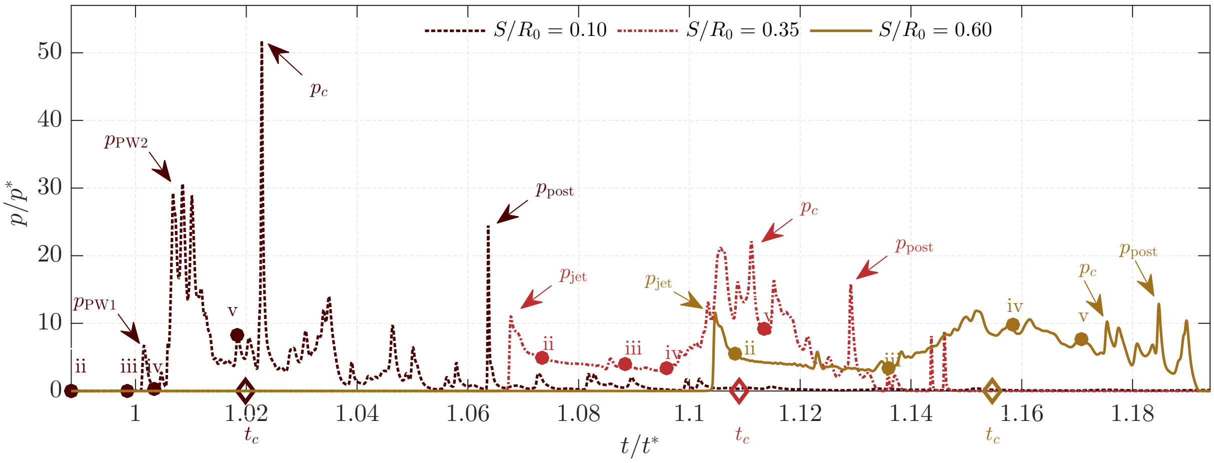

Figure 7.8.: Evolution of the wall-pressure at $r = 0$ for the case $R_C/R_0 = 0.15$ at varying stand-off distances S/R_0. The time instances shown in Fig. 7.7 are highlighted and labeled with the corresponding row (ii–v). The pressure peaks induced by the jet impact p_{jet}, the pressure-wave p_{PW}, the collapse p_c and post-collapse wave dynamics p_{post} are indicated as such. The collapse time t_c is plotted as a diamond on the x-axis.

(c,iv)), emitting intense pressure waves. These waves propagate radially outward, interfere with each other, and are reflected within the crevice. The time steps (b,v) and (c,v) both visualize the complex wave pattern after the total collapse.

Figure 7.8 shows that the wall-centered pressures associated with the $S/R_0 = 0.35$ and 0.6 cases are qualitatively similar. Both have a pressure peak due to the jet impact, followed by a time-delayed accumulation of pressure peaks during and after the final collapse phase. For $S/R_0 = 0.6$ these pressure peaks are smaller since the intense pressure waves are more concentrated in the area above the crevice (see (c,iv,v)) and thus decay until they reach the crevice bottom.

At all stand-off distances, significant pressure peaks are induced by post-collapse wave dynamics (see p_{post} in Fig. 7.8).

7.3.4. LARGE CREVICE $R_C/R_0 = 0.75$

We next consider the large crevice $R_C/R_0 = 0.75$ cases. Recall that S is now measured from the bottom of the crevice wall to the bubble center, instead of from the top of the crevice wall. Figure 7.9 visualizes the collapses and the corresponding wall-centered pressures are shown in Fig. 7.10.

For the $S/R_0 = 0.1$ case (column a), the fraction of the bubble surface initially exposed to the high-pressure liquid is comparable to that of a bubble with a small negative stand-off distance ($S/R_0 - d/R_0 = 0.1 - 0.25 = -0.15$). Consequently, the initial collapse phase resembles that of such a configuration. Lauer et al. (2012b) and Shima and Nakajima (1977) report a collapse behavior similar to that of a spherical collapse with an additional circumferential pinching at the position of maximum extension, resulting in a mushroom-shape. Here, (a,ii) shows

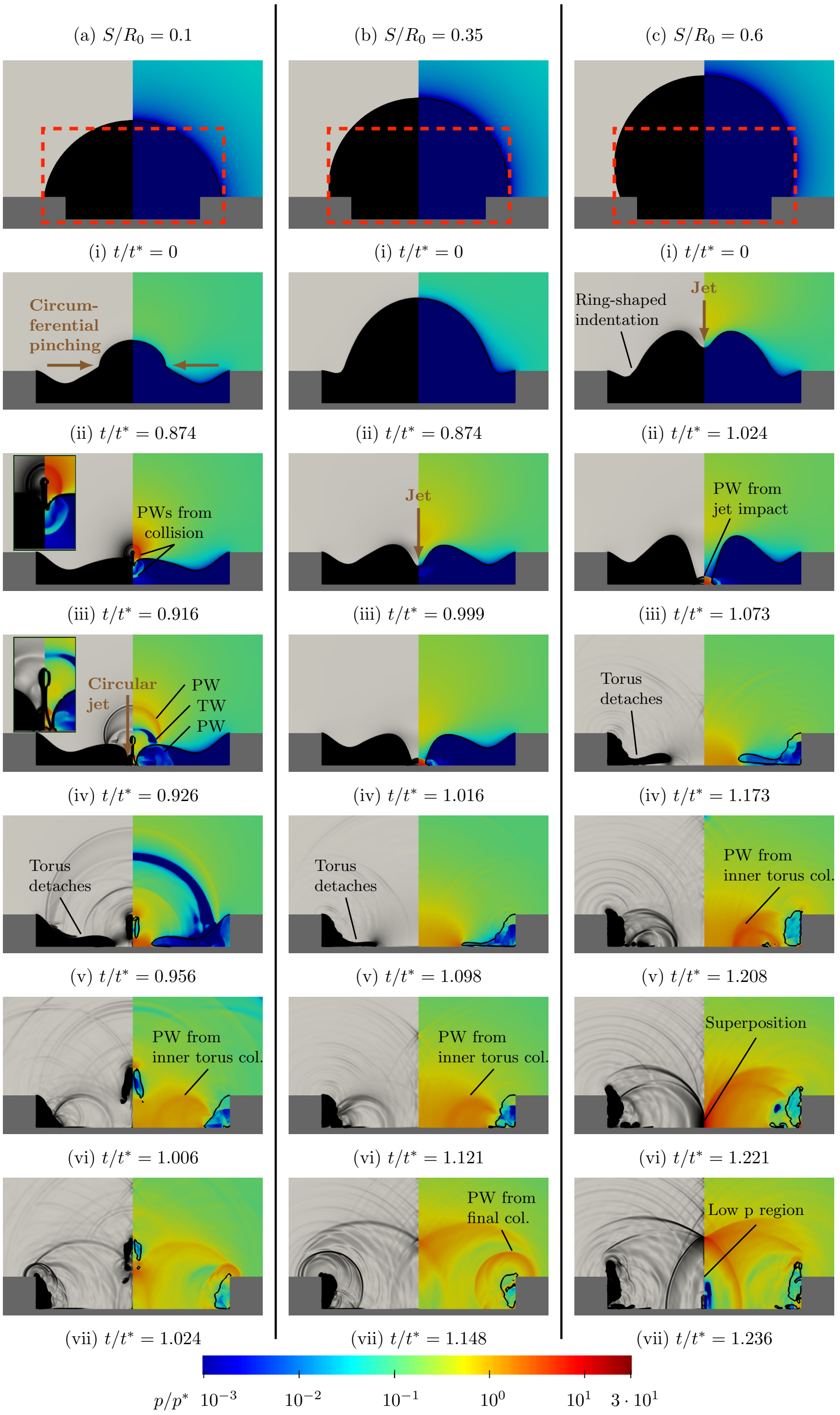

Figure 7.9.: Numerical schlieren (left) and pressure fields (right) of an air bubble collapsing onto a wall with crevice size $R_C/R_0 = 0.75$ at varying stand-off distances S/R_0 (a)–(c) at selected times (i)–(vii). In (a,iii) and (a,iv) the relevant areas are additionally magnified in the upper left corner. (ii)–(vii) are magnified to the – – – rectangular region shown in (i). Selected pressure waves (PW), tension waves (TW), and collapse dynamics (col.) are also identified.

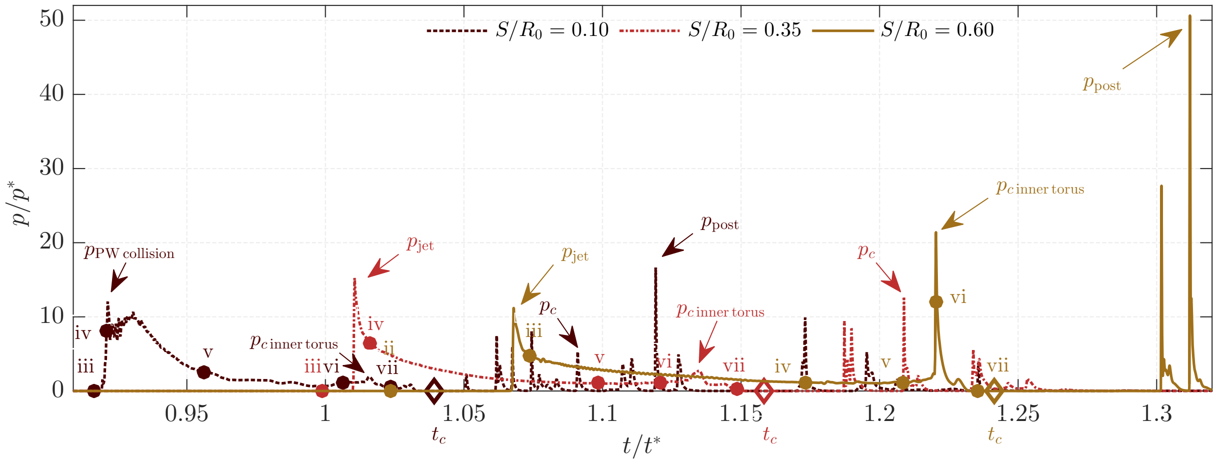

Figure 7.10.: Evolution of the wall-pressure at $r = 0$ for the case $R_C/R_0 = 0.75$ at varying stand-off distances S/R_0. The time instances shown in Fig. 7.9 are highlighted and labeled with the corresponding row (ii–vii). The pressure peaks induced by the jet impact p_{jet}, the collision of the pressure-wave $p_{\text{PW collision}}$, the collapse of the inner torus $p_{c\,\text{inner torus}}$, the total collapse p_c and post-collapse wave dynamics p_{post} are indicated as such. The collapse time t_c is plotted as a diamond on the x-axis.

the compressed upper part of the bubble and also a circumferential pinching. Additionally, a ring-shaped indentation of the bubble can be observed.

The circumferential pinching meets at the $r = 0$ axis of symmetry, generating a pressure wave (a,iii), which propagates radially outward in the liquid and the gas. When the pressure wave in the gas reaches the bottom wall, it induces a pressure peak there (see Fig. 7.10, $p_{\text{PW collision}}$). The pressure wave in the liquid is partially reflected at the gas-liquid interface, and generates a tension wave following the initial pressure wave (a,iv,v). Furthermore, the collision of the circumferential pinching results in the formation of a wall-normal circular jet, see (a,iii,iv). The subsequent circular jet impacts on the bottom wall and pushes away the gas in the crevice center. A secondary bubble pinches off and moves upwards (a,v). From the remaining flattened gas torus, an inner gas torus detaches at the position of the ring-shaped indentation, collapses (a,vi) and emits a pressure wave propagating in the direction of $r = 0$ (a,vii). At the same time, the remaining gas is pressed towards the crevice side walls and pressure waves are formed at the sharp edges of the crevice (a,vii).

For the $S/R_0 = 0.35$ and 0.6 cases (Fig. 7.9 (b) and (c)), a ring-shaped indentation forms close to the crevice edge during the initial collapse phase, similar to that of the $S/R_0 = 0.1$ case. In addition, the jet indents the bubble from the top, as observed for the small crevice and the smooth wall configurations. (b,iv) and (c,iii) show that the larger stand-off distance results in a more curved bubble interface when the jet impacts the wall. Similar to the $S/R_0 = 0.1$ case, an inner torus detaches from the main torus at the position of the ring-shaped indentation ((b,v) and (c,iv)) and collapses, emitting a pressure wave ((b,vi) and (c,v)). The pressure wave propagates to the center, collides there inducing a pressure peak (c,vi) ($p_{c\,\text{inner torus}}$) and then continues, resulting in a low-pressure area (c,vii). This pressure decrease can cause a vapor bubble rebound when phase-change processes are taken into account. The final collapse occurs when the remaining gas torus in the corner of the crevice is compressed to its minimum size (b,vii).

The pressure signals in Fig. 7.10 show the jet-induced pressure peak p_{jet} for $S/R_0 = 0.35$ and $S/R_0 = 0.6$. For $S/R_0 = 0.35$ p_{jet} is higher because the initially liquid-exposed part of the bubble interface is almost a hemisphere and is thus strongly accelerated, see also Section 7.3.2. For $S/R_0 = 0.1$, there is no jet-induced pressure peak in the center due to the circular jet. However, a pressure peak of about the same intensity is induced by the pressure wave emitted when the circumferential pinching collides ($p_{\text{PW collision}}$).

This first peak is followed by a peak $p_{c\,\text{inner torus}}$ caused by the collapse of the inner detached torus. As S/R_0 increases, this pressure peak increases since the volume of the detached inner torus increases, resulting in a stronger pressure wave. Due to the preceding collapse of the inner torus, a smaller gas volume is associated with the final collapse phase. Furthermore, the collapse occurs at the crevice corner, and thus the induced pressure waves are less intense at the wall-center. As a result, the collapse-induced pressure peak in the center p_c is comparatively small and is exceeded by p_{jet} (or respectively by $p_{\text{PW collision}}$). Indeed, for $S/R_0 = 0.6$, the total collapse does not generate a pressure peak at the wall center.

After the final collapse, intense wave dynamics occur, which can lead to high pressure peaks. For $S/R_0 = 0.1$ and 0.6, these post-collapse pressure peaks p_{post} are the maximum pressure observed.

7.3.5. COLLAPSE OF A WALL-DETACHED BUBBLE ($S/R_0 = 1.1$)

The collapse of wall-detached bubbles ($S/R_0 = 1.1$) are visualized in Fig. 7.11 for varying crevice sizes. The corresponding wall-centered pressure evolution is shown in Fig. 7.12. As observed for previous cases, the aspherical pressure distribution leads to an indentation of the top of the bubble and the formation of a jet penetrating the bubble for all cases. The monitored jet velocities are about $u_{\text{jet}}/u^* \approx 10$, which is in good agreement with previous studies for smooth walls (Lauer et al., 2012b; Supponen et al., 2016).

For the smooth-wall case (Fig. 7.11 (a)) the jet impacts the far-side bubble interface at $t = 1.1t^*$ and a pressure wave is emitted (a,iii). The impact time of the jet at the bubble wall and the bubble position with respect to the initial configuration are in good agreement with previous observations (Supponen et al., 2016). The jet impact results in an upward and a downward moving wave front (see (a,iv)), with the latter being curved. The numerical schlieren shows an additional downward moving density jump corresponding to a contact wave. When the downward moving pressure wave impacts the wall, a pressure peak is induced (see also Fig. 7.12, $p_{\text{PW jet}}$). The pressure wave is then reflected at the wall (a,v), compressing the remaining bubble torus from bottom to top (a,vi) leading to the total collapse. After the collapse (a,vii–ix), a gas torus rebounds and moves towards the wall. The pressure waves due to the jet impact and toroidal collapse compare well with the visualized wave patterns of Supponen et al. (2015).

Figure 7.11 (b) shows that the small crevice does not significantly change the collapse and rebound behavior compared to the smooth wall. The main difference is the reflection of the pressure wave emitted at jet-bubble-impact at the crevice edge (b,iii–iv) and the resulting different

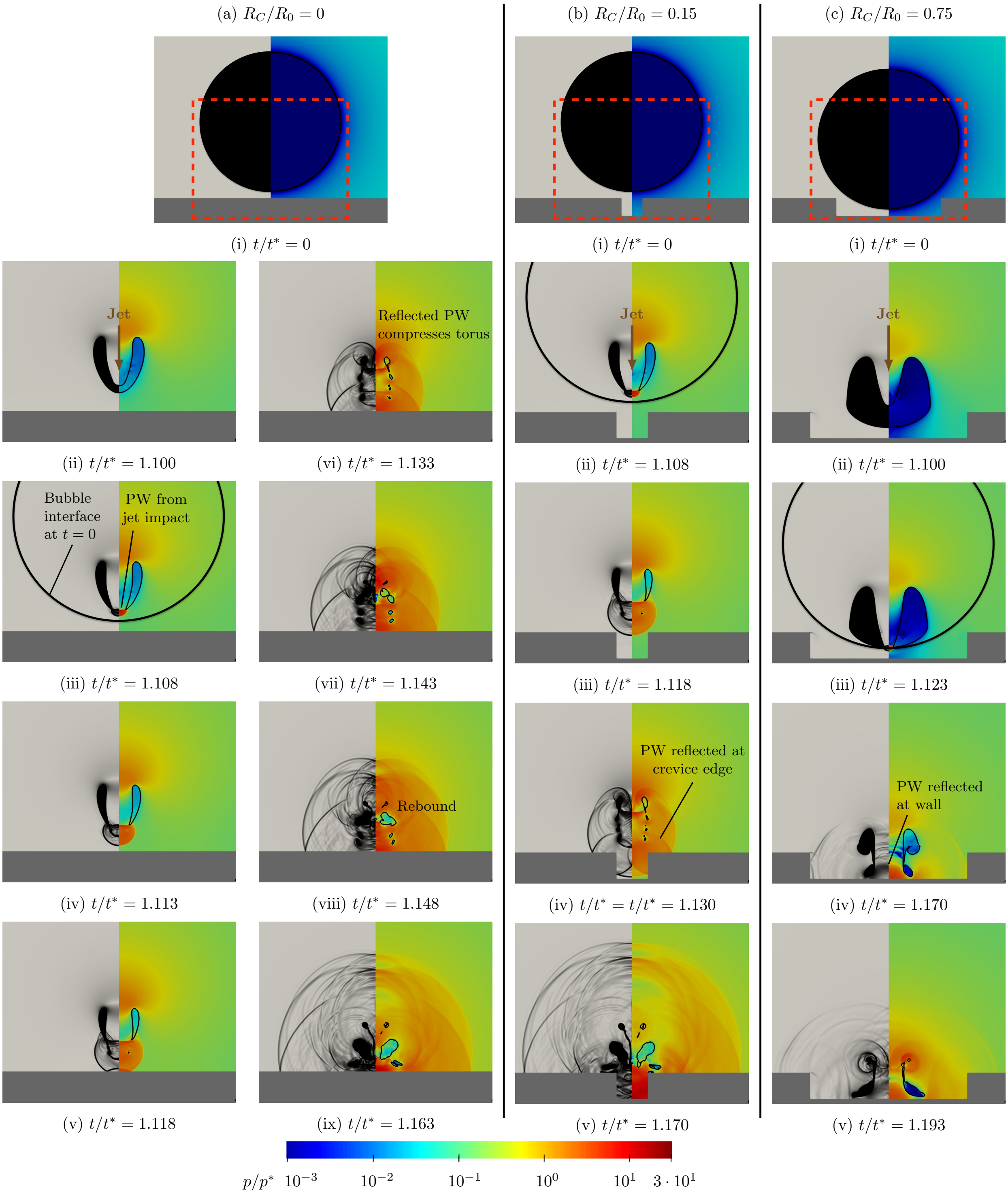

Figure 7.11.: Numerical schlieren (left) and pressure fields (right) of a wall-detached air bubble ($S/R_0 = 1.1$) collapsing onto a wall of varying crevice size R_C/R_0 (a)–(c) at selected times as labeled. (ii)–(ix) are magnified to the – – – rectangular region shown in (i). The solid curve in (a,iii), (b,ii) and (c,iii) indicates the initial position of the bubble interface. Selected pressure waves (PW) are also identified.

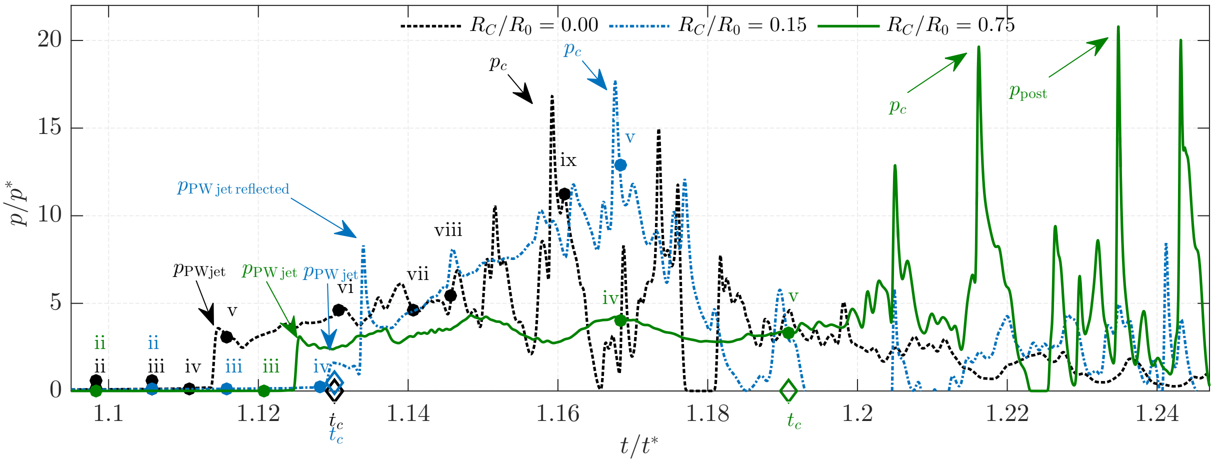

Figure 7.12.: Evolution of the wall-pressure at $r = 0$ for the $S/R_0 = 1.1$ case and varying crevice sizes R_C/R_0. The time instances shown in Fig. 7.9 are highlighted and labeled with the corresponding row (ii–v). The pressure peaks induced the pressure-wave $p_{\text{PW jet}}$, the collapse p_c and post-collapse wave dynamics p_{post} are indicated as such. The collapse time t_c is plotted as a diamond on the x-axis.

wave patterns.

For $R_C/R_0 = 0.75$ (Fig. 7.11 (c)), the crevice initially suppresses the compression of the lower part of the bubble, resulting in a different shape during jet penetration, at jet impact, and also after compression by the reflected wave (c,ii–v). Furthermore, this increases the collapse time by about 5% when compared to the smooth-wall case.

The pressure signals (Fig. 7.12) show that the pressure wave due to the jet-bubble-impact results in a pressure peak $p_{\text{PW jet}}$ for all configurations. For the small crevice, the pressure wave has to pass a longer distance and thus the peak is smaller. However, the reflection and superposition of the wave at the edge of the crevice results in a more intense peak following ($p_{\text{PW jet reflected}}$).

After the collapse, all three pressure signals exhibit pressure fluctuations with significant peaks that exceed $p_{\text{PW jet}}$. For the large crevice, these peaks are modestly higher than those of the other cases, since the collapse, the rebound and the associated wave dynamics take place closer to the wall. In addition, there are pressure peaks induced by post-collapse wave dynamics for the large crevice.

7.3.6. ASSESSMENT OF CAVITATION EROSION POTENTIAL

The previous sections showed that jet impact, collapse and, in certain configurations, post-collapse wave dynamics induce high pressure peaks in the crevice center. Peak pressures are in the range of 15–80p^*, which corresponds to about 2–12 GPa. These values are in good agreement with the estimated peak pressures for aspherical near-wall collapses (several GPa) (Philipp and Lauterborn, 1998) and spherical bubble collapses (about 12 GPa) (Supponen et al., 2017). Such high peak pressures significantly exceed the strengths of many common engineering materials,

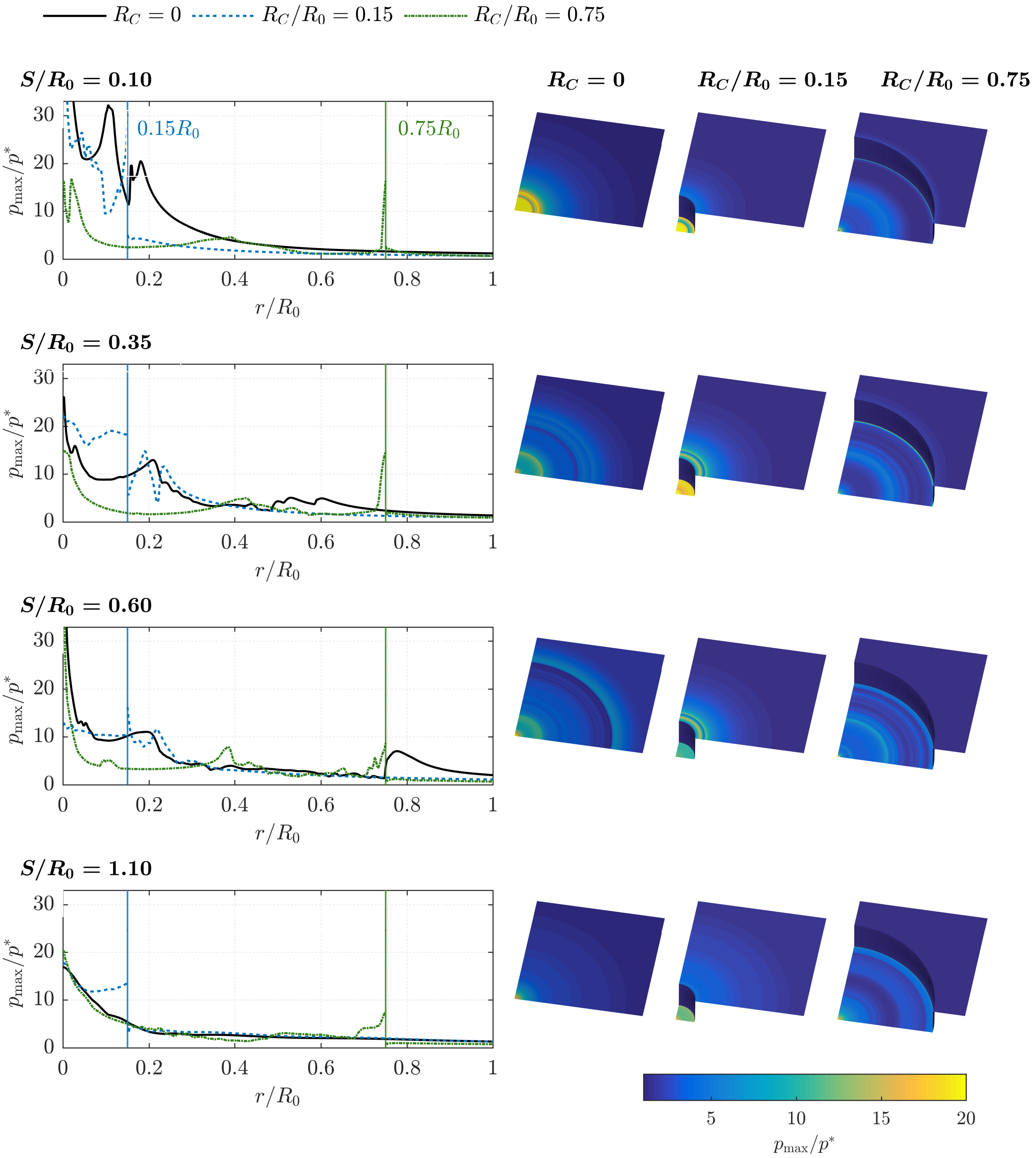

Figure 7.13.: Maximum wall pressure $p_{\max}$ of the entire bubble-collapse process for varying radial locations r with rows corresponding to the stand-off distances S/R_0. First column: $p_{\max}$ over r, where the pressure axes are truncated to promote visibility; the maximum values can be found in the corresponding pressure signals presented in previous sections. Second to fourth column: 3−D visualization of the maximum wall pressure for each crevice size.

such as the 0.55 GPa ultimate tensile strength of stainless steel. Thus, there is potential for significant material erosion. To investigate this, we analyze the spatial distribution of maximum wall pressures.

Figure 7.13 shows the maximum wall pressure $p_{\max}$ at varying radial locations and a visualization of the $p_{\max}$ distribution. First the attached configurations are discussed by crevice size and then the detached ones.

For the smooth wall configurations, there is a collapse-induced peak in $p_{\max}$ at the center with a significant radial decay. In addition, modest pressure peaks are observed at about $r \approx 0.2R_0$, where the torus collapses. This pressure distribution is in agreement with predicted damage patterns by Philipp and Lauterborn (1998), who found ring-shaped damage ($r \approx 0.3R_0$) and a smooth indentation at the wall center.

For the small crevice, significant pressure peaks are induced over the entire crevice bottom. They are especially high at $S/R_0 = 0.35$, where they exceed that of the smooth wall. On the upper wall are peaks at about $r \approx 0.2R_0$ which are related to the torus collapsing at this position (see Fig. 7.7). For the small stand-off distance $S/R_0 = 0.1$ no increased maximum pressures are observed at the upper wall, because the collapse takes place within the crevice.

For the large crevice, the collapse of the detached gas torus results in a modest pressure peak at $r \approx 0.4R_0$, as described in Section 7.3.4. This gas torus is largest for the $S/R_0 = 0.6$ case, and thus leads to highest pressures at this position. The total collapse is in the crevice corner ($r = R_C$) and induces large pressures at this location. Furthermore, at $S/R_0 = 0.1$ two pressure peaks are observed near $r = 0$. The impact of the circular jet results in the off-center peak, while the shock wave after the collapse results in the $r = 0$ maximum pressure.

For all detached-bubble cases, the maximum $p_{\max}$ occurs at $r = 0$, and decays with increasing r apart from a modest increase at $r = R_C$. For the small crevice, there is again a high pressure impact over the entire $r < R_C$ area. Nevertheless, overall the effect of R_C on $p_{\max}$ appears to decrease with increasing S.

For smooth-wall cases, the pressure peaks are most significant at the wall center and cavitation erosion can be expected at this location. For the small crevice cases, a high pressure occurs across the entire crevice bottom, leading to a broader area of possible cavitation erosion. For the large crevice cases, the pressure peaks seen at the crevice corners are also significant, and cavitation erosion is possible at these locations as well.

7.4. CONCLUSION

The collapse of a single gas bubble attached or near a smooth or creviced surface was investigated using high-resolution simulations. Variations of the stand-off distance of the bubble center from the wall and the crevice size were considered. Changing these parameters significantly alters the behavior of the bubble collapse and its associated impact on the wall.

For smooth-wall configurations the final collapse of the bubble results in the maximum wall-pressure, rather than the liquid jet that impinges it. This is in agreement with experimental studies. A similar behavior is observed for smaller crevice sizes, albeit for larger crevices the jet-induced pressures are more significant than the collapse pressures. The presence of the crevice results in a complex collapse process. Reflection and wave superposition result in wave dynamics, which can induce significant post-collapse pressures.

The part of the bubble interface initially in contact with the high-pressure liquid plays an important role in the collapse behavior. The bubble collapse behavior was qualitatively similar for the smooth-wall and small-crevice cases, since the pressure distribution at the interface was comparable. However, large crevices led to a significantly different bubble-liquid interface area, and thus qualitatively different dynamics. The effect of the wall geometry on the collapse behavior and wall pressure was smaller for wall-detached cases.

Lastly, we considered the potential for cavitation erosion. Pressures were recorded over a larger part of the wall. The presence of the small crevice leads to a significant pressure over the entire crevice bottom, as opposed to the smooth-wall cases when largest pressures occurred at the wall center. For all rough configurations, high pressures also occur at the crevice edges, where they induce stresses that can result in material damage.

While assessing the effects of surface topology on hydrodynamics is a necessary step towards understanding this complex process, prediction of actual cavitation erosion also requires investigations of exposed materials. Coupled fluid-material simulations that incorporate suitable material models, and thus also represent elastic and plastic deformation, are one way to accomplish such investigations.

Part III.

CAVITATING NOZZLE FLOWS WITH INJECTION INTO GAS

8. GENERIC STEP NOZZLE - SET-UP AND VALIDATION

We have performed LES of cavitating nozzle flows with injection into gas. The results of this simulation are the basis for Chapters 9 and 10. Here we present the numerical set-up and the validation with experimental data.

This chapter has partially been published in Trummler et al. (2018c,b). Text sections and figures are reprinted with permission from ASME and Begell house. The simulations were conducted by Rahn (2017) during his master's thesis.

8.1. MOTIVATION

The flow field within realistic geometries, such as injector components or control valves, is difficult to access due to limited optical accessibility, small dimensions and complex geometries as well as high velocities and pressures. Therefore, experimental investigations are mostly performed with upscaled transparent nozzles. For the analysis of cavitation dynamics in orifices and control valves, experiments are carried out with injection into liquid (submerged injection) (Sato and Saito, 2002; Saito and Sato, 2003; Sugimoto and Sato, 2009). Cavitation in injector components and the interaction between cavitation and jet break up was investigated by Stanley et al. (2014, 2011); Sou et al. (2007, 2014); He et al. (2016) with injection into gas. Time-resolved numerical simulations are not limited by the above mentioned constraints and provide three-dimensional flow field data to assess the processes in realistic geometries and under real conditions. LES can capture the interaction of cavitation and turbulence, as shown by Egerer et al. (2014). A large number of numerical investigations (Örley et al., 2015; Koukouvinis et al., 2017; Edelbauer, 2017; Biçer and Sou, 2015; Biçer and Sou, 2016) have used the above mentioned reference experiments (Sou et al., 2007, 2014) to validate their modeling approaches and thereby provided deeper insights into the underlying physical processes. Successfully validated models were applied to realistic injector geometries (Örley et al., 2016; Koukouvinis et al., 2017).

As part of this Ph.D. project, we have carried out compressible LES of cavitating nozzle flows emanating into ambient air. Our numerical set-up is based on reference experiments performed by Sou et al. (2014) and Biçer and Sou (2015). The non-dimensional numbers in the experiment - the Reynolds number and the Cavitation number - are in the same range as for typical technical applications. Two operating points covering different cavitation regimes are investigated.

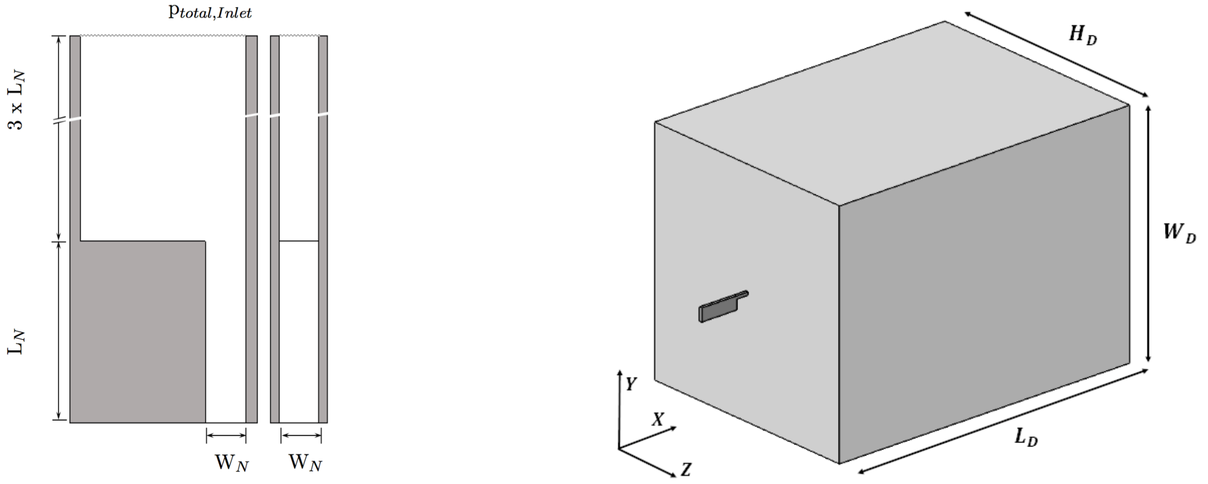

(a) **(b)**

Figure 8.1.: Sketch of the experimental setup. (a) Upstream region and nozzle in top view (left) and side view (right) (b) Full Simulation domain.

8.2. NUMERICAL SET-UP

Our numerical set-up is based on the experiments performed by Sou et al. (2014) and Biçer and Sou (2015). In the experiments, tap water is discharged through a step nozzle into ambient air. Six different operating points were investigated and the cavitation pattern and jet characteristics were visualized with high-speed cameras. Additionally, Laser Doppler Velocimetry (LDV) measurements were conducted for one representative operating point. The investigated operating points are characterized by the cavitation number, which is defined here as:

$$\sigma = \frac{p_{out} - p_{sat}}{0.5\,\rho\,\bar{u}^2}\,. \tag{8.1}$$

p_{out} denotes the pressure at the outlet, p_{sat} the saturation pressure of the liquid, ρ the mean density and $\bar{u}$ the mean velocity in streamwise direction. The tendency for cavitation increases with a lower cavitation number. By changing the flow rate and thus the mean velocity, the cavitation number can be tuned in the experiments. Another important non-dimensional parameter is the Reynolds number

$$Re = \frac{\bar{u}\,W_N}{\nu}, \tag{8.2}$$

which relates the inertial forces to the viscous forces. W_N stands for the width of the nozzle and ν denotes the kinematic viscosity. For the investigated operating points, the Reynolds number Re is in the order of 30,000.

For our numerical studies, we selected two representative operating points: $\sigma = 1.19$ with *developing cavitation* and $\sigma = 0.84$ with *supercavitation*. The numerical set-up is depicted in Fig. 8.1. The geometric measures were taken from the experimental set-up: $L_N = 8\,\text{mm}$ and $W_N = 1.94\,\text{mm}$. The upstream region is elongated to three times the nozzle length, i.e. 24 mm

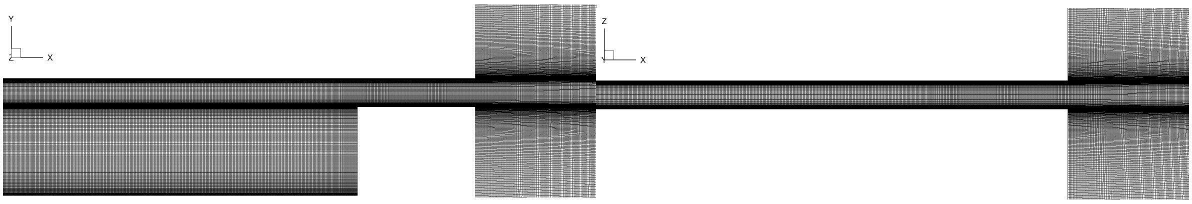

(a) **(b)**

Figure 8.2.: Grid on the finest level (every 4th grid line shown). (a) Top view. (b) Side view.

and to minimize the influence of boundary conditions on the primary jet break-up, a large outlet domain is added, see Fig. 8.1 (b). The following factors with respect to the nozzle dimensions are chosen: $L_D = 25$ x L_N and $W_D = H_D = 75$ x W_N. We discretize the domain using a block-based, structured mesh. A grid sequencing strategy is applied to reduce the computational cost. This means that for each case we let the flow field first develop on a coarse grid and then refine the grid over several refinement steps to the fine grid. For this simulation five different grid levels were used, where the coarsest grid contains 2.4 million cells and the finest 51.5 million cells. In the finest grid, the smallest cell size in wall-normal direction is 2.5 µm and the biggest cells in the nozzle are 30.5 µm long. The grid is also refined around the sharp edge at the nozzle inlet and in the nozzle outflow area where primary jet break-up occurs. Figure 5.4 depicts slices through the grid, showing every fourth grid line.

For the inlet boundary condition we use a total pressure condition as also done by Koukouvinis et al. (2017). The correct pressure for the chosen inlet length is first determined with preliminary simulations and applied later. For $\sigma = 1.19$ we prescribe a total pressure of 2.37×10^5 Pa and for $\sigma = 0.84$ of 3.03×10^5 Pa. At the outlet we define an outlet pressure of $p_{\text{outlet}} = 10^5$ Pa. All walls are treated as viscous isothermal walls. Initially, the whole domain has a pressure of 1×10^5 Pa and a velocity of $u = 0$ m/s. Up to the nozzle outlet, the domain is initialized with liquid only $\xi_g = 0$ and in the outlet region with gas $\xi_g = 1$.

We set the Courant-Friedrichs-Lewy (CFL) to 1.4, resulting in a time step of approximately 0.7×10^{-9} s on the finest grid. Statistical averaging on the finest grid was performed over 4 ms, sampling every time step. The analyzing time of 4 ms corresponds to roughly 6 flow-through times, depending on the operating point. Mass flow and average velocity at the nozzle inlet and the outlet were monitored during the simulations. Additionally, the integral vapor content in the nozzle was monitored.

Figure 8.3 shows the dimensionless wall-normal resolution y^+ for the case $\sigma = 1.19$. y^+ is the ratio of the wall-normal distance of the first grid point to the viscous length scale δ_ν:

$$y^+ = \frac{y}{\delta_\nu} \text{ with } \delta_\nu = \frac{\nu}{u_\tau} = \frac{\nu}{\sqrt{\tau_W/\rho}} \,. \tag{8.3}$$

The near-wall resolution in the nozzle is $y = 2.5$ µm. δ_ν is calculated using time-averaged data, where ν stands for the average kinematic viscosity and u_τ for the friction velocity. u_τ is the square root of the time-averaged ratio of the wall shear stress τ_W over the density ρ. As shown in Fig. 8.3, y^+ in the nozzle is around 1. This indicates that the first grid points lie within the viscous sublayer. Additionally, the chosen grid resolution is motivated by the simulations

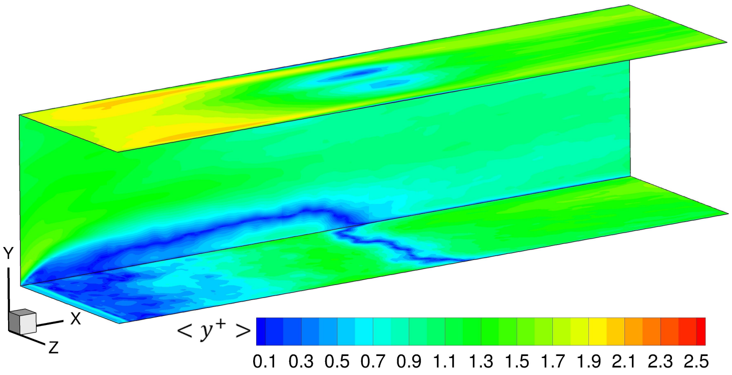

Figure 8.3.: Averaged y^+ for $\sigma = 1.19$.

conducted by Örley et al. (2015) for a similar configuration with slightly higher velocities, where they proved grid convergence for a near-wall grid resolution of 3.9 µm. Koukouvinis et al. (2017) demonstrated grid convergence for the same reference case with an identical near-wall resolution of 2.5 µm.

In this chapter and the two subsequent ones, the computational results obtained at the finest grid level are presented and discussed. In the next section, the simulation method is validated against experimental data.

8.3. COMPARISON WITH EXPERIMENTAL DATA AND VALIDATION

In the reference experiment conducted by Sou et al. (2014), light transmission images of the cavitation in the nozzle and the jet were taken. Figure 8.4 compares these with our numerical results. In general, there is a good agreement of the cavitation pattern and the jet characteristics.

For the higher cavitation number $\sigma = 1.19$ the experiment predicted *developing cavitation*. In agreement with the experiment, we observe vapor structures in the first part of the nozzle while the jet is not affected by cavitation. For $\sigma = 0.84$ the cavitation has increased significantly, and the vapor region is spanning from the nozzle inlet up to shortly before the nozzle outlet. In this *supercavitation* regime, the vapor structures collapse close to the nozzle outlet and the experiments showed that an enhanced jet break-up occurs. Our simulation results reproduce this effect. The specification of constant total pressure at the inlet results at this operating point in a slightly different average velocity (15.2 m/s instead of 15.4 m/s) and thus in a slightly higher cavitation number.

In the experiment, Sou et al. (2014) performed LDV measurements for $\sigma = 1.19$ and determined the mean streamwise velocity and the fluctuations in the nozzle. They evaluated the flow field at three different positions, marked in the sketch in Fig. 8.5, in streamwise direction. To validate our numerical method, Fig. 8.5 compares our results with the experimental data and other numerical results. For comparison, the results from Sou et al. (2014) with the Smagorinsky model and from Koukouvinis et al. (2017) with the wall-adapting local eddy-viscosity model (WALE) in combination with a barotropic cavitation model are added to the figure. In the upper row of

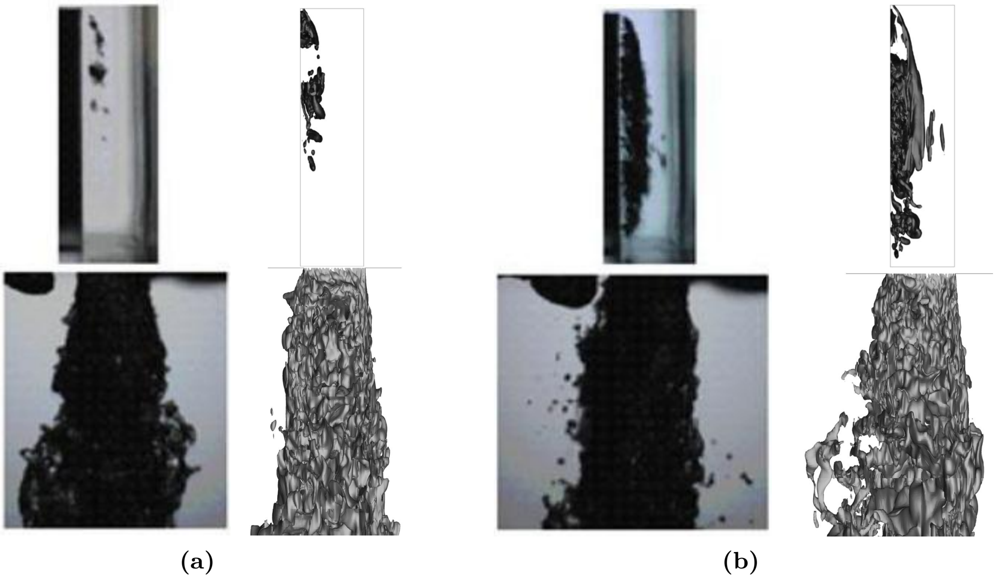

Figure 8.4.: Comparison of the experimental data from Sou et al. (2014) and the simulation results. Isosurfaces: Vapor: $\alpha = 0.1$ and jet surface: $\beta_g = 0.75$. (a) $\sigma = 1.19$ (b) $\sigma = 0.84$ ($\sigma_{\text{Experiment}} = 0.83$). Experimental data are reprinted from Sou et al. (2014) with permission of Elsevier.

Fig. 8.5 the mean streamwise velocity is plotted against the horizontal position. These profiles can be well reproduced with our simulation. Only the detached flow region is slightly wider in the experiment, especially at the position $x = 3\,\text{mm}$. Our results are close to the numerical ones obtained by Koukouvinis et al. (2017).

The fluctuations in streamwise direction are compared in the bottom row of Fig. 8.5. A clear maximum of the fluctuations is visible in the region of the cavity around $y = 0.4\,\text{mm}$ at the positions $x = 1.5$ and $3\,\text{mm}$. Within the cavitation zone ($y < 0.4\,\text{mm}$) the fluctuations are higher than in the main flow field. Our simulation and the numerical findings by Koukouvinis et al. (2017) overestimate fluctuations compared to the experiment. This may be related to the measurement method since LDV measurements employ tracing of passive particles. Due to inertia effects the particles mostly remain in the liquid phase, which affects the results of this measurement method. In the main flow field, there is an excellent agreement of the fluctuations in our simulation and the experiment. At the right wall (max y) the fluctuations increase again.

8.4. SUMMARY

We have performed implicit LES at two operating points covering the regimes of *developing cavitation* and *supercavitation* using a fully compressible multi-component model. The set-up is adapted from an experiment where tap water is discharged through a large-scale nozzle into air.

Overall, there is a good agreement of the simulation results with experimental data, which demonstrates the applicability of our numerical method and thermodynamic modeling for the

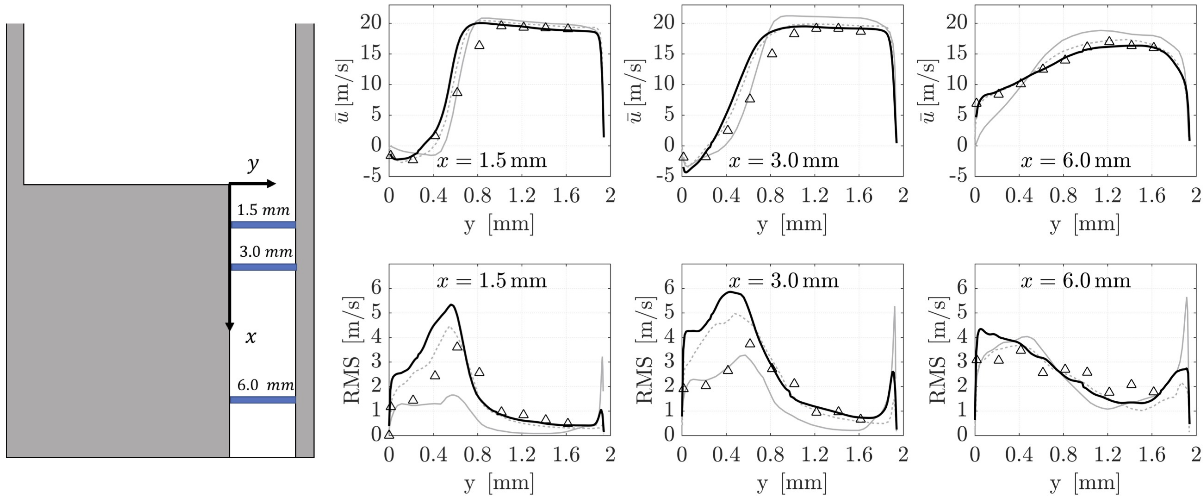

Figure 8.5.: Comparison of the experimental data from Sou et al. (2014) (triangles) and the numerical results from our simulations (—)(black, solid); from Sou et al. (2014) (—)(gray, solid) and from Koukouvinis et al. (2017)(- - -)(gray, dashed). Top: Mean streamwise velocity at different positions in the nozzle. Bottom: RMS (root mean square) of the fluctuations of the velocity in streamwise direction at different positions in the nozzle.

investigated flows. In the following chapters, these simulation results are analyzed in detail regarding the cavitation dynamics and shedding mechanisms (Chapter 9) and the effects of cavitation and gas entrainment on the mass flow and the jet characteristics (Chapter 10).

9. CAVITATION DYNAMICS AND SHEDDING MECHANISMS

This chapter provides a comprehensive analysis of cavitation dynamics in internal nozzle flows with constant cross-section and discharge into ambient gas. We analyze cavitation dynamics and the initiating shedding mechanisms. Based on our results, we propose modifications to schematics of the cloud shedding process (Stanley et al., 2014; Le et al., 1993). Moreover, we evaluate the near-wall flow field and investigate mechanisms for re-entrant jet formation.

This chapter is based on the publication Trummler et al. (2020b). Figures, tables and text sections are reprinted with permission of Elsevier.

9.1. MOTIVATION

Cloud cavitation is a form of partial cavitation where vapor clouds periodically shed from the main cavity (Reisman et al., 1998; Laberteaux and Ceccio, 2001). This form of cavitation occurs in flows around bodies, such as hydrofoils (Le et al., 1993; Kubota et al., 1989; De Lange and De Bruin, 1998), and in internal flows, e.g. Venturi nozzles (Rudolf et al., 2014; Hayashi and Sato, 2014), converging-diverging ducts with a rectangular cross-section (wedges) (Stutz and Reboud, 1997; Ganesh et al., 2016), and other types of orifices and nozzles (Stanley et al., 2014, 2011; Sato and Saito, 2002; Saito and Sato, 2003; Sugimoto and Sato, 2009; Sou et al., 2007; He et al., 2016). The periodic cloud shedding process is initiated by the upstream motion of a disturbance, which can be either a thin liquid film underneath the cavity (*re-entrant jet*) or a bubbly *condensation shock*.

A re-entrant jet characterizes the motion of a liquid jet underneath the fixed cavity in upstream direction and is generally considered to initiate the shedding process. Le et al. (1993) proposed a schematic description for the periodic cloud shedding process on hydrofoils, which Stanley et al. (2014) adapted for internal nozzle flows. Figure 9.1 depicts this schematic. After the collapse of a shed cloud, a re-entrant jet develops at the end of the cavity and travels upstream underneath the cavity. When the re-entrant jet has covered the entire cavity and reached the inception point of the cavity, the cavity is shed and a new one begins to form (Le et al., 1993; Wade and Acosta, 1966). The shed cloud convects downstream with the flow, in a rolling motion (Le et al., 1993; Kubota et al., 1989). In the region of increased pressure downstream the shed cloud collapses, emitting an intense shock wave leading to pressure peaks orders of magnitude larger than the pressure in the mean flow (Reisman and Brennen, 1996; Reisman et al., 1998), which can cause cavitation erosion (Gopalan and Katz, 2000; Petkovšek and Dular, 2013). Moreover, these cavitation induced pressure fluctuations (Leroux et al., 2004; Ji et al., 2015) are also considered

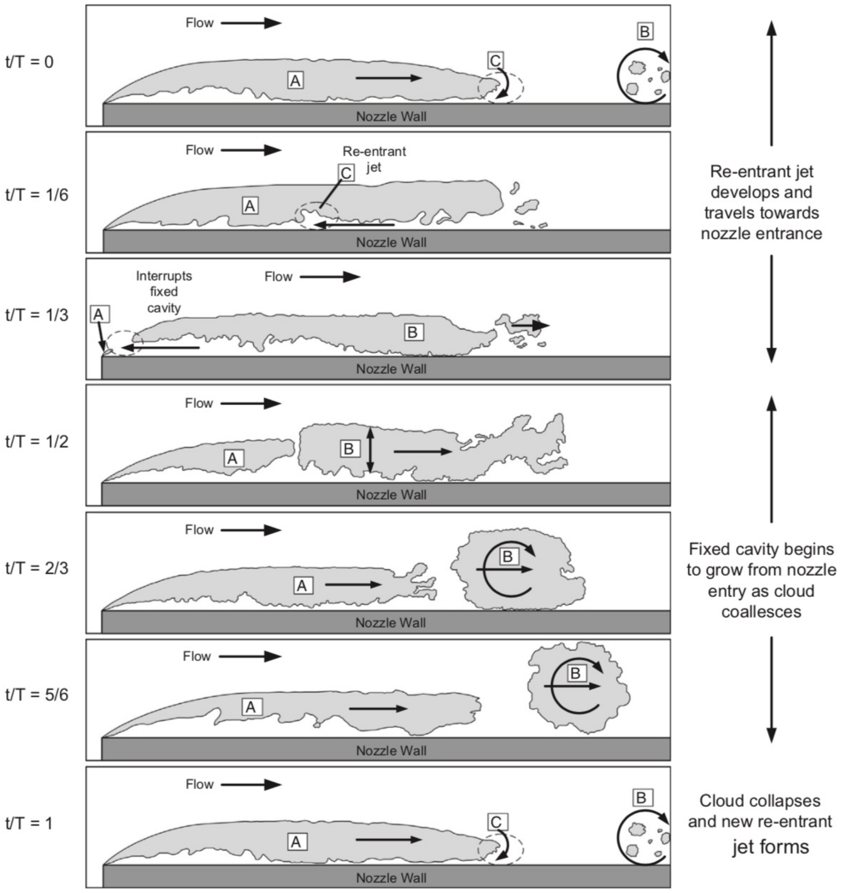
t/T = 0
t/T = 1/6
t/T = 1/3
t/T = 1/2
t/T = 2/3
t/T = 5/6
t/T = 1
Flow
Nozzle Wall
A
B
C
Re-entrant jet
Interrupts fixed cavity
Re-entrant jet develops and travels towards nozzle entrance
Fixed cavity begins to grow from nozzle entry as cloud coallesces
Cloud collapses and new re-entrant jet forms

Figure 9.1.: Schematic illustration of typical re-entrant jet motion proposed by Stanley et al. (2014), which is adapted and modified from Le et al. (1993). The nozzle orientation is horizontal. Annotations: A–C identify the fixed cavity, bubble cloud and re-entrant jet respectively where an apostrophe implies a new structure; vapor appears gray. Reprinted from Stanley et al. (2014) with permission from Elsevier.

to contribute to the formation of the re-entrant jet, as discussed below.

Although many experimental and numerical studies have investigated re-entrant jets and their decisive role in cloud shedding (e.g. Kawanami et al. (1997); Lush and Skipp (1986); Gopalan and Katz (2000); Furness and Hutton (1975)), the driving mechanism behind the formation of the jet has not yet been clarified. One theory is that the re-entrant jet is formed due to the stagnation point behind the cavity (at the closure), where the flow surrounding the cavity impinges on the wall. Another suggestion is that the pressure peaks due to the collapse of shed clouds promote the motion of the re-entrant jet (Leroux et al., 2004, 2005). Coutier-Delgosha et al. (2007), however, found no general relation between the shock waves after cloud collapse and the re-entrant jet motion. Callenaere et al. (2001) consider the cavity thickness in relation to the re-entrant jet thickness and the negative pressure gradient to be the two most relevant parameters for the instability of the re-entrant jet.

Several experimental investigations have assessed the velocity of re-entrant jets. For the cavitating flow on a hydrofoil, Pham et al. (1999) measured that the re-entrant jet velocity at the end of the cavity is about the free stream velocity and decreases upstream. Decreasing upstream jet velocity was also observed by Sakoda et al. (2001). Le et al. (1993) found that the velocity of perturbations traveling upstream is close to the magnitude of the free stream flow. Stanley et al. (2014) tracked bubbles in the liquid film underneath the cavity and obtained velocities of 20 - 30% of the free-stream velocity, which is a smaller magnitude than reported in previous findings.

In addition to re-entrant jets, condensation shocks can also initiate periodic cloud shedding. The occurrence of condensation shocks was predicted back in 1964 by Jakobsen (1964). Later, condensation shocks on hydrofoils have been studied experimentally by e.g. Reisman et al. (1998); Arndt et al. (2001). Converging-diverging geometries have been investigated experimentally by Ganesh et al. (2016); Jahangir et al. (2018); Wu et al. (2017); Wang et al. (2017) and recently by compressible numerical simulations (Budich et al., 2018). For shock initiated shedding, one observes an upstream moving bubbly shock rather than a re-entrant jet. The formation of bubbly shocks is more likely when the cavitation number decreases, and for an increased void fraction in the cavity (Ganesh et al., 2016). We are not aware of publications addressing the occurrence of condensation shocks in nozzles with constant cross-sections. However, the observations by Stanley et al. (2014) may be explained by a condensation shock mechanism.

In Sections 9.2 and 9.3, we analyze the cavitation dynamics of the two investigated operating points. Following Stanley et al. (2014), we define the beginning of a cycle by the collapse of the previously shed cloud. Afterwards, we scrutinize the shedding processes in Section 9.5 and propose modifications to schematics of the cloud shedding process from the literature for the different shedding mechanisms in Section 9.5. In the end, in Section 9.6, we analyze the upstream-flow and its potential driving mechanisms.

9.2. DEVELOPING CAVITATION AND MAINLY RE-ENTRANT JET INITIATED SHEDDING ($\sigma = 1.19$)

A time series of three shedding cycles depicting instantaneous vapor structures as well as the flow field in a side and a top view is shown in Fig. 9.3. The corresponding temporal evolution of the vapor content in the nozzle is shown in Fig. 9.2. The dominant frequency of the integral vapor content based on spectral (Fourier) analysis of the data is $f = 1110\,\mathrm{Hz}$ (see Chapter 10), which corresponds to a period of $T = 0.9\,\mathrm{ms}$.

At the beginning of each shedding cycle, we observe a single cavity near the nozzle inlet, slightly shifted downstream. The shear layer at the inlet edge contains only a thin vapor sheet. In the middle of each cycle, a vapor cloud is shed and convected downstream, which manifests itself as rolling, cavitating horseshoe vortex, see e.g. fourth column of Fig. 9.3. Corresponding experimental observations are given in Kubota et al. (1989). These detached, rolling vortices move faster than the main cavity grows, which can be clearly seen from the different trajectories in Fig. 9.3 (e.g. $t = 2.2 - 2.7\,\mathrm{ms}$). The structures become smaller as they move downstream and their velocity increases. These observations agree with experimental findings by Kubota et al. (1989); Sato and Saito (2002). Furthermore, we observe streamwise cavitating vortices (e.g.

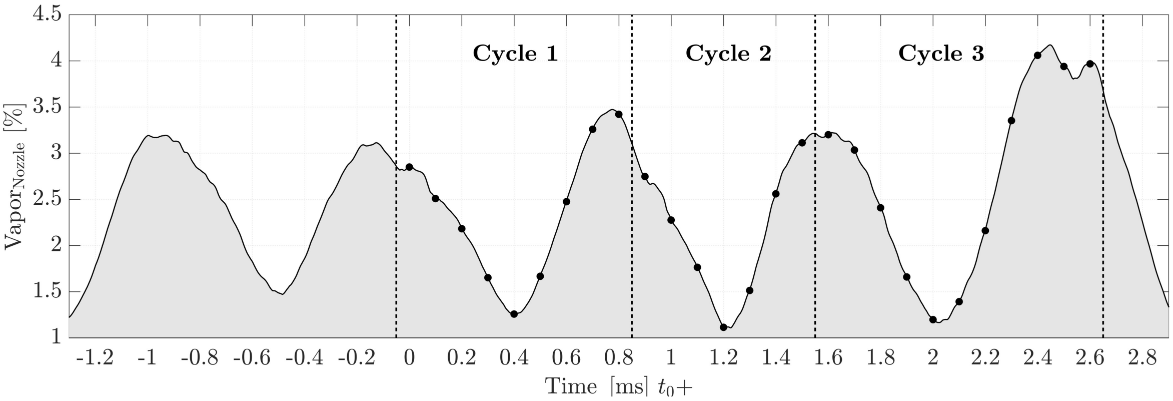

Figure 9.2.: Vapor content over time for $\sigma = 1.19$; time steps shown in Fig. 9.3 are marked with a dot.

$t = 0.6\,\text{ms}$, $t = 0.7\,\text{ms}$, $t = 2.4\,\text{ms}$). At certain time steps, these connect the main cavity with the detached structure. Saito and Sato (2003) reported similar observations.

After the shedding, a new main cavity forms (black dashed line in Fig. 9.3), and gains vapor volume by shear layer cavitation. Cavitating spanwise vortices form in the shear layer and later coalesce in a rolling motion (e.g. $t = 0.4-0.5\,\text{ms}$ and $t = 1.3-1.4\,\text{ms}$). Such a pairing of spanwise structures in a rolling motion was also observed in experiments (Saito and Sato, 2003; Sato and Saito, 2002).

The vapor sheet is not a coherent vapor cavity, as often shown schematically (Le et al., 1993; Callenaere et al., 2001; Franc and Michel, 2005), but is a two-phase mixture of vapor bubbles and liquid, which also has been observed in experimental investigations (Stanley et al., 2014; Kubota et al., 1989). Furthermore, in most cases the vapor sheet is not attached to the nozzle wall but separated from the wall by a liquid film with an upstream velocity, as also reported by Stanley et al. (2014, 2011).

The shedding during the first two cycles depicted in Fig. 9.3 is caused by a re-entrant jet, whereas in the last cycle it is due to a condensation shock. During the first two cycles, a thin, coherent, upstream moving liquid film at the end of the sheet can be seen over the first half of the cycle, which agrees with existing schematics of the cloud shedding process (Stanley et al., 2014; Le et al., 1993) depicting a re-entrant jet motion over the first third of a cycle. The jet motion continues upstream and initiates a shedding in the middle of the cycle. An upstream flow underneath the cavity is present during the entire cycle since in the second half of each cycle, the rolling motion of detached vapor structures induces an upstream flow.

During the third cycle, near wall liquid layers are not observed and the vapor reaches down to the wall, i.e. the cavity is attached, which apparently triggers the condensation shock observed during this cycle. Moving upstream the shock increases in height and eventually spans over the entire cavity height (see $t = 1.9\,\text{ms}$, $t = 2.0\,\text{ms}$).

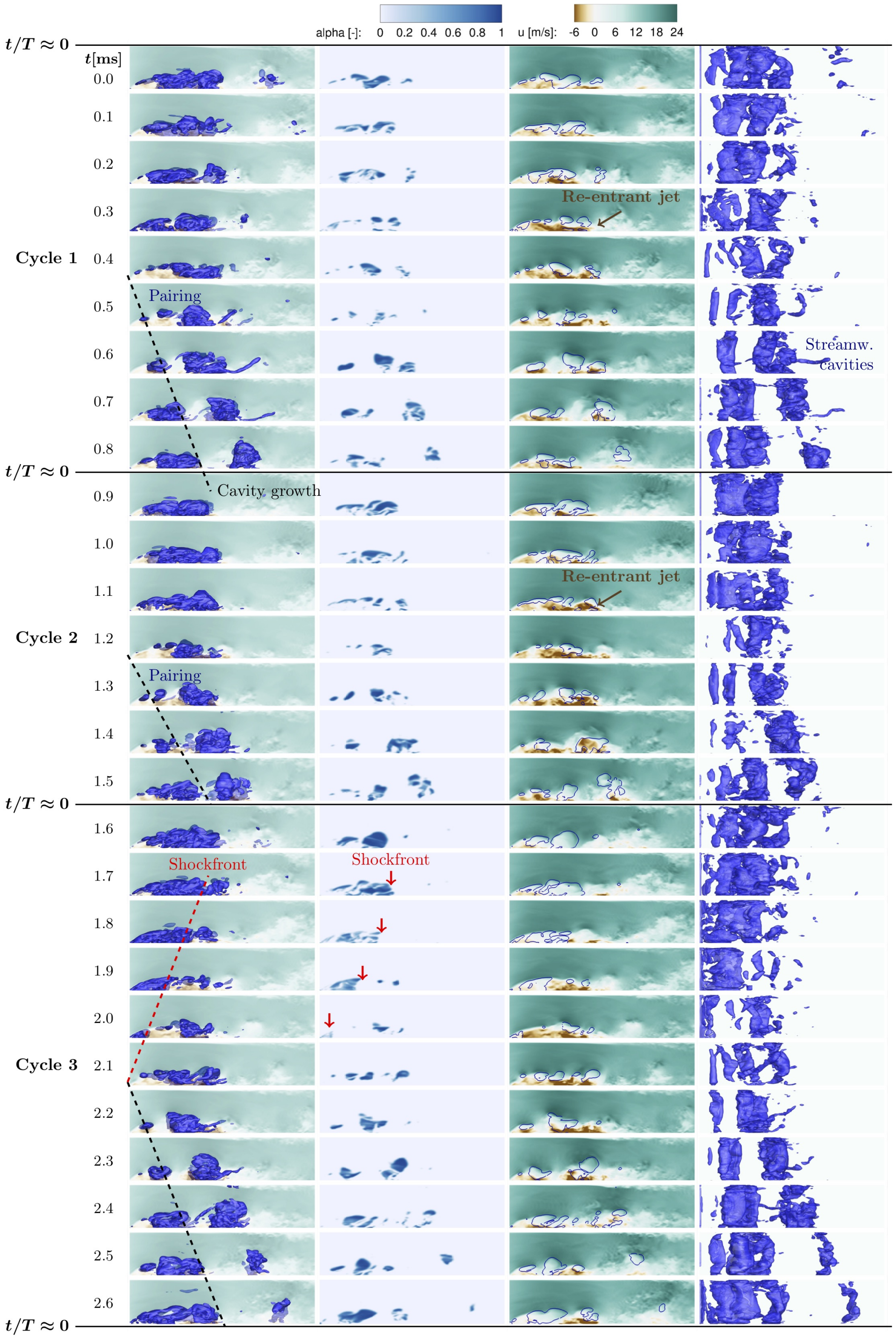

Figure 9.3.: Time series for $\sigma = 1.19$, time step $\Delta t = 0.1$ ms, time increases from top to bottom. First to third column: side view of the midplane flow field; fourth column: top view. First column: streamwise velocity and isosurface vapor; second: vapor; third: streamwise velocity and isoline vapor; fourth: isosurface vapor. Blue isosurface or isoline 10% vapor, black dashed line indicates the cavity growth and the red dashed one the upstream moving shock front.

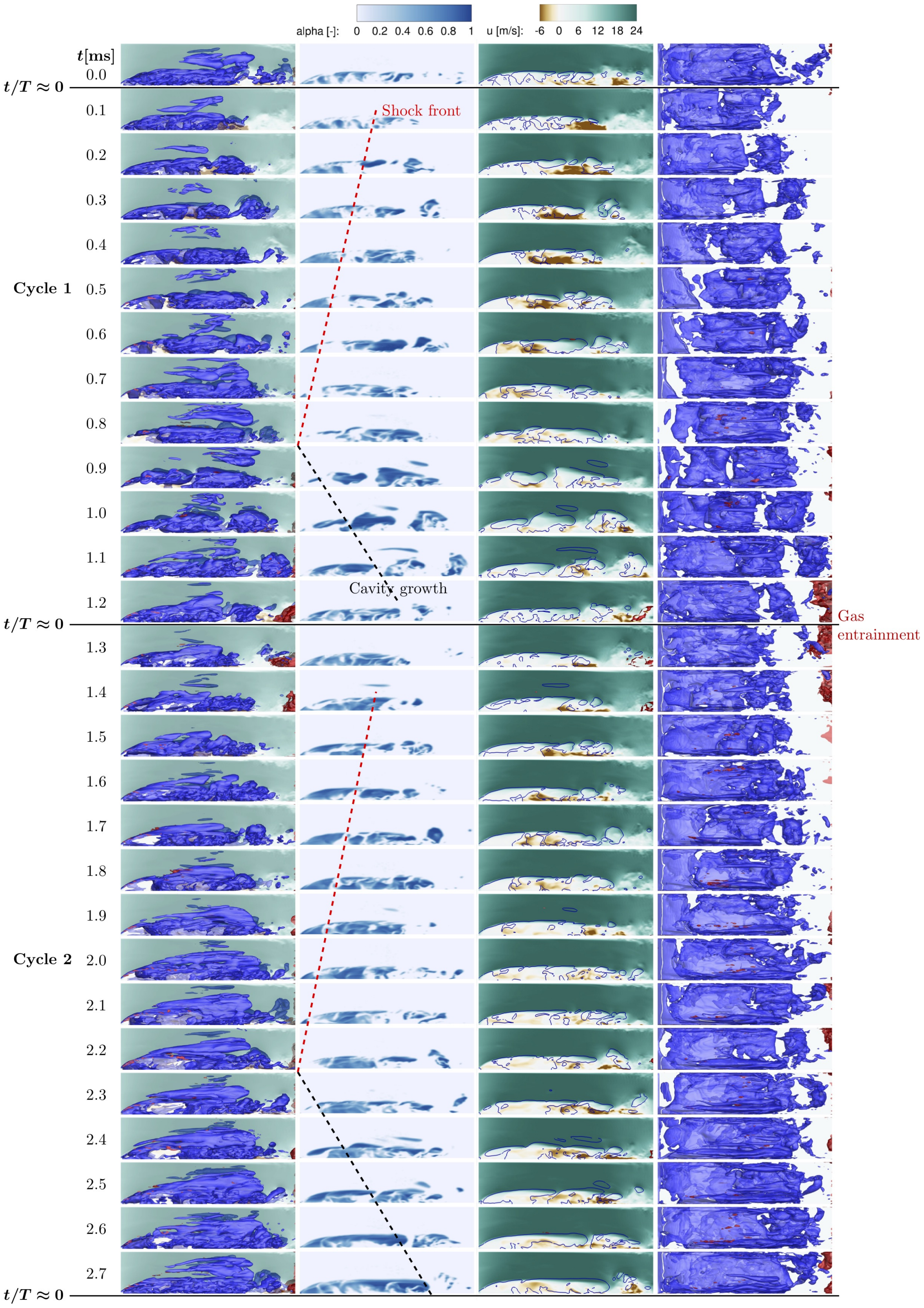
alpha [-]: 0 0.2 0.4 0.6 0.8 1
u [m/s]: -6 0 6 12 18 24
t[ms]
0.0
t/T ≈ 0
0.1
0.2
0.3
0.4
Cycle 1
0.5
0.6
0.7
0.8
0.9
1.0
1.1
1.2
t/T ≈ 0
1.3
1.4
1.5
1.6
1.7
1.8
1.9
Cycle 2
2.0
2.1
2.2
2.3
2.4
2.5
2.6
2.7
t/T ≈ 0
Shock front
Cavity growth
Gas entrainment

Figure 9.4.: Time series for $\sigma = 0.84$, time step $\Delta t = 0.1$ ms, time increases from top to bottom. First to third column: side view of the midplane flow field; fourth column: top view. First column: streamwise velocity and isosurfaces vapor and gas; second: vapor; third: streamwise velocity and isoline vapor; fourth: isosurfaces vapor and gas. Blue isosurface or isoline 10% vapor, red isosurface 10% gas, black dashed line indicates the cavity growth and red dashed one the upstream moving shock front.

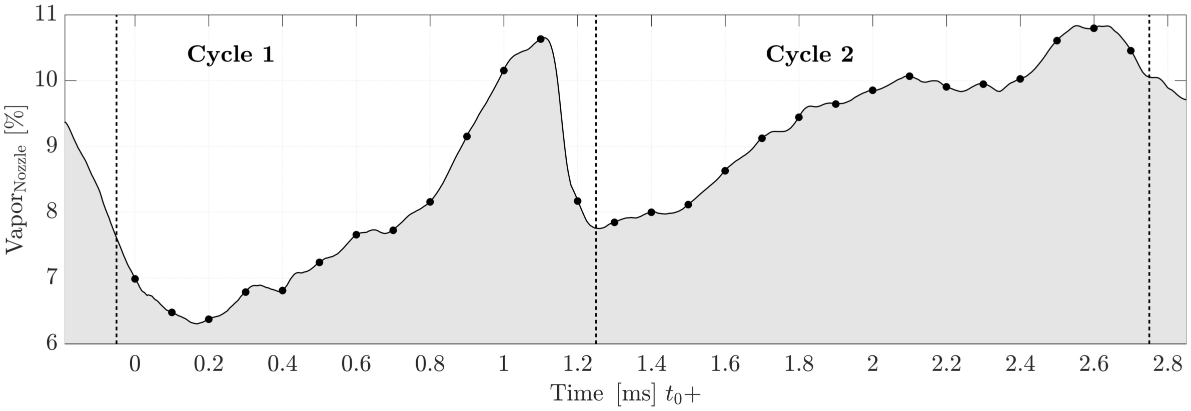

Figure 9.5.: Vapor content over time for $\sigma = 0.84$; time steps shown in Fig. 9.4 are marked with a dot.

9.3. SUPERCAVITATION AND CONDENSATION SHOCK INITIATED SHEDDING ($\sigma = 0.84$)

Figure 9.4 shows a time series covering two shedding cycles. At this operating point, partial gas entrainment occurs. The red isosurface indicates a local gas content of $\geq 10\%$. Figure 9.5 depicts the corresponding temporal evolution of the integral vapor content. The vapor content has increased significantly and does not drop as much as for $\sigma = 1.19$. We do not observe a well-defined periodic shedding as for $\sigma = 1.19$ and the dominant frequency decreases compared to $\sigma = 1.19$, both observations also reported from experimental investigations (Stanley et al., 2011). The dominant frequency found by spectral analysis is $f = 750\,\text{Hz}$, which corresponds to $T = 1.33\,\text{ms}$. The decreasing shedding frequency with increasing cavitation is consistent with observations by experimental studies (Stanley et al., 2011; Ganesh, 2015; Ganesh et al., 2016).

Streamwise vortices in the center of the nozzle can be observed at some time instants, which also have been observed in experiments (Mauger et al., 2012) and numerical simulations (Egerer et al., 2014); the latter reference discusses the underlying mechanisms leading to the formation of these vortices.

At the beginning of the shedding cycle, a vapor sheet spans from the inlet edge to about 3/4 of the nozzle length. At the end of the sheet, a liquid flow with a comparably high velocity in the upstream direction is visible, similar to the observations and the schematic description by Stanley et al. (2014). During the first half of the shedding cycle, smaller structures at the end of the sheet detach, are convected downstream and then collapse. Due to the detachment of these smaller structures, the cavity length is approximately constant throughout the cycle. The small detached structures are rolling, cavitating spanwise vortices. Occasionally, connecting streamwise vortices are visible, as in $t = 0.3\,\text{ms}$ or in $t = 1.7\,\text{ms}$. The re-entrant jet formed at the beginning of each cycle later transforms into a condensation shock. While the upstream moving shock leads to the condensation of the front part of the cavity, the rear part is further fed by shear layer cavitation. The complete condensation of the front part causes the detachment of the remaining rear part, see e.g. $t = 0.8\,\text{ms}$. This part is then convected further downstream and reshapes

Table 9.1.: Strouhal number (*Str*), temporal partitioning ($\lambda_{T,\phi}$) and relative velocities ($\lambda_{U,\phi}$) with $\phi = \{G, D\}$ where G is growth and D deformation. 'Slope' refers to the lines in the time series (Figs. 9.3 and 9.4).

σ [-]	$\bar{u}$ [m/s]	f [Hz]	l_{cav} [mm]	Str [-]	$\lambda_{\mathrm{T,G}}$ [-]	$\lambda_{\mathrm{u,G}}$ [-]	$\lambda^{\mathrm{slope}}_{\mathrm{u,G}}$ [-]	$\lambda_{\mathrm{T,D}}$ [-]	$\lambda_{\mathrm{u,D}}$ [-]	$\lambda^{\mathrm{slope}}_{\mathrm{u,D-SF}}$ [-]
1.19	12.8	1110	3.6	0.31	1/2	0.62	0.53	1/2	0.62	0.7
0.84	15.2	750	5.8	0.29	1/3	0.87	0.86	2/3	0.44	0.33

into two vapor clouds ($t = 0.9 - 1.2\,\mathrm{ms}$) rotating towards the nozzle outlet. The cloud further downstream reaches the outlet and leads there to gas entrainment into the nozzle ($t = 1.2\,\mathrm{ms}$, red isosurfaces). Shortly afterwards ($t = 1.3 - 1.4\,\mathrm{ms}$), the gas is pushed back out. However, a certain amount of gas remains in the nozzle and expands later in the low-pressure vapor region forming small gas-filled structures, see e.g. $t = 1.7\,\mathrm{ms}$ and $1.8\,\mathrm{ms}$. The second cloud collapses close to the main cavity ($t = 1.2\,\mathrm{ms}$, $t = 1.3\,\mathrm{ms}$), and after its collapse a thin upstream liquid flow at the end of the cavity can be seen. For the second cycle, we also observe a shedding, though not visible as clearly as in the first cycle depicted, and the volume of the shed cloud is smaller.

9.4. CHARACTERIZATION OF THE SHEDDING PROCESSES

The shedding at $\sigma = 1.19$ is mainly caused by re-entrant jet motion whereas at $\sigma = 0.84$ condensation shocks are predominant. The dominance of condensation shocks for the lower cavitation number is in accordance with experimental investigations (Jahangir et al., 2018; Arndt et al., 2001). E.g. Jahangir et al. (2018) determined that for a convergent, divergent nozzle the shedding is shock dominated for $\sigma < 0.75$. The comparison to our results indicates that for our nozzle geometry the limits are shifted to higher cavitation numbers, which may result from a stronger blocking effect due to the constant cross-section. Ganesh (2015) found that the formation of condensation shocks is favored at increased void fractions.

The dimensionless Strouhal number for shedding processes is

$$Str = f \cdot l_{\mathrm{cav}} / \bar{u}, \tag{9.1}$$

where l_{cav} the length of the main cavity, here evaluated in the time series. The values obtained are $Str \approx 0.3$ (see Table 9.1) and compare well with experimental values for cylindrical orifices with $Str = 0.3 - 0.5$ (Stanley et al., 2011; Sato and Saito, 2002; Sugimoto and Sato, 2009).

As can be seen in the time series (Figs. 9.3 and 9.4), shedding cycles can be divided into the upstream motion of a disturbance ($\phi = D$), which is either a re-entrant jet (RJ) or a condensation shock (CS), and the growth phase of the main cavity ($\phi = G$) with the temporal partitioning of

$$\lambda_{T,\phi} = t_\phi / T \quad \text{and} \quad \sum_\phi \lambda_{T,\phi} = 1 \tag{9.2}$$

where t_ϕ stands for the time the process $\phi = \{D, G\}$ takes. We observe for the re-entrant jet governed cycles at $\sigma = 1.19$ a duration of about half a period for each process and thus

$\lambda_{T,G} = \lambda_{T,D-RJ} = 1/2$ (see Fig. 9.3). Our $\lambda_{T,D-RJ}$ is slightly higher than reported in the literature as Le et al. (1993) proposed $\lambda_{T,D-RJ} = 1/3$ and Callenaere et al. (2001) found $\lambda_{T,D-RJ} \approx 0.40$ and a length of $\lambda_{L,D-RJ} = 0.75$. For the shock governed regime, the motion of the disturbance is slower and takes about $\lambda_{T,D-SF} = 2/3$ (see Fig. 9.4). A dependency of the temporal partitioning on the governing shedding mechanism can also be seen in the time series in Fig. 9.3, where the last cycle, with the condensation shock, is significantly longer than the previous ones. In the data provided by Budich et al. (2018) for a condensation shock governed shedding of a cavitating flow over a wedge, the velocity ratios are $|u_G/u_{D-SF}| = 1.22$ which implies that $\lambda_{T,G} < \lambda_{T,D-SF}$ and confirms our observation.

The velocity ($u_\phi = \lambda_{U,\phi}\,\bar{u}$) of each process is the ratio of the length l_ϕ, which can be expressed as $l_\phi = \lambda_{L,\phi}\,l_{cav}$, to the time t_ϕ as

$$u_\phi = \frac{l_\phi}{t_\phi} = \frac{\lambda_{L,\phi}\,l_{cav}}{\lambda_{T,\phi}\,T}, \tag{9.3}$$

with $\lambda_{L,\phi} \approx 1$ and Eq. (9.1) we obtain for the dimensionless velocity

$$\lambda_{u,\phi} \approx \frac{Str}{\lambda_{T,\phi}}. \tag{9.4}$$

Table 9.1 compares the velocities estimated using Eq. (9.4), which represent time-averaged values, and the ones obtained by the mean slope of the lines tracing the cavity end and the shock front in the time series (Figs. 9.3 and 9.4). The agreement of these values shows that Eq. (9.4) provides a good estimate. Furthermore, the velocities determined and estimated for the disturbance $\lambda_{U,D}$, $\lambda_{U,D}^{\text{slope}}$ are in accordance with the data from the literature. For re-entrant jets, values of approximately 0.5 $\bar{u}$ (e.g. Pham et al. (1999); Callenaere et al. (2001)) are given, which is within the range of our results. Detailed analyses follow in section Section 9.6. For the shock front velocities values of 35 – 60% of the free flow velocity are reported by Ganesh (2015) for cavitating flows over a wedge. For a cavitating nozzle flow, Stanley et al. (2014) observed an upstream moving deformation at the interface of the lower cavity at a velocity of 30 – 80% $\bar{u}$ for the range of our cavitation numbers. Both ranges of the shock front velocity agree to our results of $\lambda_{U,D-SF}^{\text{slope}} = 0.33 - 0.7$, see Table 9.1.

9.5. SCHEMATICS OF THE CLOUD SHEDDING PROCESS

Based on the previous observations we have adapted existing schematics of the cloud shedding process (Stanley et al., 2014; Le et al., 1993) as shown in Fig. 9.6 and propose modifications depending on the governing shedding mechanism.

For the re-entrant jet initiated shedding at the developing cavitation, an upstream motion of a liquid jet is present during the first half of a cycle. In the middle of the shedding cycle, a vapor cloud is shed and convected downstream as a rolling horseshoe vortex. The growth of the new main cavity is due to shear layer cavitation and paring and coalescence of the formed spanwise vortices. An upstream, liquid, near-wall flow is present throughout the cycle - first due to the re-entrant jet motion and later due to the rolling motion of the detached structures.

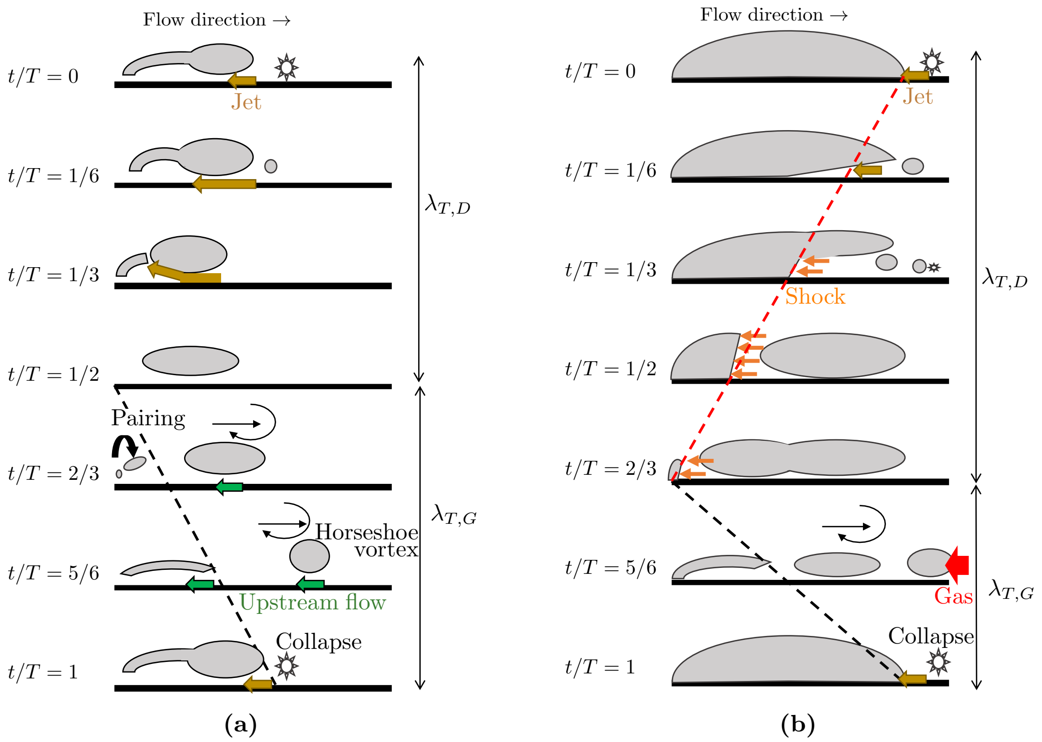
Flow direction →
t/T = 0
Jet
t/T = 1/6
t/T = 1/3
t/T = 1/2
$\lambda_{T,D}$
Pairing
t/T = 2/3
$\lambda_{T,G}$
Horseshoe vortex
t/T = 5/6
Upstream flow
Collapse
t/T = 1
Flow direction →
t/T = 0
Jet
t/T = 1/6
t/T = 1/3
Shock
$\lambda_{T,D}$
t/T = 1/2
t/T = 2/3
t/T = 5/6
Gas
$\lambda_{T,G}$
Collapse
t/T = 1

(a) **(b)**

Figure 9.6.: Schematics of cloud shedding processes adapted and modified from those proposed by Stanley et al. (2014) and Le et al. (1993) for re-entrant jet governed cloud shedding. (a) developing cavitation with re-entrant jet initiated shedding (b) supercavitation with condensation shock initiated shedding. Flow direction is from left to right; vapor appears gray.

In case of a shock initiated shedding, the vapor sheet is attached to the nozzle wall. At the beginning of a cycle, a re-entrant jet forms at the end of the sheet and moves upstream transforming into a condensation shock. Here the temporal partitioning into the convection of the disturbance is longer than for the re-entrant jet initiated shedding, as also discussed above. The condensation of the upstream part leads to the detachment of the rear part. In this cavitation regime, detached vapor clouds reaching the nozzle outlet can lead to gas entrainment. In this study, the gas entrainment affects only the flow field directly at the nozzle outlet, and we did not observe a direct impact on cavitation dynamics and shedding.

9.6. NEAR-WALL UPSTREAM FLOW

We analyze the near-wall upstream flow using x-t diagrams in which the flow field on the midplane close to the wall is extracted and arranged with increasing time, see Fig. 9.7. Furthermore, the pressure field at the end of the cavitation zone is depicted in the second column in Fig. 9.7. The upstream velocity at $l/l_{cav} = \{0.15, 0.5, 0.85\}$ is plotted over time in Fig. 9.8.

In the x-t diagram of $\sigma = 1.19$ the formation of a re-entrant jet at the beginning of each cycle and its upstream movement can be seen. The highest velocity peaks occur at the end of the

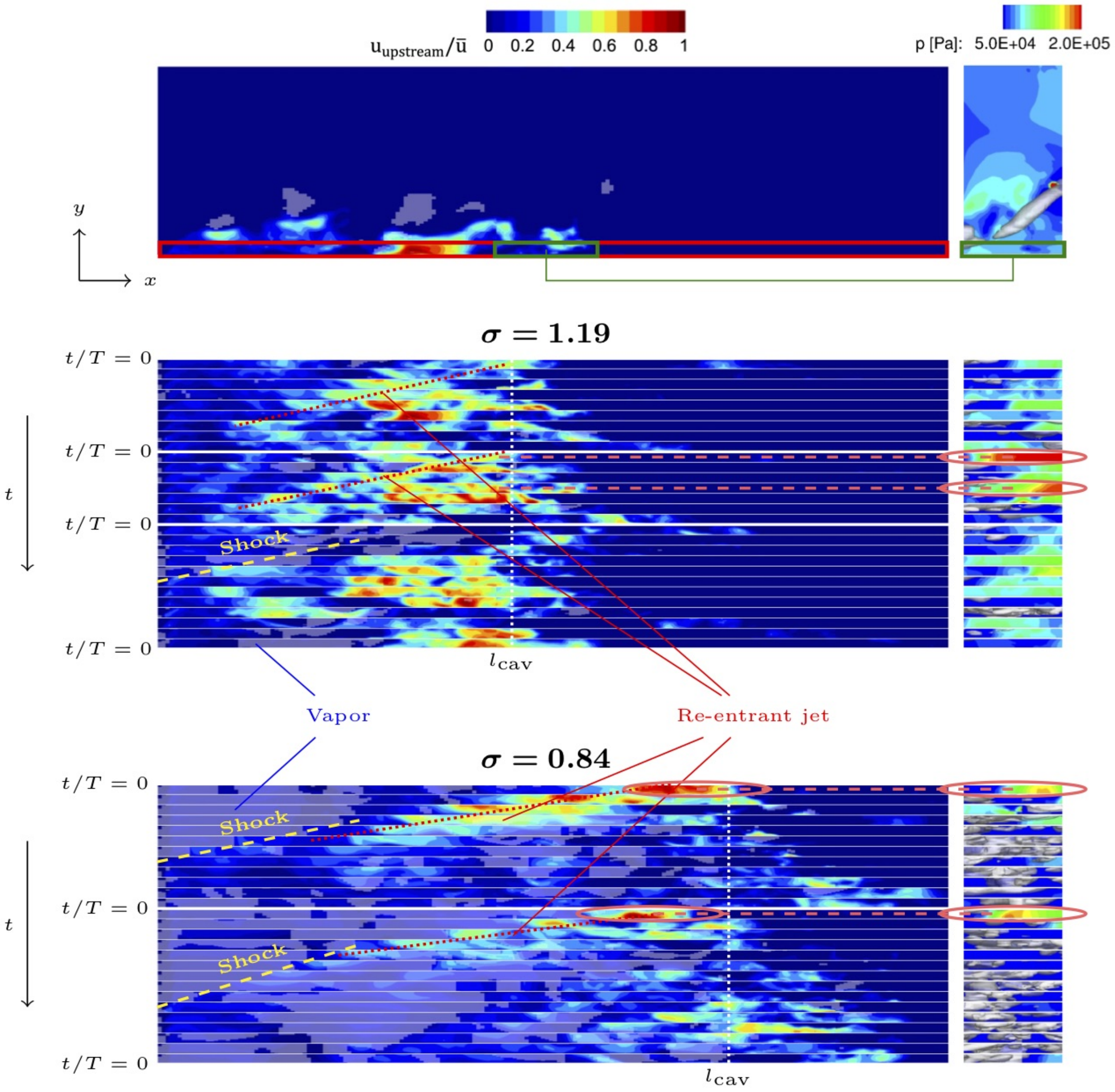

Figure 9.7.: Time series (x-t) of streamwise velocity u (left) and pressure field p (right) close to the wall ($h = 0.1\,\text{mm}$). Vapor regions ($\alpha = 0.1$) are indicated as bright regions (left) and as white isosurface(right). The top panel illustrates the investigated regions. Red dotted lines indicate the re-entrant jet motion and yellow dashed lines highlight the shock front. Pressure peaks downstream of the cavity are correlated to the velocity field and are marked in orange.

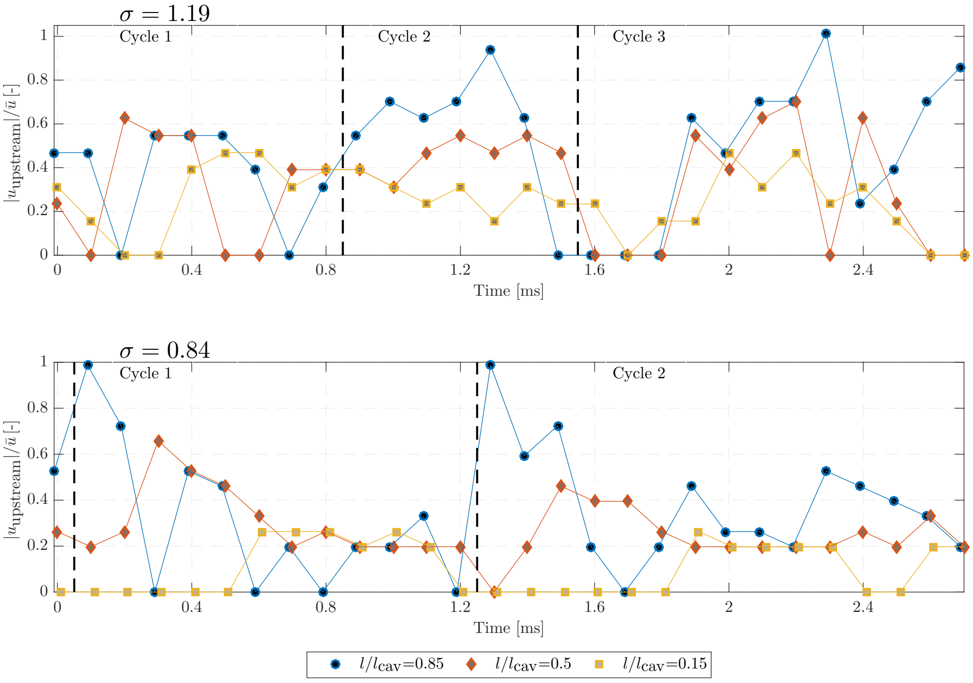

Figure 9.8.: Near-wall upstream velocity normalized by mean nozzle velocity $|u_{\text{upstream}}|/\bar{u}$ evaluated at different positions as a function of time.

sheet at about 2/3 of each cycle, see also Fig. 9.8, and are apparently induced by the rolling motion of the detached structures, see Fig. 9.3. Additionally, this upstream flow can be amplified by the pressure peak induced by the collapse of smaller vapor structures at the end of the sheet, see in the middle of the second cycle. Furthermore, the extracted velocities (Fig. 9.8) illustrate that the velocity magnitude tends to decrease in upstream direction.

For $\sigma = 0.84$, the x-t diagram (Fig. 9.7) and the extracted velocity (Fig. 9.8) show a clear and unique peak at the end of the cavitation zone at the beginning of the two cycles, which corresponds to the re-entrant jet formed there. A comparison with the pressure field (left column of Fig. 9.7) reveals that negative velocity peaks correlate with pressure peaks induced by the collapse of the shed cloud. The fluid with peak velocity moves upstream and slows down. In the x-t diagram it can be seen that further upstream the jet and the upstream flow are not purely liquid anymore and the jet also extends into the vapor region. While moving upstream the jet transforms into a condensation shock, which is clearly visible by the upstream moving vapor front in the x-t diagram. Close to the nozzle inlet (see 0.15 l_{cav} in Fig. 9.8), there is only an upstream flow after the condensation shock has passed. In the second half of the cycles, the velocity magnitudes at all three positions are about the same (20 - 30% of $\bar{u}$), which agrees with the measured data of Stanley et al. (2014). We point out that Stanley et al. (2014) reported an upstream moving deformation, which we believe is related to a condensation shock.

The re-entrant jet corresponds, in our notation of the shedding cycles, to the upstream flow at the beginning of the cycle. The determined re-entrant jet velocity magnitudes have peaks in the range of the mean velocity $\bar{u}$ at the end of the cavity and decrease in magnitude in upstream direction, which is in good agreement with experimental observations (Pham et al., 1999; Sakoda et al., 2001). At $\sigma = 1.19$, the re-entrant jet velocities are slightly lower and match well with the re-entrant jet velocity of half the mean velocity determined by Callenaere et al. (2001).

So far, the driving mechanism behind the re-entrant jet has not yet been completely clarified. In our simulations we observe for $\sigma = 0.84$ a clear correlation between the collapse of the shed cloud and a more pronounced upstream flow, which was proposed in the literature by e.g. Leroux et al. (2004, 2005). However, at $\sigma = 1.19$ we observe this correlation only once, which matches the finding by Coutier-Delgosha et al. (2007) that this relation is flow condition dependent. Moreover, we found that at $\sigma = 1.19$ the highest magnitude of the upstream flow is induced by the rolling motion of detached vapor structures and not associated with the re-entrant jet motion.

9.7. SUMMARY

Cloud cavitation is a common yet challenging phenomenon that occurs in external and in internal cavitating flows. Although orifices and nozzles with constant cross-section play an important role in technical applications, detailed investigations of cavitation dynamics and shedding mechanisms have been far less performed than for external flows or for flows in convergent-divergent geometries.

In this chapter, cavitation dynamics and shedding mechanisms of cavitating nozzle flows were investigated using wall-resolved LES results. The three-dimensional flow field data of several shedding cycles provide a deep insight into the physical processes of the cloud cavitation mechanisms in nozzle flows and allow detailed analyses of the flow field. Our results compare well with the reference experiment and reported observations for cavitation dynamics.

In our simulations, the shedding for inertia-driven supercavitation ($\sigma = 0.84$) is initiated by condensation shocks, whereas for developing cavitation ($\sigma = 1.19$) it is primarily initiated by re-entrant jets. The occurrence of condensation shocks at lower cavitation numbers is consistent with experimental findings. Our investigation reveals for the first time condensation shocks in cavitating nozzle flows with constant cross-section. Based on our observations, we have analyzed the shedding in detail and then adapted and extended the schematics of the cloud shedding process from the literature for the different mechanisms.

At both operating points, a re-entrant jet forms at the beginning of the cycle and in case of shock-initiated shedding the jet transforms further upstream into a shock. Our results confirm the existing theory that the re-entrant jet formation is related to the pressure peak induced by the collapse of the detached cloud. The determined re-entrant jet velocities are in the order of the mean nozzle velocity and decrease in upstream direction. For developing cavitation a pronounced upstream flow is present during the entire cycle, which first can be characterized as re-entrant jet motion and later as an upstream flow induced by the rolling motion of the detached vapor structures, which lead to the highest upstream velocities.

The analysis performed contributes to an improved understanding of cavitation dynamics in nozzles and has demonstrated the occurrence of condensation shocks there.

10. EFFECTS OF CAVITATION AND PARTIAL GAS ENTRAINMENT

In this chapter, we present results of Large-eddy simulations of cavitating nozzle flows with injection into gas, investigating the interactions between cavitation in the nozzle, primary jet breakup, mass flow rates, and gas entrainment. Two operating points (see Chapters 8 and 9) covering different cavitation regimes and jet characteristics are investigated. Special emphasis is placed on studying the effects of cavitation and partial gas entrainment in the nozzle on the mass flow and the jet. Therefore, frequency analyses of the recorded time-resolved signals are performed. Furthermore, the dynamics and intensities of imploding vapor structures are assessed.

This chapter is based on the publication Trummler et al. (2018c). Figures, tables and text sections are reprinted with permission of Begell House.

10.1. MOTIVATION

Cavitation in injection systems can have desired and undesired effects, as briefly discussed in Chapter 1. The most beneficial one is the promotion of primary jet break up and fuel atomization (Bergwerk, 1959; Reitz and Bracco, 1982). Since spray quality is one of the key parameters for combustion efficiency and reduction of pollutants, this can become a central aspect to fulfill future emission standards. Adverse effects are the reduction of mass flow and cavitation erosion. Cavitation can strongly interact with the mass flow, since the generated vapor reduces the effective cross-section and the discharge coefficient, as already observed by Bergwerk (1959); Nurick (1976). This can have a large impact because the amount of injected fuel is crucial for internal combustion processes and efficiency. Collapses near solid walls induce high surface loads, which can lead to material erosion (Philipp and Lauterborn, 1998) and finally to severe material damage and even to injector failure (Asi, 2006). In conclusion, it is vital to improve the understanding of cavitation and its consequences in order to optimize spray quality and the durability of injector components, and also to ensure a sufficient injection of fuel.

Another important aspect for cavitating nozzle flows with injection into gas, is gas entrainment into the nozzle. In experiments a distinction between gas and vapor is hardly possible because of similar physical properties. Only recently Duke et al. (2016) presented an application of x-ray fluorescence in which vapor and gas in a cavitating nozzle were measured simultaneously. However, partial gas entrainment in the nozzle and its effects have not yet been investigated in detail by experiments. Consequently, numerical simulations are essential to gain further insight into the effects of partial gas entrainment into the nozzle.

In this chapter, we first investigate the interaction between cavitation and mass flow and perform frequency analysis in Section 10.2. Then, we assess the dynamics and occurrence of collapse events in Section 10.3 and discuss the effects of cavitation and gas entrainment on the jet characteristics in Section 10.4.

10.2. EFFECTS ON THE MASS FLOW

In this section, the effects of cavitation and partial gas entrainment on the mass flow at the nozzle inlet and outlet are studied. First, we evaluate the discharge coefficients and compare them with the experimental ones. Then we analyze the direct interaction of the cavitation on the temporal mass flows and evaluate the dominant frequencies with FFT analysis. Finally, we also investigate the amplitude of the fluctuations of the mass flows.

The discharge coefficient is defined as

$$C_D = \frac{\dot{m}}{\dot{m}_{\text{theoretical}}} = \frac{\dot{m}}{A_{\text{theoretical}}\sqrt{2\rho(p_{\text{inlet}} - p_{\text{outlet}})}}, \tag{10.1}$$

where $A_{\text{theoretical}}$ denotes the cross-section area of the nozzle. It is well known, that cavitation leads to a decrease of the discharge coefficient, see e.g. the experimental investigations by (Nurick, 1976; Payri et al., 2004). From the available experimental data by Sou et al. (2014), we can derive the experimental discharge coefficient $C_{D,exp}$. Table 10.1 compares $C_{D,sim}$ with the experimental data, which are in excellent agreement.

We now analyze the temporal signals and investigate the direct effects of the cavitation on the mass flows. Figure 10.1 shows the temporal evolution of the mass flow and the integral vapor content together with their frequency spectra. For both operating points, a very strong correlation between the temporal evolution of the three signals is apparent. Additionally, the FFT reveals that the dominant frequency of the mass flows and the vapor volume is identical.

For $\sigma = 1.19$ we observe a periodic oscillation of the vapor content (black line) due to the shedding, see Fig. 10.1 (a). The mass flow at the inlet (gray dotted line) oscillates asynchronously to the vapor content. A mass flow maximum at the nozzle inlet corresponds to a rising flank of the vapor content. The vapor formation in the nozzle and the mass flow at the nozzle inlet are strongly coupled. When the mass flow and thus the velocity increases, the static pressure drops locally, and consequently more vapor is generated. The formed vapor reduces the effective cross-section, which results in a drop in the mass flow at the nozzle inlet. A reduced mass flow leads to less cavitation and less blocking of the cross-section which then consequently allows an increase of the mass flow again. The mass flow at the nozzle outlet (gray line) increases time-delayed to the vapor content. The delay is approximately 0.6 ms, which is slightly less than the average flow-through time of 0.625 ms (8 mm nozzle length and average velocity of 12.8 m/s). The formation of vapor leads to a replacement of the liquid and consequently also to a short acceleration of the fluid towards the outlet. This can cause the time-delayed peak of the mass flow at the outlet.

For the super-cavitating case $\sigma = 0.84$ (Fig. 10.1 (b)), the quantities oscillate with a lower frequency than $\sigma = 1.19$. In the depicted timespan we observe one 'double peak' in the integral vapor content at the beginning and one normal peak at approximately $t_0 + 1.6$ ms. Both peaks correspond to a clearly visible, slightly time advanced, drop in the mass flow at the nozzle inlet.

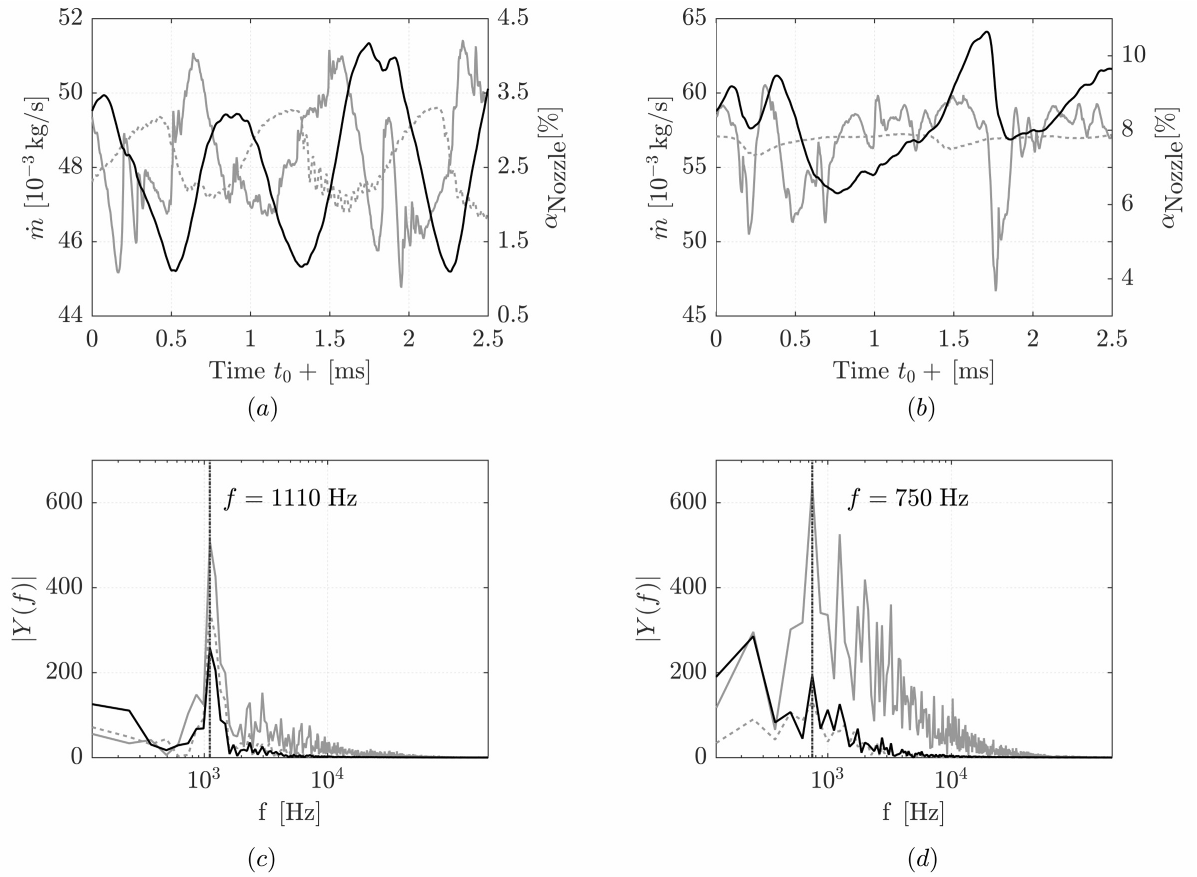

(*a*) (*b*)

(*c*) (*d*)

Figure 10.1.: Temporal evolution of the mass flow $\dot{m}$ at nozzle inlet (- - - -) and outlet (—) and vapor content $\alpha_{\mathrm{Nozzle}} = \mathrm{V}_{\mathrm{Vapor}}/\mathrm{V}_{\mathrm{Nozzle}} \cdot 100\%$ (—) as well as the amplitude of their complex frequency spectra $|Y(f)|$ over the frequency f. The operating point $\sigma = 1.19$ is shown in (a) and (c) and $\sigma = 0.84$ is shown in (b) and (d).

Thus, as for $\sigma = 1.19$, the increase of the vapor content initiates a drop of the mass flow at the inlet. For $\sigma = 0.84$, the mass flow at the outlet appears to be stronger governed by the cavitation. Every maximum in the vapor content corresponds to a slightly time-delayed minimum in the mass flow at the outlet. At $t_0 + 1.6$ ms there is a high peak in the vapor content and afterwards a significant drop of the mass flow at the outlet. From the analysis of the flow field data, we find that the high vapor content leads to partial gas entrainment which evokes a backflow and causes the drop of the mass flow.

The amplitude of the spectra is depicted in Fig. 10.1 (c) and (d). For $\sigma = 1.19$, the frequency with the highest amplitude is $f = 1110$ Hz, which is equivalent to a period of $T = 0.9$ ms. The dominant frequency decreases with the cavitation number and for $\sigma = 0.84$ the peak is at $f = 750$ Hz, $T = 1.32$ ms. Thus in both cases, the dominant frequencies of the mass flow and the vapor content coincide. This was also observed experimentally by Duke et al. (2015), who found corresponding peaks of the fractional power spectral density for the fluctuations at the inlet, for void-filled bubbles, the wall film, and the cavitation interface. Recently, Beban et al.

(2017) demonstrated a correlation between the mass flow at the nozzle outlet and integrated vapor content, for a submerged flow.

The coincidence of the peak frequencies of different quantities can be very useful to estimate unknown quantities. For instance, given an experimental time-resolved mass flow signal, one can evaluate the dominant frequency of the mass flow signal and, one may assume that this frequency is equivalent to the shedding frequency as well. Care has to be taken as spurious frequencies may be generated by the experimental apparatus. Furthermore, with an approximate Strouhal number, the cavity length can be estimated. Conversely, based on the cavity length, fluctuations of the mass flow can be estimated with the Strouhal number.

For most applications, such as combustion processes or injection processes, a stable mass flow of the fluid is desirable. Consequently, fluctuations in the discharged mass should be reduced. In Fig. 10.1 (a) and (b) we see significant fluctuations of the mass flow. Table 10.1 contains the relevant mass flow data as found in our simulations. Besides the mean mass flow $\overline{\dot{m}}$, the mean deviation of the mass flow from the average at the inlet and the outlet $\overline{|\dot{m}'|}$ as well as the maximum deviations from the mean values $\max(\dot{m}')$ are evaluated. As indicated in Table 10.1, the fluctuations at the inlet are very small on average. The average deviation and the maximum deviation at the inlet are higher for $\sigma = 1.19$. On one hand, this is partly due to the lower absolute value of the mean mass flow, but on the other hand, the mass flow at the inlet seems to be more strongly affected by cavitation at $\sigma = 1.19$ since the cavitation process occurs closer to the nozzle inlet. However, oscillations at the outlet are mostly more crucial for stable processes. Here we find average deviations approximately twice as large as at the inlet. And the maximum deviations have increased as well, rising with a decreasing cavitation number. As already discussed, the immense instantaneous drop of the mass flow at the outlet in the case of $\sigma = 0.84$ by nearly 20 % is triggered by gas entrainment.

Table 10.1.: Discharge coefficients, mass flows and their fluctuations.

σ	$C_{D,exp}$	$C_{D,sim}$	$\overline{\dot{m}}$ [g/s]	$\overline{\lvert\dot{m}'_{in}\rvert}$ [%]	$\max(\dot{m}'_{in})$ [%]	$\overline{\lvert\dot{m}'_{out}\rvert}$ [%]	$\max(\dot{m}'_{out})$[%]
1.19	0.83	0.83	48.4	1.63	3.32	2.75	7.12
0.84	0.81	0.80	57.0	0.42	1.93	3.39	18.12

10.3. FLOW DYNAMICS ASSOCIATED WITH COLLAPSING VAPOR PATTERNS

For partial cavitation, vapor structures detach and are advected downstream, where they implode due to the increased surrounding pressure. The collapse of a vapor structure leads to a collision of liquid fronts and subsequently to the emission of shock waves. In applications with higher inlet pressures, such as with Diesel injector components, such collapses can lead to severe material damage and to device failure. Available experimental data for this investigation do not provide information about collapse dynamics, collapse locations and possible impact loads. However, our compressible approach enables us to capture shock waves following collapse events. To detect the collapse events, we utilize the collapse detection algorithm developed by Mihatsch et al. (2015).

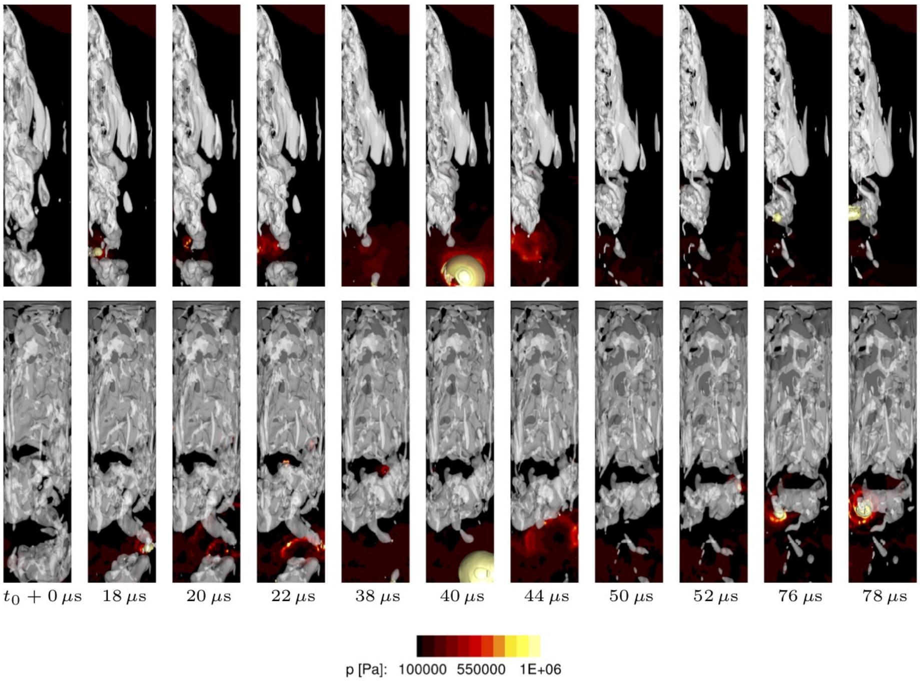

Figure 10.2.: Time series for $\sigma = 0.84$ with selected time steps capturing collapse events. Isosurfaces: vapor (10%, white) and pressure ($1 \cdot 10^6$ Pa, yellow) and wall pressure. Top row: Top view with the wall pressure at the back wall. Bottom row: Side view with wall pressure on the sidewall.

Collapse events are identified based on the vanishing of the vapor content in the cell and all next-neighbor cells and a negative divergence of the velocity. The maximum pressure is recorded and stored as collapse pressure p_c. Schmidt et al. (2014) and Mihatsch et al. (2015) have shown that using an inviscid flow model the recorded collapse pressure p_c depends on the grid resolution, since the collapse pressures are inversely proportional to the cell size at the collapse center. They proposed to scale the pressure with

$$p_{\text{c,scaled}} = p_c \cdot \frac{V_{\text{cell}}^{1/3}}{l_{\text{ref}}} \tag{10.2}$$

where V_{cell} is the cell volume and l_{ref} a reference length. The scaling law is motivated by the ideally radial decay of the maximum pressure with $1/r$ of an emitted shock wave. In order to predict collapse pressures correctly, the reference length l_{ref} needs to be calibrated with experimental data, see Mihatsch et al. (2015). Since there is insufficient information for calibrating the reference length for this investigation, we have adopted the smallest length scale in the evaluated dataset l_{ref}=7.14 µm. Consequently, the scaled collapse pressures $p_{\text{c,scaled}}$ do not provide absolute values for the case and can not be compared to material parameters. Nevertheless, the scaling is necessary for grids with inhomogeneous resolution.

In Fig. 10.2, a time series capturing collapse events at $\sigma = 0.84$ is depicted. At the end of the vapor sheet and in the detached cloud the vapor structures fragment and eventually collapse.

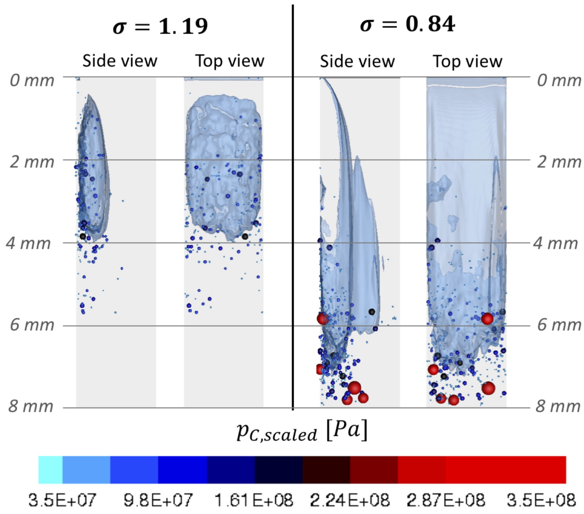

Figure 10.3.: Detected collapse events (shown as spheres with color and size corresponding to the collapse pressure) and isosurface of the averaged vapor content (10%, blue) over the analysis time of 4 ms.

After the collapse they emit a spherical shock wave, resulting in a circular pressure footprint. In the time series, the legend for the pressure is chosen for a lower range to capture and visualize collapse events. The pressure peaks after a collapse event have a very short duration and decay radially with $1/r$, such that it is very difficult to capture a collapse event and its aftermath with regular output.

Fig. 10.3 shows the detected collapses over the analysis time of 4 ms together with the averaged vapor content. For $\sigma = 1.19$ collapses are recorded between 25 % and 60 % of the nozzle length. Mainly they occur close to the wall in the second half of the average cavity, where during the cavitation process the highest fluctuation of the vapor takes place. At the operating point $\sigma = 0.84$ more collapses are detected and the recorded pressures are significantly higher than $\sigma = 1.19$. In this case, the collapses mostly occur at the end of the average cavitation zone or even shortly after and thus very close to the nozzle outlet. In order to evaluate the validity of the obtained results for high pressure applications with Diesel fuel, we compare our results to those obtained by Egerer et al. (2014). They perform LES of turbulent cavitating flows in a micro-channel with a typical Diesel-like test fluid and outlet pressures of $O(100\,\mathrm{bar})$. For *developing cavitation*, with high vapor dynamics in the first half of the channel, they monitored collapses in the first half of the channel and close to the wall. For strong cavitation, collapses were mainly detected close to the outlet and often significantly dislocated from the nozzle walls. This comparison indicates that areas where collapse events mainly occur can be estimated based on cavitation regimes independently of the working fluid and the injection pressure. However, in contrast to our results, they have predicted a higher risk of cavitation erosion for the operating point with *developing cavitation*. In our simulations, higher collapse pressures are detected for the smaller cavitation number in the *super-cavitating* regime.

An important aspect is that collapses amplify turbulent fluctuations, as has been observed

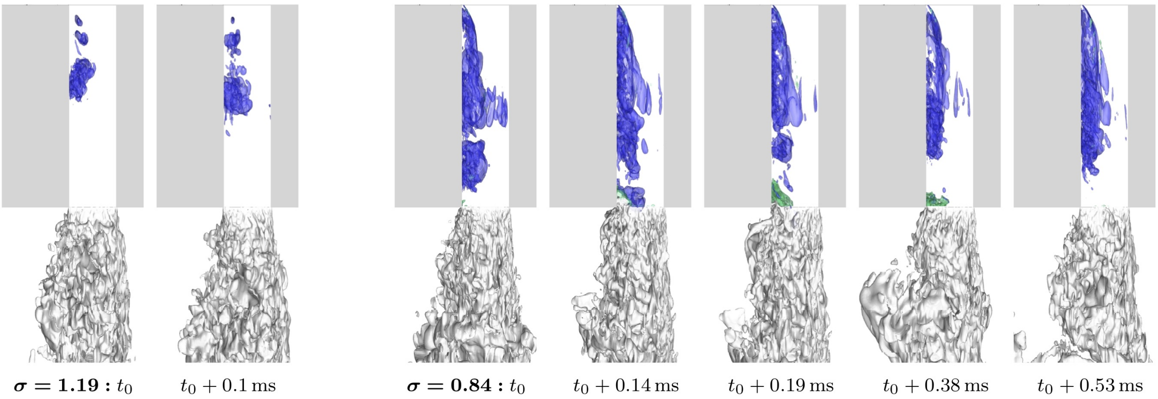
$\boldsymbol{\sigma = 1.19 : t_0}$
$t_0 + 0.1\,\mathrm{ms}$
$\boldsymbol{\sigma = 0.84 : t_0}$
$t_0 + 0.14\,\mathrm{ms}$
$t_0 + 0.19\,\mathrm{ms}$
$t_0 + 0.38\,\mathrm{ms}$
$t_0 + 0.53\,\mathrm{ms}$

Figure 10.4.: Time series for $\sigma = 1.19$ (left) and for $\sigma = 0.84$ (right). Vapor in the nozzle (blue, 10%), gas sucked into the nozzle (green, 10%) and jet surface (gray).

experimentally (Sou et al., 2007) and numerically (Örley et al., 2015). Consequently, intense collapses close to the nozzle outlet are considered as one of the main mechanisms to enhance primary jet break up. The effect of cavitation on the primary jet break up is discussed in Section 10.4.

10.4. EFFECTS OF CAVITATION AND PARTIAL GAS ENTRAINMENT ON THE JET

Intense cavitation in the nozzle affects the flow field close to the nozzle outlet and subsequently the discharged liquid jet. The time series in Fig. 10.4 visualize the cavitating flow in the nozzle together with the liquid jet injected into air. For $\sigma = 1.19$, no strong effect on the jet is present. However, the jet opening angle is increased on the cavitating side and the jet surface is more disturbed at this side as well. On the other side, for $\sigma = 0.84$ cavitation and partial gas entrainment have a strong impact on the jet appearance, especially close to the nozzle outlet. In the depicted time series partial gas entrainment leads to a bulging of the jet surface. At $t = 0.76$ ms the jet surface starts to bulge where the gas is sucked in and the spray angle near the outlet is suddenly strongly increased. Afterwards this bulge grows ($t = 0.81$ ms) and is convected downstream, where it bursts away and finally further detaches. This phenomenon was also described by Örley et al. (2015); Edelbauer (2017).

In experiments (Sou et al., 2007) and numerical investigations (Örley et al., 2015), collapse induced fluctuations have been found to enhance primary jet break-up. Besides the increased fluctuations, Örley et al. (2015) proposed two additional mechanisms: collapses inside the jet close to the surface and gas entrainment into the nozzle. In the following, we discuss and evaluate the influence of gas entrainment and collapse events on the jet characteristic. Figure 10.5 compares vorticity induced by collapse events and by gas entrainment. In Fig. 10.5 (a) a vapor structure collapses close to the nozzle outlet and induces a local increase of turbulent fluctuations, which are convected outside and disturb the jet surface. On the other hand, gas entrainment is visualized in Fig. 10.5 (b), where gas from the outlet area enters the nozzle and leads to higher vorticity than in (a) with larger spatial extent and subsequently to a strong increase of the near-nozzle

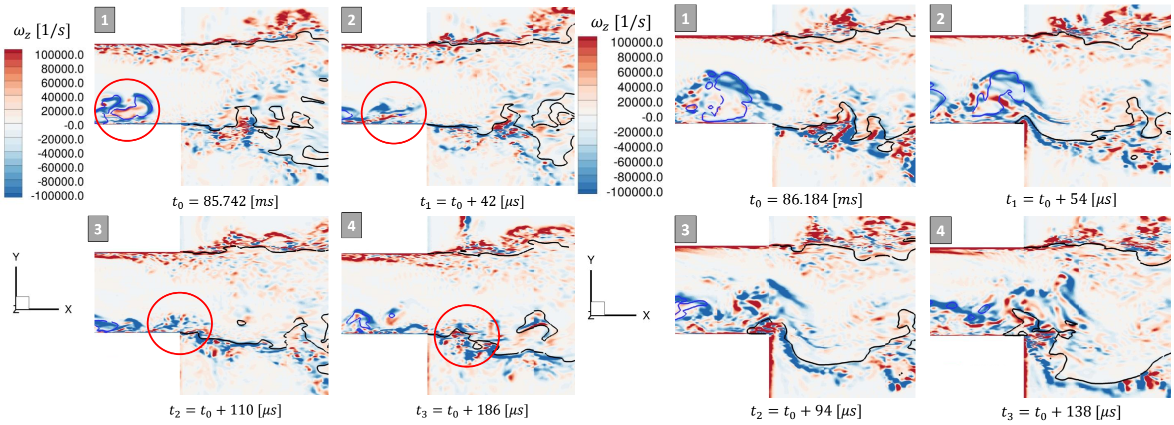

(a) **(b)**

Figure 10.5.: Vorticity after a collapse event (a) and after gas entrainment (b) for $\sigma = 0.84$; isolines: vapor (blue, 10%) gas (black, 75%).

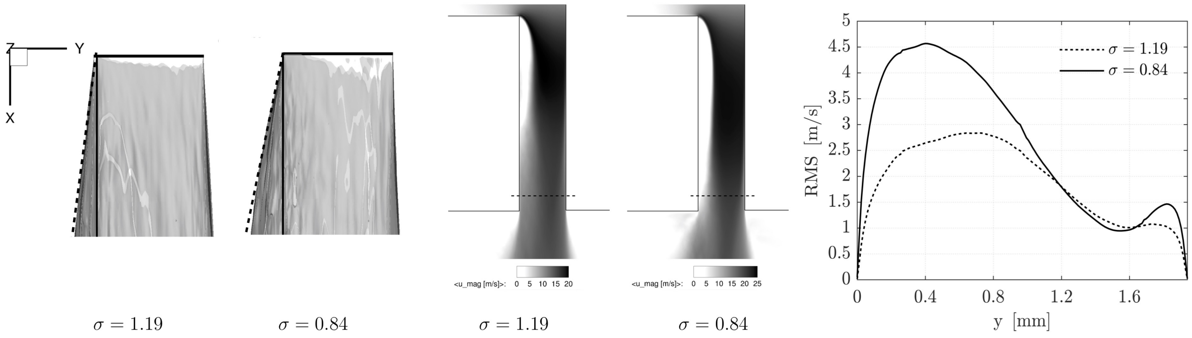

(a) (b) (c)

Figure 10.6.: (a) Averaged jet surface 75%. (b) Averaged velocity magnitude on the midplane and marked position of the evaluation of the fluctuations. (c) Fluctuations in lateral direction 0.5 mm before the nozzle outlet (nozzle length 8 mm). All data are averaged over 4 ms.

spray angle. Thus, we conclude that in the investigated configuration partial gas entrainment may have a more significant influence on the jet characteristic than collapse events.

The temporally averaged data, see Fig. 10.6, also confirm an increased mean jet angle in the super-cavitating case ($\sigma = 0.84$). For $\sigma = 1.19$ the average jet opening angle on the cavitation side is 6.5° and for $\sigma = 0.84$ it is 12.4°. Both values are in good agreement with experimental data (Sou et al., 2007; Stanley et al., 2011), although at $\sigma = 1.19$ our value is slightly higher than in the experiments, where it was found to lie between $4° - 5°$.

According to experimental investigations by Sou et al. (2007), velocities and fluctuations in lateral direction are among the key parameters for an enhanced jet break-up. Both can lead to a higher disturbance of the jet surface in lateral direction. Consequently, we now consider the average flow field in Fig. 10.6 (b) and the lateral velocity fluctuations 0.5 mm before the nozzle outlet in Fig. 10.6 (c). For $\sigma = 1.19$, the flow reattaches approximately at half the nozzle length, whereas for $\sigma = 0.84$ reattachment takes place close to the outlet. The lateral velocity fluctuations are higher on the side of the nozzle where flow detachment and cavitation occurs. However, at $\sigma = 0.84$ they are significantly increased compared to $\sigma = 1.19$. At higher y values ($1 - 1.6$ mm), where no influence by cavitation or flow detachment is present, the fluctuations are on a similar level. At the opposite wall, they increase again and are higher for $\sigma = 0.84$. These observations confirm the experimental findings by Sou et al. (2007).

10.5. SUMMARY

In this chapter, the effects of cavitation and gas entrainment on the mass flow, material damage due to cavitation erosion and jet characteristics were analyzed in great detail. With spectral analysis, we were able to confirm oscillations with the same frequency for the mass flow at the nozzle inlet and outlet as well as for the integral vapor volume in the nozzle. Discharge coefficients were calculated and match the experimental ones. Additionally, we found gas entrainment to influence strongly the mass flow at the nozzle outlet. Gas entrainment can lead to a temporary drop in the mass flow by nearly 20%. This can be crucial in injection processes if their efficiency is governed by the mass flow.

Our computation reproduces the interaction of the cavitating nozzle flow with the emanating jet. In the case of *supercavitation*, detached vapor structures can reach the nozzle outlet, leading to partial entrainment of gas from the outflow region into the nozzle. Due to the similar physical properties of vapor and gas, this mechanism is hard to capture experimentally. Our multi-component computation, however, allows a deeper insight into this phenomenon and its effects. Visualization of the numerical results revealed partial gas entrainment as one of the driving mechanisms for a widening of the jet. The other main factor is the presence of higher velocity fluctuations close to the nozzle outlet in the case of strong cavitation, which are induced by collapse events. Time-averaged data confirm that increased lateral fluctuations close to the nozzle outlet correlate with an increased averaged jet angle.

The performed numerical analyses serve as a basis for further investigations with higher injection pressures and realistic geometries.

Part IV.

CONCLUDING REMARKS

11. SUMMARY & OUTLOOK

11.1. SUMMARY

The scope of this work was the numerical investigation of cavitation phenomena associated with collapsing bubbles and nozzle flows. For these investigations, the two compressible flow solvers CATUM and ECOGEN were used. The performed simulations with high spatial and temporal resolution complement existing experimental investigations and allowed precise evaluations providing deeper insights. For the simulations conducted with CATUM, a multi-component model considering a cavitating liquid and an additional non-condensable gas component was employed. This model enables the investigation of realistic configurations in which gas can play an important role, such as vapor bubbles containing additional gas or discharge of cavitating nozzle flows into a gaseous ambient.

Firstly, collapsing bubbles were simulated. The aspherical collapse of near-surface vapor structures leads to material damage, which is a major effect of cavitation. While this is mostly disadvantageous in technical applications, the high damage potential is exploited in medical applications to e.g. destroy kidney stones. In this thesis, the effects of non-condensable gas inside vapor bubbles, of the driving pressure difference and of the surface topology on the bubble dynamics and erosion potential were assessed. To numerically capture the effect of non-condensable gas in vapor bubbles, an existing multi-component model has been extended and modified. The proposed model can correctly reproduce the enhancement of the rebound and the damping of pressure peaks by the gas. Additionally, also the energy partitioning into rebound and shock wave energy is captured by the model.

Subsequently, the collapse of wall-attached bubbles under atmospheric conditions was studied. The comparably low driving pressure of $\Delta p = 1\,\text{bar}$ enabled detailed evaluations of the rebound behavior and the influence of non-condensable gas in aspherical configurations. Schematics of the collapse and rebound behavior were derived, containing new findings for bubbles with a negative stand-off distance. As expected, consideration of additional non-condensable gas inside the vapor bubble increases the rebound and dampens the maximum pressure.

Furthermore, the collapse behavior and erosion potential of a gas bubble collapsing above a smooth wall and walls with cylindrical crevices were analyzed in detail. The dynamics and the recorded maximum wall pressures alter with the size of the crevice and the stand-off distance of the bubble. The presence of a large crevice leads to significantly different collapse dynamics compared to a smooth wall and a small crevice. The analyses of the induced maximum wall pressure showed that peak values are attenuated in intensity by the presence of a crevice, however, significant pressure over larger areas, as the entire crevice bottom, can be induced and high pressures also occur at the crevice edges.

Secondly, cavitating nozzle flows with injection into gas were investigated. Cavitating nozzle flows and the effect of cavitation in these applications are of high technical relevance, as e.g. in injector components. For the integral simulation of cavitation in the nozzle and the emanating jet, a multi-component model has been implemented in the flow solver CATUM and validated with wall-resolved LES of a reference experiment. The model is fully capable of reproducing different cavitation regimes and the effect of cavitation on the jet characteristics, both in accordance with the experiment. The time-resolved 3-D simulation results enabled further insights and, in particular, the evaluation of the effects of cavitation-induced gas entrainment into the nozzle on the jet and mass flow. We found that vapor structures collapsing close to the nozzle outlet and partial gas entrainment can promote jet widening.

Furthermore, cavitation dynamics and shedding mechanisms of the unsteady cavitation process in the nozzle were analyzed in detail. Depending on the cavitation regime, the shedding is either controlled by a re-entrant jet or by a condensation shock. The presented work is the first to report on condensation shock governed shedding in nozzles with a constant cross-section and to examine these dynamics in that configuration in detail. The re-entrant jet motion, its velocity and possible driving mechanisms were also evaluated. The re-entrant jet velocity is about the free stream velocity and decreases upstream in magnitude, which is in agreement with the literature.

In summary, this work contributes to a better understanding of cavitation-related processes and effects. The presented simulations cover different aspects of cavitation, ranging from the rebound of spherical bubbles to cavitation enhanced jet break-up. The numerical framework for the investigation of multi-component flows available in CATUM, which was developed and validated within this Ph.D. project, provides an ideal starting point for future investigations.

11.2. OUTLOOK

Some of the performed studies were highly innovative and their results motivate subsequent work. In the case of bubble collapses, future investigations may focus on the energy partitioning into rebound and shock wave energy in aspherical configurations. In this context, a precise evaluation of the influence of the driving pressure difference and the non-condensable gas inside vapor structures on the partitioning can also be a central aspect. Such a study can be based on the work of Supponen et al. (2017) on shock waves in non-spherical configurations and that of Mihatsch (2017) on energy partitioning of collapsing near-wall bubble clusters. To capture the effect of non-condensable gas in detail, the gas should be modeled adiabatic. For this purpose, a full thermodynamic multi-component model considering phase change is recommended.

Further, the presented study to the influence of surface topology on collapsing bubbles represents a pioneering work and provides a basis for future studies. These can, for instance, assess a broader range of geometric parameters such as crevice radius, depth, and shape. Apart from that, simulations of a bubble cluster collapsing near a non-smooth surface could also be an interesting aspect.

Regarding cavitating multi-component flows, future work can apply the successfully validated models to realistic configurations, such as high-pressure injection processes. But also other cavitating multi-component flows, as e.g. film-free laser printing (Patrascioiu et al., 2014) or needle-free injection (Tagawa et al., 2013), represent potential applications of the multi-component model. In the field of cavitation dynamics, subsequent studies can determine the effect of outgassing of gases dissolved in liquids on the shedding frequency, cavity length and erosion aggressiveness.

For further development of the in-house code CATUM, the implementation of an algorithm for the detection of structures, such as bubble fragments, vapor structures, jet droplets, and ligaments, would be a valuable extension. Such an algorithm would not only allow to track the fragmentation occurring at non-spherical bubble collapses, but also provide new insights into the cavitation dynamics of nozzle flows and quantitative data on the jet break-up. The intensity of collapse-induced shock waves correlates, among other things, with the size of the collapsing structure. Consequently, tracking of these structures is essential for analyses of energy partitioning in complex configurations and could also become a powerful approach for erosion prediction. The tool recently designed by Bußmann (2019) at the Chair of Aerodynamics and Fluid Mechanics could potentially be adapted for this future code development step of CATUM. Ideally, such an algorithm is combined with that developed by Mihatsch et al. (2015) for collapse induced pressure peaks, rendering it to the perfect tool for assessing energy partitioning.

BIBLIOGRAPHY

Abgrall, R., 1996. How to prevent pressure oscillations in multicomponent flow calculations: a quasi conservative approach. Journal of Computational Physics 125 (1), 150–160.

Adams, N., Hickel, S., Franz, S., 2004. Implicit subgrid-scale modeling by adaptive deconvolution. Journal of Computational Physics 200 (2), 412–431.

Akhatov, I., Lindau, O., Topolnikov, A., Mettin, R., Vakhitova, N., Lauterborn, W., 2001. Collapse and rebound of a laser-induced cavitation bubble. Physics of Fluids 13 (10), 2805–2819.

Allaire, G., Clerc, S., Kokh, S., 2002. A five-equation model for the simulation of interfaces between compressible fluids. Journal of Computational Physics 181 (2), 577–616.

Arndt, R. E., 1981. Cavitation in fluid machinery and hydraulic structures. Annual Review of Fluid Mechanics 13 (1), 273–326.

Arndt, R. E. A., Song, C. C. S., Kjeldsen, M., Keller, A., 2001. Instability of partial cavitation: A numerical/experimental approach. In: Twenty-Third Symposium on Naval Hydrodynamics Office of Naval Research Bassin d'Essais des Carenes National Research Council. pp. 599–615.

Asi, O., 2006. Failure of a diesel engine injector nozzle by cavitation damage. Engineering Failure Analysis 13 (7), 1126–1133.

Beattie, D. R. H., Whalley, P. B., 1982. A simple two-phase frictional pressure drop calculation method. International Journal of Multiphase Flow 8 (1), 83–87.

Beban, B., 2019. Numerical simulation of submerged cavitating throttle flows. Ph.D. thesis, Technical University of Munich.

Beban, B., Schmidt, S. J., Adams, N. A., 2017. Numerical study of submerged cavitating throttle flows. Atomization and Sprays 27 (8), 723–739.

Beig, S. A., Aboulhasanzadeh, B., Johnsen, E., 2018. Temperatures produced by inertially collapsing bubbles near rigid surfaces. Journal of Fluid Mechanics 852, 105–125.

Bensow, R. E., Bark, G., 2010. Implicit LES predictions of the cavitating flow on a propeller. Journal of Fluids Engineering 132 (4), 041302.

Bergwerk, W., 1959. Flow pattern in diesel nozzle spray holes. Proceedings of the Institution of Mechanical Engineers 173 (1), 655–660.

Besant, W., 1859. A Treatise on Hydrostatics and Hydrodynamics. Deighton, Bell, London.

Biçer, B., Sou, A., 2015. Numerical models for simulation of cavitation in diesel injector nozzles. Atomization and Sprays 25 (12), 1063–1080.

Biçer, B., Sou, A., 2016. Application of the improved cavitation model to turbulent cavitating flow in fuel injector nozzle. Applied Mathematical Modelling 40 (7-8), 4712–4726.

Bohner, M., Fischer, R., Gscheidle, R., 2001. Fachkunde Kraftfahrzeugtechnik. HaanGruiten, Verlag Europa-Lehrmittel.

Brackbill, J. U., Kothe, D. B., Zemach, C., 1992. A continuum method for modeling surface tension. Journal of Computational Physics 100 (2), 335–354.

Brandao, F. L., Bhatt, M., Mahesh, K., 2020. Numerical study of cavitation regimes in flow over a circular cylinder. Journal of Fluid Mechanics 885.

Brennen, C. E., 1995. Cavitation and Bubble Dynamics. Oxford University Press.

Budich, B., 2018. Shock phenomena in cavitating flow and its application to ship propellers. Ph.D. thesis, Technical University of Munich.

Budich, B., Borrmann, F., Schmidt, S. J., Adams, N. A., 2015. Assessment of erosion aggressiveness for the cavitating model propeller VP1304 by fully compressible numerical simulation. In: Proceedings of 18th Numerical Towing Tank Symposium, NuTTS. pp. 28–30.

Budich, B., Schmidt, S., Adams, N., 2016. Implicit large eddy simulation of the cavitating model propeller VP1304 using a compressible homogeneous mixture model. In: 31st Symposium on Naval Hydrodynamics.

Budich, B., Schmidt, S. J., Adams, N. A., 2018. Numerical simulation and analysis of condensation shocks in cavitating flow. Journal of Fluid Mechanics 838, 759–813.

Bußmann, A., 2019. Geometrical Tracking and Analysis of Interfaces and Flow Structures in Multiphase Flows. Master's thesis. Technical University of Munich.

Callenaere, M., Franc, J.-P., Michel, J.-M., Riondet, M., 2001. The cavitation instability induced by the development of a re-entrant jet. Journal of Fluid Mechanics 444, 223–256.

Chaves, H., Knapp, M., Kubitzek, A., Obermeier, F., Schneider, T., 1995. Experimental study of cavitation in the nozzle hole of diesel injectors using transparent nozzles. SAE International, 645–657.

Coussios, C. C., Roy, R. A., 2008. Applications of acoustics and cavitation to noninvasive therapy and drug delivery. Annual Review of Fluid Mechanics 40, 395–420.

Coutier-Delgosha, O., Stutz, B., Vabre, A., Legoupil, S., 2007. Analysis of cavitating flow structure by experimental and numerical investigations. Journal of Fluid Mechanics 578, 171–222.

Cristofaro, M., Edelbauer, W., Koukouvinis, P., Gavaises, M., 2019. A numerical study on the effect of cavitation erosion in a Diesel injector. Applied Mathematical Modelling, 1–35.

De Lange, D. F., De Bruin, G. J., 1998. Sheet Cavitation and Cloud Cavitation, Re-Entrant Jet and Three-Dimensionality . In: Biesheuvel, A., van Heijst, G. F. (Eds.), Fascination of Fluid Dynamics. Springer, pp. 91–114.

Dijkink, R., Ohl, C.-D., 2008. Laser-induced cavitation based micropump. Lab on a Chip 8 (10), 1676–1681.

Dittakavi, N., Chunekar, A., Frankel, S. H., 2010. Large Eddy Simulation of Turbulent-Cavitation Interactions in a Venturi Nozzle. Journal of Fluids Engineering 132 (12), 121301–11.

Döhring, A., Schmidt, S., Adams, N., 2018. Numerical investigation of transcritical turbulent channel flow. In: 2018 Joint Propulsion Conference. p. 4768.

Döhring, A., Schmidt, S. J., Adams, N. A., 2019. Large-eddy simulation of turbulent channel flow at transcritical states. In: 11th International Symposium on Turbulence and Shear Flow Phenomena, TSFP 2019.

Ducros, F., Ferrand, V., Nicoud, F., Weber, C., Darracq, D., Gacherieu, C., Poinsot, T., 1999. Large-Eddy Simulation of the Shock/ Turbulence Interaction. Journal of Computational Physics 152, 517–549.

Duke, D. J., Kastengren, A. L., Swantek, A. B., Matusik, K. E., Powell, C. F., 2016. X-ray fluorescence measurements of dissolved gas and cavitation. Experiments in Fluids 57 (10), 162.

Duke, D. J., Schmidt, D. P., Neroorkar, K., Kastengren, A. L., Powell, C. F., 2013. High-resolution large eddy simulations of cavitating gasoline–ethanol blends. International Journal of Engine Research 14 (6), 578–589.

Duke, D. J., Swantek, A. B., Kastengren, A. L., Fezzaa, K., Powell, C. F., 2015. Recent Developments in X-ray Diagnostics for Cavitation. SAE International Journal of Fuels and Lubricants 8 (1), 135–146.

Dular, M., Požar, T., Zevnik, J., et al., 2019. High speed observation of damage created by a collapse of a single cavitation bubble. Wear 418, 13–23.

Edelbauer, W., 2017. Numerical simulation of cavitating injector flow and liquid spray break-up by combination of eulerian–eulerian and volume-of-fluid methods. Computers & Fluids 144, 19–33.

Egerer, C. P., Hickel, S., Schmidt, S. J., Adams, N. A., 2014. Large-eddy simulation of turbulent cavitating flow in a micro channel. Physics of Fluids 26 (8), 085102.

Egerer, C. P., Schmidt, S. J., Hickel, S., Adams, N. A., 2016. Efficient implicit LES method for the simulation of turbulent cavitating flows. Journal of Computational Physics 316, 453–469.

Ferziger, J. H., Perić, M., Street, R. L., 2002. Computational methods for fluid dynamics. Vol. 3. Springer.

Franc, J.-P., Michel, J.-M., 2005. Fundamentals of cavitation. Dordrecht: Springer science & Business media.

Freudigmann, H.-A., Dörr, A., Iben, U., Pelz, P. F., 2017. Modeling of Cavitation-Induced Air Release Phenomena in Micro-Orifice Flows. Journal of Fluids Engineering 139 (11), 7–43.

Fujikawa, S., Akamatsu, T., 1980. Effects of the non-equilibrium condensation of vapour on the pressure wave produced by the collapse of a bubble in a liquid. Journal of Fluid Mechanics 97 (03), 481–34.

Furness, R., Hutton, S., 1975. Experimental and theoretical studies of two-dimensional fixed-type cavities. Journal of Fluids Engineering 97 (4), 515–521.

Ganesh, H., 2015. Bubbly shock propagation as a cause of sheet to cloud transition of partial cavitation and stationary cavitation bubbles forming on a delta wing vortex. Ph.D. thesis, University of Michigan.

Ganesh, H., Mäkiharju, S. A., Ceccio, S. L., 2016. Bubbly shock propagation as a mechanism for sheet-to-cloud transition of partial cavities. Journal of Fluid Mechanics 802, 37–78.

Germano, M., Piomelli, U., Moin, P., Cabot, W. H., 1991. A dynamic subgrid-scale eddy viscosity model. Physics of Fluids A: Fluid Dynamics 3 (7), 1760–1765.

Ghahramani, E., Arabnejad, M. H., Bensow, R. E., 2019. A comparative study between numerical methods in simulation of cavitating bubbles. International Journal of Multiphase Flow 111, 339–359.

Giannadakis, E., Gavaises, M., Arcoumanis, C., 2008. Modelling of cavitation in diesel injector nozzles. Journal of Fluid Mechanics 616, 153–41.

Gnanaskandan, A., Mahesh, K., 2016. Large eddy simulation of the transition from sheet to cloud cavitation over a wedge. International Journal of Multiphase Flow 83, 86–102.

Gopalan, S., Katz, J., 2000. Flow structure and modeling issues in the closure region of attached cavitation. Physics of Fluids 12 (4), 895–911.

Gorkh, P., Schmidt, S. J., Adams, N. A., 2018. Numerical investigation of cavitation-regimes in a converging-diverging nozzle. In: Katz, J. (Ed.), Proceedings of the 10th International Symposium on Cavitation. ASME Press, pp. 1–7.

Hayashi, S., Sato, K., 2014. Unsteady Behavior of Cavitating Waterjet in an Axisymmetric Convergent-Divergent Nozzle: High Speed Observation and Image Analysis Based on Frame Difference Method. Journal of Flow Control, Measurement & Visualization 02 (03), 94–104.

He, Z., Chen, Y., Leng, X., Wang, Q., Guo, G., 2016. Experimental visualization and LES investigations on cloud cavitation shedding in a rectangular nozzle orifice. International Communications in Heat and Mass Transfer 76 (C), 108–116.

Hickel, S., Adams, N. A., Domaradzki, J. A., 2006. An adaptive local deconvolution method for implicit LES. Journal of Computational Physics 213 (1), 413–436.

Hickel, S., Egerer, C. P., Larsson, J., 2014. Subgrid-scale modeling for implicit large eddy simulation of compressible flows and shock-turbulence interaction. Physics of Fluids 26 (10), 106101.

Hickel, S., Mihatsch, M., Schmidt, S. J., 2011. An adaptive local deconvolution method for implicit LES. WIMRC 3rd International Cavitation Forum.

Huang, B., Zhao, Y., Wang, G., 2014. Large eddy simulation of turbulent vortex-cavitation interactions in transient sheet/cloud cavitating flows. Computers & Fluids 92, 113–124.

Iben, U., Wolf, F., Freudigmann, H.-A., Fröhlich, J., Heller, W., 2015. Optical measurements of gas bubbles in oil behind a cavitating micro-orifice flow. Experiments in Fluids 56 (6), 1–10.

Jahangir, S., Hogendoorn, W., Poelma, C., 2018. Dynamics of partial cavitation in an axisymmetric converging-diverging nozzle. International Journal of Multiphase Flow 106, 34–45.

Jakobsen, J., 1964. On the mechanism of head breakdown in cavitating inducers. Journal of Basic Engineering 86 (2), 291–305.

Ji, B., Luo, X., Arndt, R. E., Peng, X., Wu, Y., 2015. Large eddy simulation and theoretical investigations of the transient cavitating vortical flow structure around a naca66 hydrofoil. International Journal of Multiphase Flow 68, 121–134.

Ji, B., Luo, X., Peng, X., Zhang, Y., Wu, Y., Xu, H., 2010. Numerical investigation of the ventilated cavitating flow around an under-water vehicle based on a three-component cavitation model. Journal of Hydrodynamics 22 (6), 753–759.

Johnsen, E., 2007. Numerical simulations of non-spherical bubble collapse. Ph.D. thesis, California Institute of Technology.

Johnsen, E., Colonius, T., 2009. Numerical simulations of non-spherical bubble collapse. Journal of Fluid Mechanics 629, 231–32.

Kapila, A., Menikoff, R., Bdzil, J., Son, S., Stewart, D., 2001. Two-phase modeling of deflagration-to-detonation transition in granular materials: Reduced equations. Physics of Fluids 13 (10), 3002–3024.

Kawanami, Y., Kato, H., Yamaguchi, H., Tanimura, M., Tagaya, Y., 1997. Mechanism and control of cloud cavitation. Journal of Fluids Engineering 119 (4), 788–794.

Keller, J. B., Miksis, M., 1980. Bubble oscillations of large amplitude. The Journal of the Acoustical Society of America, 1–6.

Koch, M., Lechner, C., Reuter, F., hler, K. K., Mettin, R., Lauterborn, W., 2017. Numerical modeling of laser generated cavitation bubbles with the finite volume and volume of fluid method, using OpenFOAM. Computers & Fluids, 1–34.

Koop, A., 2008. Numerical simulation of unsteady three-dimensional sheet cavitation. Ph.D. thesis, University of Twente.

Koop, A., Hoeijmakers, H., 2009. Numerical simulation of three-dimensional unsteady sheet cavitation. In: Proceedings of the 7th International Symposium on Cavitation. ASME Press.

Koren, B., 1993. A robust upwind discretization method for advection, diffusion and source terms. Centrum voor Wiskunde en Informatica Amsterdam.

Koukouvinis, P., Gavaises, M., Georgoulas, A., Marengo, M., 2016a. Compressible simulations of bubble dynamics with central-upwind schemes. International Journal of Computational Fluid Dynamics 30 (2), 129–140.

Koukouvinis, P., Gavaises, M., Li, J., Wang, L., 2016b. Large eddy simulation of diesel injector including cavitation effects and correlation to erosion damage. Fuel 175, 26–39.

Koukouvinis, P., Naseri, H., Gavaises, M., 2017. Performance of turbulence and cavitation models in prediction of incipient and developed cavitation. International Journal of Engine Research 18 (4), 333–350.

Kubota, A., Kato, H., Yamaguchi, H., Maeda, M., 1989. Unsteady structure measurement of cloud cavitation on a foil section using conditional sampling technique. Journal of Fluids Engineering 111 (2), 204–210.

Kunz, R. F., 2000. A preconditioned Navier-Stokes method for two-phase flows with application to cavitation prediction. Computers & Fluids, 1–27.

Kyriazis, N., Koukouvinis, P., Gavaises, M., 2018. Numerical investigation of bubble dynamics using tabulated data. International Journal of Multiphase Flow, 1–31.

Laberteaux, K., Ceccio, S., 2001. Partial cavity flows. part 1. cavities forming on models without spanwise variation. Journal of Fluid Mechanics 431, 1–41.

Lauer, E., Hu, X. Y., Hickel, S., Adams, N. A., 2012a. Numerical investigation of collapsing cavity arrays. Physics of Fluids 24 (5), 052104–25.

Lauer, E., Hu, X. Y., Hickel, S., Adams, N. A., 2012b. Numerical modelling and investigation of symmetric and asymmetric cavitation bubble dynamics. Computers & Fluids 69 (C), 1–19.

Lauterborn, W., Lechner, C., Koch, M., Mettin, R., 2018. Bubble models and real bubbles: Rayleigh and energy-deposit cases in a Tait-compressible liquid. IMA Journal of Applied Mathematics 83 (4), 556–589.

Le, Q., Franc, J.-P., Michel, J.-M., 1993. Partial cavities: global behavior and mean pressure distribution. Journal of Fluids Engineering 115 (2), 243–248.

Le Métayer, O., Massoni, J., Saurel, R., 2005. Modelling evaporation fronts with reactive Riemann solvers. Journal of Computational Physics 205 (2), 567–610.

Lechner, C., Lauterborn, W., Koch, M., Mettin, R., 2019. Fast, thin jets from bubbles expanding and collapsing in extreme vicinity to a solid boundary: A numerical study. Physical Review Fluids, 1–7.

Leroux, J. B., Astolfi, J. A., Billard, J. Y., 2004. An experimental study of unsteady partial cavitation. Journal of Fluids Engineering 126, 94–101.

Leroux, J.-B., Coutier-Delgosha, O., Astolfi, J. A., 2005. A joint experimental and numerical study of mechanisms associated to instability of partial cavitation on two-dimensional hydrofoil. Physics of Fluids 17 (5), 052101–21.

Lindau, O., Lauterborn, W., 2003. Cinematographic observation of the collapse and rebound of a laser-produced cavitation bubble near a wall. Journal of Fluid Mechanics 479, 327–348.

Lush, P., Skipp, S., 1986. High speed cine observations of cavitating flow in a duct. International Journal of Heat and Fluid Flow 7 (4), 283–290.

Malmberg, C., Käck, B., 2015. Aluminium foil at multiple length scales, mechanical tests and numerical simulations in abaqus. TFHF-5198.

Mauger, C., Méès, L., Michard, M., Azouzi, A., Valette, S., 2012. Shadowgraph, schlieren and interferometry in a 2d cavitating channel flow. Experiments in fluids 53 (6), 1895–1913.

McKenney, E., Brennen, C. E., 1994. On the dynamics and acoustics of cloud cavitation on an oscillating hydrofoil. In: ASME. No. 190. American Society of Mechanical Engineers, pp. 195–202.

Meng, J. C., Colonius, T., 2018. Numerical simulation of the aerobreakup of a water droplet. Journal of Fluid Mechanics 835, 1108–1135.

Mihatsch, M., 2017. Numerical prediction of erosion and degassing effects in cavitating flows. Ph.D. thesis, Technical University of Munich.

Mihatsch, M. S., Schmidt, S. J., Adams, N. A., 2015. Cavitation erosion prediction based on analysis of flow dynamics and impact load spectra. Physics of Fluids 27 (10), 103302–22.

Mithun, M.-G., Koukouvinis, P., Gavaises, M., 2018. Numerical simulation of cavitation and atomization using a fully compressible three-phase model. Physical Review Fluids 3 (6), 064304.

Nurick, W., 1976. Orifice cavitation and its effect on spray mixing. Journal of Fluids Engineering 98 (4), 681–687.

Obreschkow, D., Kobel, P., Dorsaz, N., De Bosset, A., Nicollier, C., Farhat, M., 2006. Cavitation bubble dynamics inside liquid drops in microgravity. Physical Review Letters 97 (9), 094502.

Ochiai, N., Iga, Y., Nohmi, M., Ikohagi, T., 2011. Numerical analysis of nonspherical bubble collapse behavior and induced impulsive pressure during first and second collapses near the wall boundary. Journal of Fluid Science and Technology 6 (6), 860–874.

Ogloblina, D., Schmidt, S. J., Adams, N. A., 2018. Simulation and analysis of collapsing vapor-bubble clusters with special emphasis on potentially erosive impact loads at walls. In: EPJ Web of Conferences. Vol. 180. EDP Sciences, p. 02079.

Ohl, C.-D., Arora, M., Dijkink, R., Janve, V., Lohse, D., 2006. Surface cleaning from laser-induced cavitation bubbles. Applied Physics Letters 89 (7), 074102.

Örley, F., 2016. Numerical simulation of cavitating flows in diesel injection systems. Ph.D. thesis, Technical University of Munich.

Örley, F., Hickel, S., Schmidt, S. J., Adams, N. A., 2016. Large-Eddy Simulation of turbulent, cavitating fuel flow inside a 9-hole Diesel injector including needle movement. International Journal of Engine Research, 1–17.

Örley, F., Trummler, T., Hickel, S., Mihatsch, M. S., Schmidt, S. J., Adams, N. A., 2015. Large-eddy simulation of cavitating nozzle flow and primary jet break-up. Physics of Fluids 27 (8), 086101–28.

Parker, B., Youngs, D., 1992. Two and three dimensional Eulerian simulation of fluid flow with material interfaces. Atomic Weapons Establishment.

Patrascioiu, A., Fernández-Pradas, J., Morenza, J., Serra, P., 2014. Film-free laser printing: Jetting dynamics analyzed through time-resolved imaging. Applied Surface Science 302, 303–308.

Payri, F., Bermudez, V., Payri, R., Salvador, F., 2004. The influence of cavitation on the internal flow and the spray characteristics in diesel injection nozzles. Fuel 83 (4-5), 419–431.

Pecha, R., Gompf, B., 2000. Microimplosions: cavitation collapse and shock wave emission on a nanosecond time scale. Physical Review Letters 84 (6), 1328.

Perigaud, G., Saurel, R., 2005. A compressible flow model with capillary effects. Journal of Computational Physics 209 (1), 139–178.

Petkovšek, M., Dular, M., 2013. Simultaneous observation of cavitation structures and cavitation erosion. Wear 300 (1-2), 55–64.

Pham, T., Larrarte, F., Fruman, D. H., 1999. Investigation of unsteady sheet cavitation and cloud cavitation mechanisms. Journal of Fluids Engineering 121 (2), 289–296.

Philipp, A., Lauterborn, W., 1998. Cavitation erosion by single laser-produced bubbles. Journal of Fluid Mechanics 361, 75–116.

Pishchalnikov, Y. A., Behnke-Parks, W. M., Schmidmayer, K., Maeda, K., Colonius, T., Kenny, T. W., Laser, D. J., 2019. High-speed video microscopy and numerical modeling of bubble dynamics near a surface of urinary stone. The Journal of the Acoustical Society of America 146 (1), 516–531.

Pishchalnikov, Y. A., Sapozhnikov, O. A., Bailey, M. R., Williams Jr., J. C., Cleveland, R. O., Colonius, T., Crum, L. A., Evan, A. P., McAteer, J. A., 2003. Cavitation bubble cluster activity in the breakage of kidney stones by lithotripter shockwaves. Journal of Endourology 17 (7), 435–446.

Plesset, M. S., 1949. The dynamics of cavitation bubbles. Journal of Applied Mechanics 16, 277–282.

Plesset, M. S., Chapman, R. B., 1971. Collapse of an initially spherical vapour cavity in the neighbourhood of a solid boundary. Journal of Fluid Mechanics 47 (2), 283–290.

Pöhl, F., Mottyll, S., Skoda, R., Huth, S., 2015. Evaluation of cavitation-induced pressure loads applied to material surfaces by finite-element-assisted pit analysis and numerical investigation of the elasto-plastic deformation of metallic materials. Wear 330-331, 618–628.

Pollack, G. L., 1991. Why gases dissolve in liquids. Science 251 (4999), 1323–1330.

Prosperetti, A., 1987. The equation of bubble dynamics in a compressible liquid. Physics of Fluids 30 (11), 3626–4.

Quirk, J. J., Karni, S., 1996. On the dynamics of a shock-bubble interaction. Journal of Fluid Mechanics 318, 129–163.

Rahn, D., 2017. Large-eddy simulation of a cavitating nozzle flow and primary jet breakup. Master's thesis. Technical University of Munich.

Rasthofer, U., Wermelinger, F., Karnakov, P., Šukys, J., Koumoutsakos, P., 2019. Computational study of the collapse of a cloud with 12 500 gas bubbles in a liquid. Physical Review Fluids 4 (6), 063602.

Rayleigh, O. F., 1917. VIII. On the pressure developed in a liquid during the collapse of a spherical cavity. The London, Edinburgh, and Dublin Philosophical Magazine and Journal of Science 34 (200), 94–98.

Reisman, G., Brennen, C., 1996. Pressure pulses generated by cloud cavitation. In: Proc. ASME Symp. on Cavitation and Gas - Liquid Flows in Fluid Machinery and Device FED 236. American Society of Mechanical Engineers, pp. 319—-328.

Reisman, G., Wang, Y.-C., Brennen, C. E., 1998. Observations of shock waves in cloud cavitation. Journal of Fluid Mechanics 355, 255–283.

Reitz, R., Bracco, F., 1982. Mechanism of atomization of a liquid jet. The Physics of Fluids 25 (10), 1730–1742.

Reuter, F., Gonzalez-Avila, S. R., Mettin, R., Ohl, C.-D., 2017. Flow fields and vortex dynamics of bubbles collapsing near a solid boundary. Physical Review Fluids 2 (6), 51–34.

Rodriguez, M., Johnsen, E., 2019. A high-order accurate five-equations compressible multiphase approach for viscoelastic fluids and solids with relaxation and elasticity. Journal of Computational Physics 379, 70–90.

Roe, P. L., 1986. Characteristic-based schemes for the euler equations. Annual Review of Fluid Mechanics 18 (1), 337–365.

Rudolf, P., Hudec, M., Gríger, M., Štefan, D., 2014. Characterization of the cavitating flow in converging-diverging nozzle based on experimental investigations. In: EPJ Web of conferences. Vol. 67. p. 02101.

Saito, Y., Sato, K., 2003. Growth process to cloud-like cavitation on separated shear layer. In: ASME/JSME 2003 4th Joint Fluids Summer Engineering Conference. pp. 1379–1384.

Sakoda, M., Yakushiji, R., Maeda, M., Yamaguchi, H., 2001. Mechanism of cloud cavitation generation on a 2-d hydrofoil. In: Proceedings of the International Symposium on Cavitation.

Sato, K., Saito, Y., 2002. Unstable cavitation behavior in a circular-cylindrical orifice flow. JSME International Journal Series B Fluids and Thermal Engineering 45 (3), 638–645.

Sato, T., Tinguely, M., Oizumi, M., Farhat, M., 2013. Evidence for hydrogen generation in laser- or spark-induced cavitation bubbles. Applied Physics Letters 102 (7), 074105–5.

Saurel, R., Petitpas, F., Berry, R. A., 2009. Simple and efficient relaxation methods for interfaces separating compressible fluids, cavitating flows and shocks in multiphase mixtures. Journal of Computational Physics 228 (5), 1678–1712.

Schenke, S., van Terwisga, T. J. C., 2019. An energy conservative method to predict the erosive aggressiveness of collapsing cavitating structures and cavitating flows from numerical simulations. International Journal of Multiphase Flow 111, 200–218.

Schmidmayer, K., Bryngelson, S. H., Colonius, T., 2020. An assessment of multicomponent flow models and interface capturing schemes for spherical bubble dynamics. Journal of Computational Physics 402 (109080).

Schmidmayer, K., Petitpas, F., Daniel, E., 2019a. Adaptive mesh refinement algorithm based on dual trees for cells and faces for multiphase compressible flows. Journal of Computational Physics 388, 252–278.

Schmidmayer, K., Petitpas, F., Le Martelot, S., Daniel, É., 2019b. ECOGEN: An open-source tool for multiphase, compressible, multiphysics flows. Computer Physics Communications, 107093.

Schmidt, S. J., 2015. A low mach number consistent compressible approach for simulation of cavitating flows. Ph.D. thesis, Technical University of Munich.

Schmidt, S. J., Mihatsch, M. S., Thalhamer, M., Adams, N. A., 2014. Assessment of Erosion Sensitive Areas via Compressible Simulation of Unsteady Cavitating Flows. In: Advanced Experimental and Numerical Techniques for Cavitation Erosion Prediction. Springer Netherlands, Dordrecht, pp. 329–344.

Schmidt, S. J., Sezal, I. H., Schnerr, G. H., 2006. Compressible simulation of high-speed hydrodynamics with phase change. In: Proceedings of the European Conference on Computational Fluid Dynamics. Delft University of Technology.

Schmidt, S. J., Thalhamer, M., Schnerr, G. H., 2009. Inertia controlled instability and small scale structures of sheet and cloud cavitation . In: Proceedings of the 7th International Symposium on Cavitation. ASME Press, pp. 1–14.

Schnerr, G. H., Sauer, J., 2001. Physical and numerical modeling of unsteady cavitation dynamics. In: Proceedings of the 4th International Conference on Multiphase Flow. Vol. 1. ICMF New Orleans.

Schnerr, G. H., Sezal, I. H., Schmidt, S. J., 2008. Numerical investigation of three-dimensional cloud cavitation with special emphasis on collapse induced shock dynamics. Physics of Fluids 20 (4), 040703–10.

Sezal, I., 2009. Compressible dynamics of cavitating 3-d multi-phase flows. Ph.D. thesis, Technical University of Munich, Technical University of Munich.

Shams, E., Finn, J., Apte, S. V., 2011. A numerical scheme for euler–lagrange simulation of bubbly flows in complex systems. International Journal for Numerical Methods in Fluids 67 (12), 1865–1898.

Shima, A., Nakajima, K., 1977. The collapse of a non-hemispherical bubble attached to a solid wall. Journal of Fluid Mechanics 80 (02), 369–23.

Shima, A., Takayama, K., Tomita, Y., Ohsawa, N., 1983. Mechanism of impact pressure generation from spark-generated bubble collapse near a wall. AIAA Journal 21 (1), 55–59.

Shima, A., Tomita, Y., Takahashi, K., 1984. The collapse of a gas bubble near a solid wall by a shock wave and the induced impulsive pressure. Proceedings of the Institution of Mechanical Engineers, Part C: Journal of Mechanical Engineering Science 198 (2), 81–86.

Shyue, K.-M., 1998. An efficient shock-capturing algorithm for compressible multicomponent problems. Journal of Computational Physics 142 (1), 208–242.

Shyue, K. M., Xiao, F., 2014. An Eulerian interface sharpening algorithm for compressible two-phase flow: The algebraic THINC approach. Journal of Computational Physics 268, 326–354.

Singhal, A. K., Athavale, M. M., Li, H., Jiang, Y., 2002. Mathematical basis and validation of the full cavitation model. Journal of Fluids Engineering 124 (3), 617–624.

Sou, A., Biçer, B., Tomiyama, A., 2014. Numerical simulation of incipient cavitation flow in a nozzle of fuel injector. Computers & Fluids 103 (C), 42–48.

Sou, A., Hosokawa, S., Tomiyama, A., 2007. Effects of cavitation in a nozzle on liquid jet atomization. International Journal of Heat and Mass Transfer 50 (17-18), 3575–3582.

Stanley, C., Barber, T., Milton, B., Rosengarten, G., 2011. Periodic cavitation shedding in a cylindrical orifice. Experiments in Fluids 51 (5), 1189–1200.

Stanley, C., Barber, T., Rosengarten, G., 2014. Re-entrant jet mechanism for periodic cavitation shedding in a cylindrical orifice. International Journal of Heat and Fluid Flow 50 (C), 169–176.

Stutz, B., Reboud, J. L., 1997. Experiments on unsteady cavitation. Experiments in Fluids 22 (3), 191–198.

Sugimoto, Y., Sato, K., 2009. Visualization of unsteady behavior of cavitation in circular cylindrical orifice with abruptly expanding part. In: 13th International Topical Meeting on Nuclear Reactor Thermal Hydraulics. Vol. 13. pp. N13P1156, 1–10.

Supponen, O., Kobel, P., Obreschkow, D., Farhat, M., 2015. The inner world of a collapsing bubble. Physics of Fluids 27 (9), 091113–3.

Supponen, O., Obreschkow, D., Kobel, P., Tinguely, M., Dorsaz, N., Farhat, M., 2017. Shock waves from nonspherical cavitation bubbles. Physical Review Fluids 2 (9), 093601.

Supponen, O., Obreschkow, D., Tinguely, M., Kobel, P., Dorsaz, N., Farhat, M., 2016. Scaling laws for jets of single cavitation bubbles. Journal of Fluid Mechanics 802, 263–293.

Tagawa, Y., Oudalov, N., El Ghalbzouri, A., Sun, C., Lohse, D., 2013. Needle-free injection into skin and soft matter with highly focused microjets. Lab on a Chip 13 (7), 1357–1363.

Tinguely, M., Obreschkow, D., Kobel, P., Dorsaz, N., de Bosset, A., Farhat, M., 2012. Energy partition at the collapse of spherical cavitation bubbles. Physical Review E, 1–7.

Tiwari, A., Freund, J. B., Pantano, C., 2013. A diffuse interface model with immiscibility preservation. Journal of Computational Physics 252, 290–309.

Tiwari, A., Pantano, C., Freund, J. B., 2015. Growth-and-collapse dynamics of small bubble clusters near a wall. Journal of Fluid Mechanics 775, 1–23.

Tomita, Y., Robinson, P. B., Tong, R. P., Blake, J. R., 2002. Growth and collapse of cavitation bubbles near a curved rigid boundary. Journal of Fluid Mechanics 466, 259–283.

Tomita, Y., Shima, A., 1986. Mechanisms of impulsive pressure generation and damage pit formation by bubble collapse. Journal of Fluid Mechanics 169, 535–564.

Toro, E. F., 1997. Riemann solvers and numerical methods for fluid dynamics. Springer Verlag, Berlin.

Trummler, T., 2014. Gasmodellierung in kavitierenden Strömungen. Master's thesis. Technical University of Munich.

Trummler, T., Bryngelson, S. H., Schmidmayer, K., Schmidt, S. J., Colonius, T., Adams, N. A., 2020a. Near-surface dynamics of a gas bubble collapsing above a crevice. Journal of Fluid Mechanics.

Trummler, T., Freytag, L., Schmidt, S. J., Adams, N. A., 2018a. Large eddy simulation of a collapsing vapor bubble containing non-condensable gas. In: Katz, J. (Ed.), Proceedings of the 10th International Symposium on Cavitation. ASME Press, pp. 656–659.

Trummler, T., Rahn, D., Schmidt, S. J., Adams, N. A., 2018b. Large eddy simulation of cavitating nozzle flows and primary jet break-up with gas-entrainment into the nozzle. In: Katz, J. (Ed.), Proceedings of the 10th International Symposium on Cavitation. ASME Press, pp. 660–664.

Trummler, T., Rahn, D., Schmidt, S. J., Adams, N. A., 2018c. Large eddy simulations of cavitating flow in a step nozzle with injection into gas. Atomization and Sprays 28 (10), 931–955.

Trummler, T., Schmidt, S. J., Adams, N. A., 2019. Numerical simulation of aspherical collapses of vapor bubbles containing non-condensable gas. In: Proceedings of the 10th International Conference on Multiphase Flow.

Trummler, T., Schmidt, S. J., Adams, N. A., 2020b. Investigation of condensation shocks and re-entrant jet dynamics in a cavitating nozzle flow by Large-Eddy Simulation. International Journal of Multiphase Flow (125), 103215.

Van Leer, B., 1977. Towards the ultimate conservative difference scheme III. Upstream-centered finite-difference schemes for ideal compressible flow. Journal of Computational Physics 23 (3), 263–275.

Veilleux, J. C., Maeda, K., Colonius, T., 2018. Transient cavitation in pre-filled syringes during autoinjector actuation. In: Katz, J. (Ed.), Proceedings of the 10th International Symposium on Cavitation. ASME Press, pp. 1–7.

Vogel, A., Busch, S., 1996. Shock wave emission and cavitation bubble generation by picosecond and nanosecond optical breakdown in water. The Journal of the Acoustical Society of America, 1–18.

Vogel, A., Lauterborn, W., Timm, R., 1989. Optical and acoustic investigations of the dynamics of laser-produced cavitation bubbles near a solid boundary. Journal of Fluid Mechanics 206, 299–338.

Wade, R., Acosta, A., 1966. Experimental observations on the flow past a plano-convex hydrofoil. Journal of Basic Engineering 88 (1), 273–282.

Wang, C., Huang, B., Wang, G., Zhang, M., Ding, N., 2017. Unsteady pressure fluctuation characteristics in the process of breakup and shedding of sheet/cloud cavitation. International Journal of Heat and Mass Transfer 114, 769–785.

Wang, Y., Qiu, L., Reitz, R. D., Diwakar, R., 2014. Simulating cavitating liquid jets using a compressible and equilibrium two-phase flow solver. International Journal of Multiphase Flow 63, 52–67.

Wu, X., Maheux, E., Chahine, G. L., 2017. An experimental study of sheet to cloud cavitation. Experimental Thermal and Fluid Science 83, 129–140.

Xiao, F., Honma, Y., Kono, T., 2005. A simple algebraic interface capturing scheme using hyperbolic tangent function. International Journal for Numerical Methods in Fluids 48 (9), 1023–1040.

Zhang, Y., Li, S., Zhang, Y., Zhang, Y., 2018. Dynamics of the bubble near a triangular prism array. In: Katz, J. (Ed.), Proceedings of the 10th International Symposium on Cavitation. ASME Press, pp. 312–317.

Zupanc, M., Kosjek, T., Petkovšek, M., Dular, M., Kompare, B., Širok, B., Blažeka, Ž., Heath, E., 2012. Removal of pharmaceuticals from wastewater by biological processes, hydrodynamic cavitation and uv treatment. Ultrasonics - Sonochemistry, 1–49.